NASA Technical Memorandum 100881

Particle-Laden Weakly Swirling Free Jets: Measurements and Predictions

Daniel L. Bulzan
Lewis Research Center
Cleveland, Ohio

May 1988

NASA

TABLE OF CONTENTS

NOMENCLATURE

Symbol	Description
A_i	terms used in equations (B.6) and (B.7)
a	acceleration of gravity
C	mass fraction
C_D	drag coefficient
C_i	parameters in turbulence model
DSF	deterministic separated flow
d	injector diameter
d_p	particle diameter
E	mean signal output of counter
e	fluctuating signal output of counter
F_c	body force term, equation (3.13)
f	mixture fraction
G	particle mass flux
K	overall calibration factor of signal processor
k	turbulence kinetic energy
L	dissipation length scale, equation (4.1)
L_e	dissipation length scale of eddy
LHF	locally homogeneous flow
LV	laser velocimeter
$\dot{m}$	mass flow rate
m_p	particle mass

n	number of particle groups
n_i	number of particles per unit time in group i
PDF	probability density function
$P(f)$	probability density function for f
p	pressure
R	injection tube radius
Re_p	particle Reynolds number
S_ϕ	source term
SMD	Sauter mean diameter
$S_{p\phi}$	source term due to particles
SSF	stochastic separated flow
t	time
t_e	eddy lifetime
u	axial velocity
V_j	volume of computational cell j
v	radial velocity
w	tangential velocity
x	axial distance
$\vec{X_p}$	particle position vector
Δx_p	relative path length of particles in an eddy
Δt_p	particle residence time in an eddy
ε	rate of dissipation of turbulence kinetic energy
μ	laminar viscosity
μ_t	turbulent viscosity

ρ	density
σ_i	turbulent Prandtl/Schmidt number
ϕ	generic property
ψ	stream function
ω	dimensionless stream function, equation (B.1)

Subscripts

a	air
c	centerline quantity
E	external boundary
I	internal boundary
m	maximum condition
o	injector exit condition
p	particle property
t	measured data
∞	ambient condition

Superscripts

$(\bar{})$	time-averaged quantity
$(\tilde{})$	Favre-averaged quantity
$(\,)'$	fluctuating quantity
$\vec{(\,)}$	vector quantity

ACKNOWLEDGMENTS

The author would like to express his indebtedness to his advisor, Professor G.M. Faeth, for his invaluable guidance and encouragement during the course of the investigation. The author would also like to acknowledge his appreciation to Dr. J.-S. Shuen for his assistance during the investigation.

CHAPTER I

INTRODUCTION

1.1 General Statement of the Problem

Turbulent flows containing a dispersed phase, e.g., particles, drops, or bubbles, are often encountered during the design of heat transfer, mass transfer, and combustion equipment. For example, in gas turbine combustors, liquid fuel is generally sprayed into a turbulent swirling recirculating flowfield where the liquid breaks up into droplets, evaporates, and reacts. Because of the high cost of designing combustors, there is substantial interest in developing computer models of this very complicated two-phase flow. A better understanding of the fundamental processes involved in these flows can be used to improve current computer models and subsequently enhance the ability to accurately predict flow properties.

While understanding the entire spray combustion problem is the eventual goal, a simpler problem is considered here. The present study is limited to the investigation of particle-laden weakly swirling free jets. For this case, the only interaction between the two phases is the exchange of momentum. The arrangement considered consisted of axisymmetric weakly swirling air jets containing particles, which are injected downward into stagnant air. The swirl number was limited to 0.4 or less so that a recirculation zone is not formed and the boundary-layer approximations can be made. Major features of the flow that are of interest during the present

investigation include: the velocity distribution of both phases, the distribution of void fraction, and particle concentrations. The continuous phase is turbulent; therefore, local velocity fluctuations and Reynolds stresses are important parameters since they control the rate of spread of the continuous phase and the entrainment of ambient air into the jet. The particles interact with the turbulent continuous phase and exhibit random processes as a result; therefore, both the mean and fluctuating properties of the particle phase are of interest. Turbulent dispersion of particles, i.e., the motion of particles due to their interaction with turbulent eddies, is important since it strongly influences the spread of the particles. Finally, particle concentrations are valuable since they reflect the mixing properties of the flow.

The present study attempts to resolve some of these features emphasizing new measurements in weakly swirling particle-laden flows. Predictions are also considered, both to help interpretation of the measurements and to initiate evaluation of methods to analyze flow properties. The following section will briefly describe previous studies of two-phase flows which are related to the present study.

1.2 Related Studies

1.2.1 Single-Phase Swirling Jets

Single-phase swirling jets have been studied by a large number of investigators. Earlier experimental studies of swirling jets have been reported in Refs. 1 - 13. Theoretical analysis of some aspects

of swirling flows is described by Murthy (14)*. The present discussion will primarily concentrate on previous studies of unconfined swirling jets.

In the experimental studies reported in Refs. 1 - 12, swirl has been generated by various methods. Rose (1) and Pratt and Keffer (2) generated a swirling jet by rotating a round tube which was passing a fully developed flow. Mathur and Maccalum (3), Kerr and Fraser (4), and Sislian and Cusworth (5) used swirlers to generate the tangential component of velocity for their swirling flows. Tangential air injection into an axial flow has also been frequently used (6 - 11). Gouldin, et al. (12) utilized both swirlers and tangential air injection. For the earlier experimental studies (3, 4, 6 and 9), pitot probes were used to measure velocities; therefore, only mean velocities were reported. Hot-wire anemometry has also been used to measure both mean and fluctuating velocities (1, 2, 7, 8, and 11). Later studies used nonintrusive laser-Doppler anemometry (LDA) to measure mean and fluctuating quantities (5 and 12).

A measure of the amount of swirl in a flow is given by the swirl number. The swirl number is the axial flux of angular momentum divided by the axial flux of axial momentum multiplied by a representative length (15). For a constant density free jet in stagnant surroundings, neglecting effects of fluctuating velocities, the swirl number can be calculated from the following expression:

*Numbers in parenthesis denote references.

$$S = \frac{\int_0^\infty \bar{\rho}\,\bar{u}\bar{w}\,r^2 dr}{R\int_0^\infty \left[\bar{\rho}\bar{u}^2 + (\bar{p} - \bar{p}_\infty)\right] r\,dr} \qquad (1.1)$$

The swirl number, S, is a conserved property of the flow if the ambient conditions are stagnant, i.e., if the ambient turbulence intensity and angular velocity are zero and there is no imposed longitudinal pressure gradient. As discussed in Ref. 15, the swirl number is an important parameter of a swirling flow. For swirl numbers less than about 0.6, the adverse pressure gradient caused by the tangential velocity decay is not strong enough to cause a reversal of the axial velocity. Such flows are called weakly swirling flows and have been analyzed using the boundary-layer approximations (10 and 11). As the swirl number increases, the rate of growth, the rate of entrainment of ambient fluid, and the rate of axial velocity decay all increase. At swirl numbers above about 0.6, strong axial and radial pressure gradients are present which cause a recirculation zone to be formed along the axis. As discussed in Ref. 15, these flows are governed by elliptic partial differential equations.

Lee (16) reports an early theoretical analysis of unconfined, asymmetric, turbulent swirling jets, based on similarity of axial and swirling velocity profiles, as well as lateral entrainment. The comparison between predictions and the measurements of Rose (1), for mean values of axial and angular velocity at an axial distance of three pipe diameters downstream of the jet exit, were reasonably

good. Several computer models of turbulent swirling jets have been reported (10, 11, and 17 - 22). A study, reported by Siddhartha (10), used a parabolic marching procedure with a turbulence model based on the Prandtl mixing-layer hypothesis to predict both free and confined weakly swirling jets. Lilley (18) used an identical parabolic code with a mixing-length turbulence model that was empirically modified to account for anisotropy. Later studies have employed more advanced turbulence models. Koosinlin and Lockwood (22) used an algebraic-stress turbulence model to predict swirling boundary-layer flows. Morse (11) predicted the structure of weakly swirling turbulent free jets with a full Reynolds-stress turbulence model. His predictions, using the full Reynolds-stress model, did not show any better agreement with experimental data than much simpler mixing-length formulations. This Reynolds-stress closure has recently been modified, however, by Gibson and Younis (23) to improve its performance in swirling jets. Elliptic type calculations of swirling flows, using the two-equation k-ε turbulence model, can be found in Refs. 17 and 19 - 21.

Swirling flows are very important in combustion applications. Studies of combusting swirling flows can be found in Refs. 13 and 24 - 26.

1.2.2 Particle-Laden Flows

Previous research on particle-laden flows is quite extensive. A comprehensive discussion early work in this area can be found in Soo

(27). More recent reviews of particle-laden flows can be found in Refs. 28 - 30. Since experimental studies of two-phase flows are very numerous, the present discussion will be mainly limited to recent studies of particle- or droplet-laden jets. Yuu et al. (31) studied particle-laden jets containing fly-ash particles (15 to 20 μm in diameter) injected into stagnant air from a nozzle designed to produce a uniform outlet velocity. Gas-phase mean velocity and particle concentration measurements were reported. McComb and Salih (32 and 33) measured particle concentrations of 2.3 and 5.7 μm diameter particles injected into stagnant air, using laser-Doppler anemometry (LDA) techniques. Popper et al. (34) used LDA techniques to measure velocities of oil droplets whose diameters were estimated to be less than 50 μm: the jets of oil droplets and air were injected into still air from a nozzle designed to produce a uniform velocity at the exit; the mass-loading ratio of droplets to air for their flow was limited to an extremely low value of 0.001. Levy and Lockwood (35) measured mean and fluctuating velocities of both the gas phase and particles, using LDA, for a round jet discharging into still air: the injection pipe was 40 diameters long in order to obtain approximately fully developed turbulent flow at the exit; the particles used were relatively large sand particles, in the range of 215 to 1060 μm in diameter; while mass-loading ratios were fairly high and ranged from 1.1 to 3.5. Modarress et al. (36 and 37) used a two-color LDA to measure mean and fluctuating velocities of both the particle and gas

phases: their experimental configuration consisted of a round jet discharging into a low velocity co-flowing airstream within a duct, with particles consisting of glass beads, 50 and 200 μm in diameter, and mass-loading ratios of 0.32 to 0.85. Shuen et al. (38 - 40), Shuen (41) and Zhang et al. (42) reported measurements of a particle-laden round jet discharging into a stagnant environment using three sizes of sand particles (79, 119, and 207 μm in diameter) and various loading ratios, while employing LDA to measure the velocities of both phases. Solomon et al. (43 and 44) reported measurements in a nonevaporating spray of vacuum-pump oil from an air-atomizing injector, using a double-flash photographic technique to measure droplet velocities and LDA to measure mean and fluctuating velocities of the continuous phase. Evaporating sprays were studied by Solomon et al. (45), while measurements of combusting monodisperse droplets were reported by Shuen et al. (46 and 47): LDA was used to measure velocities of both the droplets and the continuous phase in both these studies.

The above experimental studies show that particles or drops exert an influence on the continuous phase, decreasing the spreading rate of the jet and the centerline velocity decay of the continuous phase. The size of the particles, as well as the loading ratio, had an effect on the interaction between the turbulent continuous phase and the particles.

Previous studies of particle-laden swirling flows are relatively scarce, e.g., no experimental studies could be found in the literature. A few numerical studies have been reported (48 to 51). During and Suo (48) obtained solutions for particle trajectories in a free-vortex swirling flow. Domingos and Roriz (49) predicted the trajectories of evaporating or burning droplets in known gas flowfields. Seleznev and Tsvigan (50) performed numerical computations for a swirling gas with condensed droplets in an expanding channel, treating the gas and droplets as interpenetrating media. Finally, Hamed (51) reports particle trajectory calculations in a flow field with swirling vanes. Effects of particle impacts against the swirler vane surfaces were considered, however, interactions between particle trajectories and the gas phase were ignored. More details concerning computer models of two-phase flow will be discussed in the next section.

1.2.3 Analysis of Particle-Laden Flow

Various computer models have been developed for two-phase flows. One-dimensional and lumped-parameter models are discussed in an earlier review by Faeth (52) and will not be considered here. Subsequent reviews of recent two-phase flow models, applicable to sprays, have also been presented by Faeth (53 and 54).

1.2.3.1. LHF models. - There are two major types of two-phase flow models. The first involves use of the locally-homogeneous-flow (LHF) approximation where the drops or particles and the gas phase are

treated essentially as a single phase. Interphase transport rates are assumed infinitely fast under the LHF approximation; therefore, both phases have the same temperature and velocity and are also in phase equilibrium at every point in the flowfield. The LHF model corresponds to a single-phase variable density flow. The LHF approximation is strictly accurate only at the limit of infinitely small particles.

LHF models have been extensively used to predict two-phase flows because of their relative simplicity and the modest information required to specify initial conditions, e.g., detailed specifications of initial conditions for the particles are not required.

LHF analysis of a variety of two-phase flows can be found in Refs. 38-47 and 52-56. In general, effects of finite interphase transport rates usually resulted in LHF model predictions that overestimated the rate of development of the flow. LHF model predictions were only satisfactory for flows containing small tracer particles, where characteristic response times of the particles were small in comparison to all characteristic response times of the continuous phase.

1.2.3.1. SF models. - The second type of model considers finite transport rates between the phases and is termed a separated-flow model. Many separated-flow (SF) models have been proposed. A few are described in Refs. 38 - 49 and 51 - 54, and 57 - 73.

According to a recent review by Crowe (57), separated-flow models of dilute particle-laden gas flows can be divided into two groups, two-fluid and Lagrangian models. Two-fluid models regard the conveying and particulate phases as two interactive fluids similar to the two species in a binary mixture. A major disadvantage of this approach is that in order to consider more than one particle size, each size category must be treated as a separate fluid. This can demand a considerable amount of computer storage. An example of the two-fluid approach is given by Melville et al. (58). The Lagrangian approach is based on the "Particle-Source-In-Cell" (PSIC) technique reported by Sharma and Crowe (59). The PSIC approach is based on treating the particles as sources of mass, momentum, and energy to the gaseous phase. Particle trajectories are calculated in conjunction with a Eulerian continuous-phase solution.

An advantage of Lagrangian trajectory calculations is the absence of numerical diffusion of the particles. If the Lagrangian calculation is carried out using mean values of the continuous phase, the particles follow deterministic trajectories similar to the behavior of particles in a laminar flow. This type of analysis is termed a deterministic separated flow (DSF) model. Examples of DSF models are given in Refs. 38 - 47 and 53 - 54. In general, DSF models tend to underestimate the rate of dispersion of the particle phase. In addition, no information regarding the statistical properties of the particle phase is provided by a DSF model.

Various methods have been considered in order to treat the dispersion of particles by the turbulent fluctuations of the continuous phase. One method, first proposed by Jurewicz (60), is to use an effective diffusion force that is dependent on the particle concentration gradient in the particle motion equation. This requires an effective diffusion coefficient for which no reliable information is currently available. Another technique used to model the turbulent dispersion of particles is based on Monte Carlo methods and is termed the stochastic separated flow (SSF) method. In the SSF approach, the turbulent gas-phase flow field is modeled as a steady flow with superimposed random velocity fluctuations. Particle trajectories are then computed by randomly sampling the turbulent properties of the gas-phase flow field. This procedure eliminates the need for an effective diffusion coefficient, however many particles must be considered in order to provide a valid statistical sample.

A number of methods have been employed to model the mean flow and turbulence properties of the continuous phase for SSF models. Some applications of the SSF approach used simplified descriptions or empirical correlations of turbulence properties (61 - 63). More comprehensive treatments have utilized a turbulence model to provide the instantaneous properties of the continuous phase. Peskin and Kau (64) simulated a particle-laden flow in a rectangular channel using a large-eddy simulation (LES) model. The LES turbulence model involves

simulation of the three-dimensional, time-dependent, Navier-Stokes equations which requires substantial computer time. The well-known two-equation $k-\varepsilon$ turbulence model, developed at Imperial College (74), has been used most often (38 - 47, 53, 54, 65 - 67). This is due to the lack of versatility of algebraic models, the substantial computational requirements of LES, and the relatively early state of development of algebraic stress and full Reynolds-stress turbulence models. A coherent body of research on two-phase flows is reported in Refs. 37 - 47. SSF model predictions based on the $k-\varepsilon$ turbulence model and the turbulent dispersion approach first proposed by Gosman and Ioannides (66) are presented for a variety of two-phase flows. The present work extends the methods reported in Refs. 37 - 47 to weakly swirling jets.

1.3. Specific Problem Statement

Information on the structure of two-phase, turbulent, weakly swirling jets is needed to improve our understanding and advance methods of analysis of two-phase flows.

The previous review of the literature has shown that significant progress has recently been made toward developing methods of estimating the properties of two-phase flows. However, the rate of development of two-phase flow models has outpaced available experimental data. In particular, no data are currently available for two-phase flows with swirl. Since swirling flows have many important practical applications, this is an important area of research.

The present study seeks to provide new information concerning swirling particle-laden flows. Measurements of mean and fluctuating properties of both the continuous and dispersed phases were undertaken in turbulent, weakly swirling jets. Predictions were also undertaken, based on locally homogeneous flow, deterministic separated flow and stochastic separated flow models that are typical of their current state of development. The predictions were used to help interpret the measurements and to initiate evaluation of methods to analyze swirling particle-laden flows. Specific objectives of the study were as follows:

1. Measure the structure of particle-laden weakly swirling jets injected into stagnant air. Measured properties include: mean and fluctuating velocities of both phases, and the distribution of particles in the flow field.

2. Modify existing locally homogeneous flow, deterministic separated flow and stochastic separated flow models of dilute particle-laden flows so that they can be applied to weakly swirling flows.

3. Compare model predictions with experimental data obtained during the present study and use these results to interpret measurements and to guide further model development.

Measurements were limited to relatively monodisperse, dilute, particle-laden free jets. This allowed the use of nonintrusive laser-based methods for velocity measurements of both phases, since

spurious scattering of the laser beams was modest and particle size was known. Boundary conditions for the experiment were well defined. Experiments were conducted by injecting an air jet containing solid glass spheres downward from a long tube into stagnant air at ambient temperature and pressure. Swirl was imparted to the jet by tangential air injection and was varied in order to determine its effect. Initial conditions for both phases were measured as completely as possible, to facilitate calculations of flow properties.

CHAPTER II

EXPERIMENTAL METHODS

2.1 Introduction

Measurements were obtained in both single-phase and particle-laden jets. The flows examined during the present study have properties as follows:

(1) Three isothermal single-phase jets (with swirl numbers of 0, 0.19, and 0.33).

(2) Three particle-laden jets (with a particle SMD of 39 μm, loading ratio of 0.2, and swirl numbers of 0, 0.16, and 0.3).

A variety of measurements were undertaken in order to study the flows. Axial and radial profiles of mean and fluctuating velocities for both phases and mean particle mass fluxes were measured. Initial conditions were measured at $x/d = 0.5$. Additional measurements involved particle size distributions.

2.2 Experimental Apparatus

2.2.1 General Arrangement

A schematic drawing of the experimental arrangement is illustrated in figure 2.1. The flow consists of a turbulent, weakly swirling particle-laden jet discharging vertically downward into a stagnant environment. Swirl numbers of the jets were less than 0.4, calculated from equation (1.1), in order to avoid the appearance of a

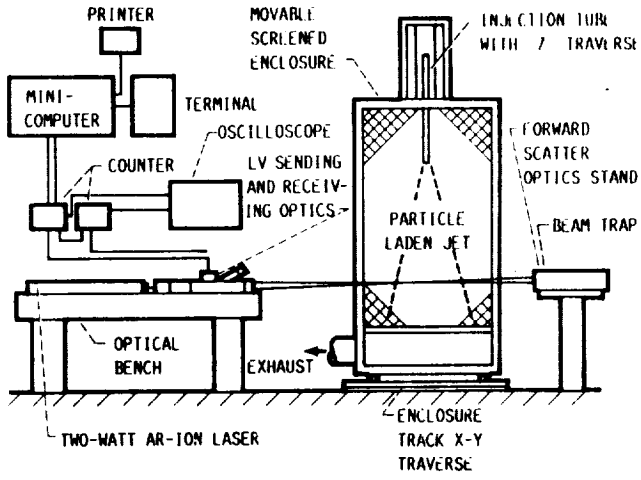

Figure 2.1. - Experimental arrangement.

recirculation zone (15). As a result, the flows could be treated using the boundary-layer approximations. The boundary-layer approximations have previously been applied successfully to these flows (10, 11, 15, 16, 18 and 22), even though initial rates of radial spread are relatively high. This arrangement provides an experiment with a relatively simple geometry and well-defined boundary conditions, which is also computationally tractable.

The single-phase and particle-laden jets discharged from a round tube (19 mm inside diameter) that was 1900 mm long, in order to provide a fully developed turbulent flow at the discharge plane. The injection tube was mounted inside a cage that was 1.8 m square at the base and 2.4 m high. The cage was completely enclosed with one layer of 16 mesh screen (wire diameter 0.41 mm, open area 55.4 percent) to protect the jet from room disturbances. The jet was exhausted to the outside using a roof-mounted, variable-speed blower whose inlet was roughly 1 m below the measuring plane. The exhaust line (250 mm in diameter) began 350 mm below a 60 mesh screen (1.2 x 1.2 m screen with wire diameter of 0.28 mm and an open area of 11.7 percent) which acted as the inlet to the exhaust system. Velocity measurements at the measurement plane, with the exhaust system operating and no jet flow, indicated an induced velocity of less than 0.2 m/s from the exhaust blower; therefore, it was concluded that the exhaust system had a negligible effect on measurements within the jet flows.

Most measurements involved optical diagnostics which were rigidly mounted; therefore, the entire cage and injector were traversed to measure properties at various points in the flow. The cage was mounted on two sets of linear bearings in order to provide movement along two axes in the horizontal plane. Positioning was accomplished using two, 1220 mm long, Unislide assemblies (B6048P20J), driven by stepper motors (Slo-Syn M093). Positioning accuracy was estimated to be ±0.1 mm. To measure properties at various axial locations, the tube from which the jet discharged was traversed vertically using a 1.3 m long Unislide (B6051P20J) driven by a stepper motor (Slo-Syn M093). Positioning accuracy in the vertical direction was also estimated to be ±0.1 mm. All three stepper motors were controlled by a microcomputer driver (Velmex 8300).

The particles used in the experiments were solid glass spheres manufactured by N.T. Ruddock Company. They had a density of 2500 kg/m^3 and a refractive index of 1.51. The particles were manufactured for use in this study and were used as received. The particle size distribution for a sample of 1567 particles is illustrated in figure 2.2. Particle size was measured using a Cambridge Instruments Quantimet 900 image analyzer. The calculated SMD for this distribution was 39 μm with a standard deviation of 15 μm. The average mean diameter of this distribution was calculated to be 30 μm.

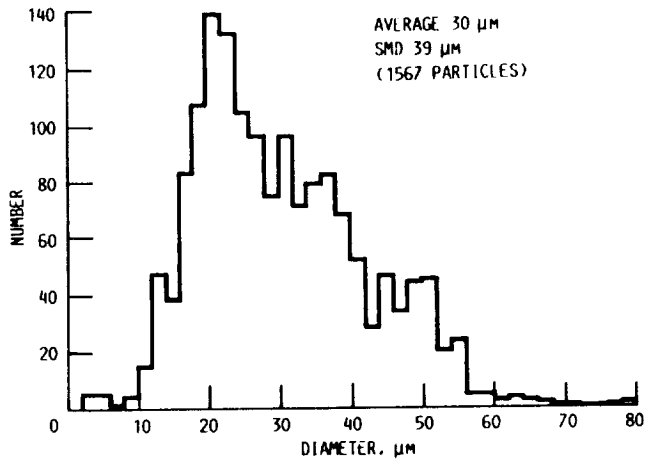

Figure 2.2. - Particle size distribution.

2.2.2 Flow system

A sketch of the flow system is illustrated in figure 2.3. Compressed air, supplied at approximately 860 kPa, was passed through two coalescing filters (Balston 62A-1), mounted in series, to remove contaminants. The flow was then separated into three streams that were used for the main airflow, the swirl airflow, and a flow which was seeded for laser velocimetry (LV) measurements. The flow rates of the main and swirl air streams were measured using calibrated, round, critical-flow orifices. Various combinations of four orifices (2.286, 1.27, 1.092 and 0.762 mm in diameter) were used to provide the required flowrates. The air flow rate was adjusted by varying the pressure on the upstream side of each orifice, using pressure regulators (Conoflow Model H40-Xt-HXA). Upstream pressures were measured using calibrated strain gage pressure transducers (MBIS C-64952-D, 0-689.5 kPa). The static pressure drop across each orifice was measured using calibrated strain gage differential pressure transducers (Bell and Howell, 4-351-0210, ±689.5 kPa) and checked to insure that each orifice was choked at all operating conditions. The air temperature upstream of each orifice was measured using 3.2 mm diameter closed-end Chromal-Alumel thermocouples, inserted into the center of the tube and connected to a Doric Scientific Series 400 readout.

The main air flow was seeded with aluminum oxide particles, nominally 1 μm in diameter, (Baikalox 1.0 CR) to allow LV measurements

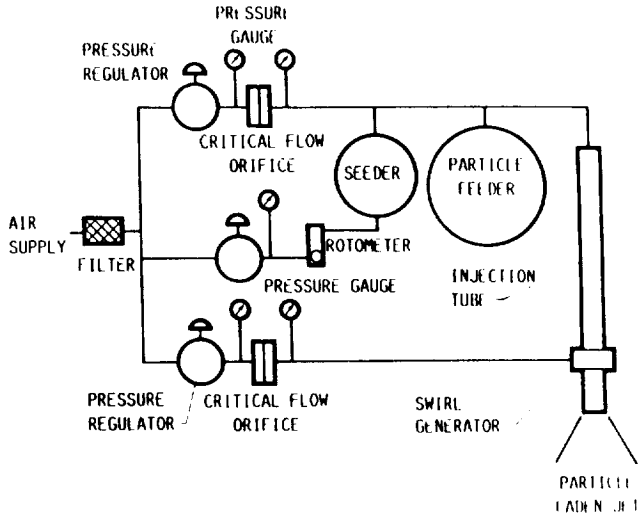

Figure 2.3. - Sketch of the flow system.

of continuous phase velocities. For the single-phase jets, the seeding particles were mixed into the airflow using a fluidized-bed particle generator (TSI Model 3400). For the particle-laden flows, a reverse cyclone seeder, described by Glass and Kennedy (75), was used in order to provide increased seeding levels. The air flow rate to either seeder was measured using a calibrated Brooks rotometer (Tube size R-6-15-B). The inlet pressure of the seeder was adjusted using a pressure regulator (Conoflow Model H40-XT-HXA).

Particles were introduced into the main air stream using a vibrating, variable-speed, screw feeder (Vibra-Screw live bin feeder) with a 9.53 mm diameter screw. The screw discharged the particles into a tapered tube where they were allowed to drop downward into the main flow. The static pressures inside the particle feeder and the main air line were equalized at the particle entry position. A 45 m long, 3.18 mm inside diameter, tube was used to damp out any pressure oscillation caused by the introduction of the particles. Particle flowrates were measured by calibration of the feeder screw speed.

The surroundings of the jet were also seeded with nominal 1 μm diameter aluminum oxide particles using a separate air supply line and a fluidized bed aerosol generator (TSI 9310).

2.2.3 Swirl Generator

A sketch of the swirl generator is illustrated in figure 2.4. Swirl was generated by introducing air tangentially into the injection

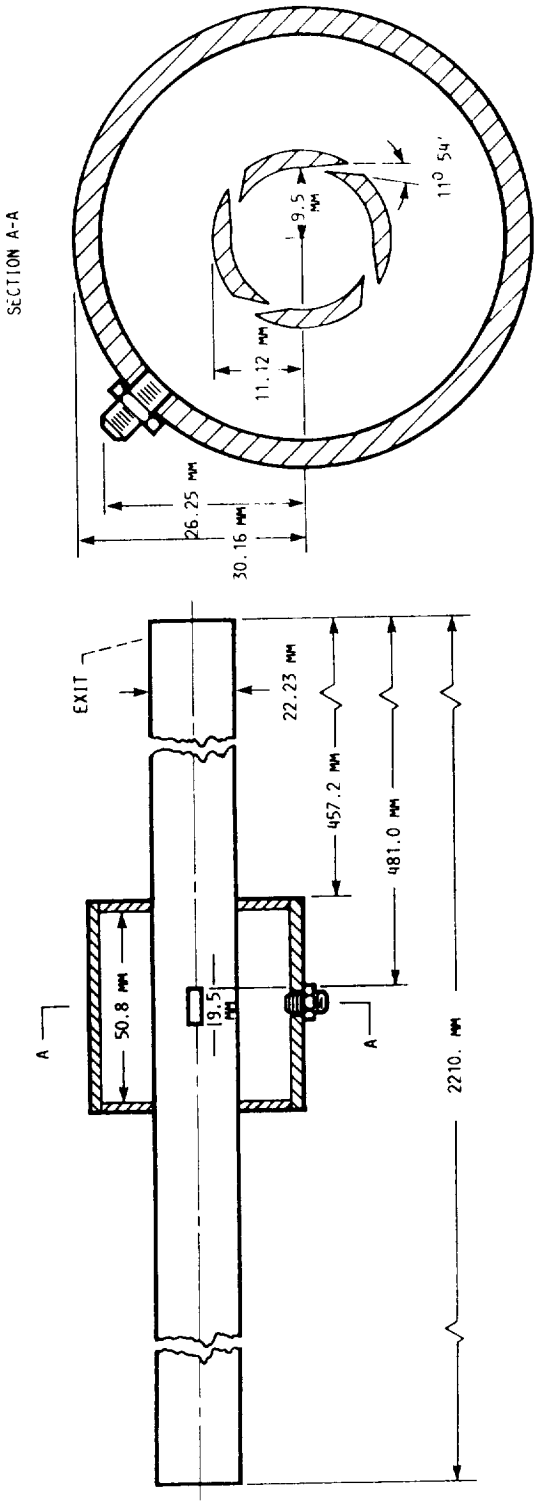

Figure 2.4 - Swirl generator and injection tube.

tube through four identical 9.5 mm long slots located 90° apart. This approach for generating swirl has been previously reported by a number of investigators (6-11) and was found to yield reasonably good results during the present study. The slots were fed from a 62 mm inside diameter plenum, to insure equal flowrates through each slot. The leading edge of the slots was located 25 diameters upstream of the injection tube exit. The swirl number of the jet is varied by changing the flowrate of the tangential air flow.

2.3 Instrumentation

2.3.1 Single-Phase Jet Velocities

The mean and fluctuating velocities of the single-phase jets were measured using a two-channel laser velocimeter (LV). A sketch of the arrangement appears in figure 2.5. Major components of the system are summarized in table 2.1.

The output beam from a 2 W Argon-Ion laser was separated into green (514.5 nm) and blue (488 nm) beams. Each beam was then split into two beams to provide a four-beam backward-scatter LV. This allowed simultaneous measurement of velocity and Reynolds stress in two directions. One beam from each color was frequency shifted (40 MHz with electronic downshifting) to optimize the frequency range and to reduce fringe bias. Beam expansion was used to increase the signal-to-noise ratio (SN) and to improve spatial resolution. The sending/collecting lens had a focal length of 762 mm. Theoretical

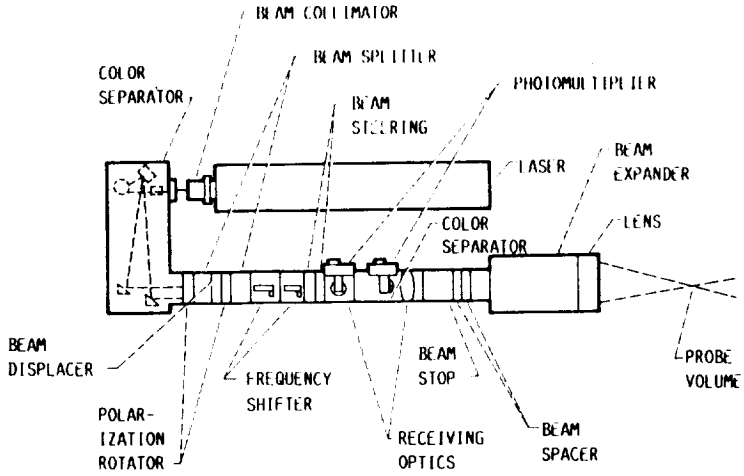

Figure 2.5. - Two-channel LV system.

Table 2.1 - Summary of LV Components for Single-Phase Jet Measurements

Component	Manufacturer	Model	Specification/function
Argon-ion laser	Lexel	95-2	2.0 W; multiline mode 1.3 mm (e^{-2} points) beam diameter
Beam collimator	TSI	9178	
Color separator	TSI	9105	
Polarization rotator	TSI	9102-11 9102-12	Blue (488 nm) beam Green (514.5 nm) beam
Beamsplitter	TSI	9115-1	50 mm beam spacing
Beam displacer	TSI	9174	25 mm beam offset to center
Frequency shifter	TSI	9182-11 9182-12	Bragg cell, 2 kHz-40 MHz shift frequency
Beam steering	TSI	9175	
Receiving assembly	TSI	9140	200 mm focal length detector lens; 98 percent reflectivity dielectric multilayer mirror at 45° incident angle
Color separator (scattered light)	TSI	9145	dichroic mirror efficiency 514.5 nm transmitted 85 percent 488 nm reflected 95 percent
Beam stop	TSI	9181	
Beam spacer	TSI	9113-22	Reduces beam spacing from 50 mm to 22 mm
Beam expander	TSI	9189	3.74 expansion ratio
Transmitting/ receiving lens	TSI	9169-750	762 mm focal length 152 mm clear aperature
Photomultiplier system	TSI	9160	0.2 mm aperature
Burst counter	TSI	1990-B	
Digital direct memory access interface	TSI	1998-D	
Oscilloscope	Tektronic	7834	
Data acquistion/ processing	DEC	Minc 11/23	

parameters for this system, fringe spacing, measuring volume size, etc., are summarized in table 2.2.

Detector signals were processed using two burst counters. An oscilloscope was used to monitor the detector and burst counter output signals. The counters were operated in the total burst mode, with a coincidence check to insure that the signals obtained from both probe volumes were from the same seeding particle. Valid data rates were generally in the range of several hundred per second. The digital output of the counters was sent to a Minc 23 microcomputer, using a direct memory access board and a TSI interface (model 1998D). Data from the counters was processed using a Thermo-Systems computer program. The computer program included a residence time weighting scheme to minimize effects of velocity bias on the results. Results presented are based on at least 2400 velocity samples. Possible sources of error and experimental uncertainties for measurements of gas velocities in the single-phase jets are discussed in Appendix A. Experimental uncertainties (95 percent confidence) are as follows: mean streamwise velocities, less than 5 percent; mean angular velocities, typically less than 20 percent; velocity fluctuations, less than 5 percent; k, less than 12 percent; and the Reynolds stress, 14 percent at the maximum Reynolds stress and proportionately higher elsewhere.

Table 2.2 - LV Theoretical Parameters

Parameter	Green (514.5 nm)	Blue (488 nm)
Single-phase Jets (backscatter):		
Fringe spacing, μm	4.76	4.51
Probe volume diameter, μm	102	99
Receiver measuring volume diameter, μm	762	762
Probe volume length, μm	1891	1838
Receiver measuring volume length, μm[a]	103	101
Number of fringes	22	22
Dispersed phase 30° off-axis (forward scatter):		
Fringe spacing, μm	4.76	4.51
Probe volume diameter, μm	102	99
Receiver measuring volume diameter, μm[b]	685	685
Probe volume length, μm	1891	1838
Receiver measuring volume length, μm[b]	283	277
Number of fringes	22	22

[a]Calculated using depth of field limit.
[b]Includes diameter of largest particle expected.

2.3.2 Particle - Laden Jet Velocities

2.3.2.1 Particle Velocities. - Mean and fluctuating velocities of the dispersed phase were measured using both a two-channel LV and a phase/Doppler anemometer. The LV system yielded particle velocities averaged over all particle sizes present while the phase/Doppler particle anemometer measured both particle size and velocity.

The arrangement of the LV system used to measure particle velocities was similar to the LV system used to measure velocities in the single-phase jets, except that the receiving optics were moved to 30° off-axis in the forward scatter direction. A receiving lens with a focal length of 602.4 mm and a clear aperture of 60 mm was used to collect scattered light from the particles. Estimated dimensions of the probe volume for this arrangement are also shown in table 2.2. To account for particles grazing the probe volume, the dimensions shown in table 2.2 were obtained by adding the diameter of the largest particle expected to the calculated theoretical diameter. Since actual probe volume size is a strong function of scattering particle size, laser power and photodetector gain setting, these values should not be strictly regarded as quantitative.

The counters were operated in the total burst mode, however, a coincidence check was not required for this measurement (cross correlations were not required). The values obtained were number averages over all sizes of particles present in the flow. A residence time weighting correction was not applied or required, since only

number averages are meaningful for the dispersed phase. The continuous phase was not seeded with aluminum oxide particles for these measurements and laser power and detector gain were also reduced to further insure that only signals from particles were processed. Valid data rates for particles varied considerably depending on where the flowfield was sampled. Each data point presented in the following represents at least 5000 samples.

Possible errors and uncertainties for the particle velocity measurements are discussed in Appendix A. Experimental uncertainties (95 percent confidence) are as follows: $\overline{u}_p$, less than 5 percent; $\overline{v}_p$, typically less than 10 percent (at x/d = 0.5); $\overline{w}_p$, less than 6 percent at the maximum and proportionately higher elsewhere; and fluctuating particle velocities, less than 5 percent.

The arrangement of the optical system for the phase/Doppler particle anemometer is illustrated in figure 2.6. Major components are summarized in table 2.3. The beam from a 2 W Argon-Ion laser was separated into green (514.5 nm) and blue (488 nm) beams. Only the green beam was used for these measurements. The beam was expanded by a factor of three before being split into two beams which were then focused and crossed with a 602.4 mm focal length lens. Scattered light was collected 30° off axis in the forward direction with a 495 mm focal length lens. The fringe spacing for this optical configuration was 6.3 μm. Estimated dimensions of the measuring volume are as follows: diameter of 100 μm, and a length of 202 μm. These

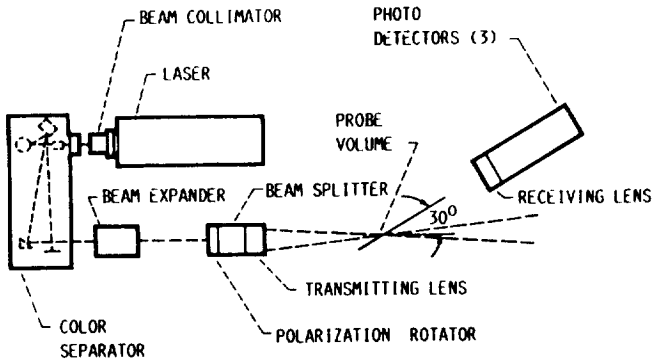

Figure 2.6. - Single-channel phase/Doppler particle anemometer.

Table 2.3 - Summary of Components for Phase/Doppler Particle Anemometer

Component	Manufacturer		Specification/function
Argon-ion laser	Lexel	95-2	2.0 W, multiline mode; 1.3 mm (e^{-2} points) beam diameter
Beam collimator	TSI	9178	
Color separator	TSI	9105	
Beam expander	Melles Griot	09 LBM 001	3.0 expansion ratio
Polarization rotator	TSI	9102-12	
Beamsplitter	TSI	9115-1	50 mm beam spacing
Transmitting lens	TSI	9119	602.4 mm focal length 2.34° half angle
Receiving lens	Aerometrics		495 mm focal length
Receiver assembly	Aerometrics	2100	50 μm slit width 240 mm focal length detector
Processor	Aerometrics	PDP 3100	
Data acquistion/ processing	IBM	P.C.	

measurements do not include the diameter of the largest particle. The collected light was focused onto a slit (50 μm wide by 1 mm long) using a 240 mm focal length lens. Three detectors, separated by fixed spacings, were used to detect the Doppler burst signals. The phase shift in the signal detected by the three detectors is proportional to particle size and this shift can be used to determine particle size. Since this method also yields particle velocity in the same manner as a laser velocimeter, a simultaneous particle size and velocity measurement is obtained. Details of the theory and experiments to validate the instrument can be found in (76, 77).

Data from the PDP3100 processor was processed using an IBM PC computer. The processor considered the entire Doppler burst for the data processing. The velocity data reported are number averages for each size group and no corrections were applied to account for velocity biasing. The actual number of samples considered for each velocity measurement varied depending upon position in the flowfield and particle size. Errors and uncertainties of the phase/Doppler measurements are discussed in Appendix A. The uncertainties (95 percent confidence) are estimated to be less than 5 percent for mean and fluctuating streamwise velocities, similar to the single-phase jet measurements.

2.3.2.2 Continuous Phase Velocities. - Mean and fluctuating velocities of the continuous phase in the presence of particles were measured using the single-channel phase/Doppler particle anemometer.

As previously discussed, this instrument measures particle size and velocity simultaneously. To measure continuous-phase velocities in the presence of particles, the continuous phase was seeded with nominal 1 μm diameter aluminum oxide particles and the corresponding velocity measurement for that size was assumed to represent the continuous phase. A reverse cyclone seeder, similar to that described by Glass and Kennedy (75), was used to introduce the aluminum oxide powder, since it provided increased seeding levels over the smaller fluidized-bed seeder used previously for velocity measurements in the single-phase flows.

By appropriate seeding of the continuous phase with the nominal 1 μm diameter aluminum oxide particles, the phase/Doppler particle anemometer was used to measure continuous-phase velocities in the presence of the solid particles. An example of a typical data point taken with the instrument is shown in figure 2.7. In figure 2.7, two distinct size distributions are clearly evident. The smallest particles (~1.9 μm) are due to the continuous-phase seeding, while the larger particles correspond to the dispersed phase. The actual number of samples considered for each velocity measurement varied depending upon position in the flowfield, but at least 1000 samples were used for each continuous-phase data point. The velocity data reported are number averages and no corrections were applied to account for velocity biasing.

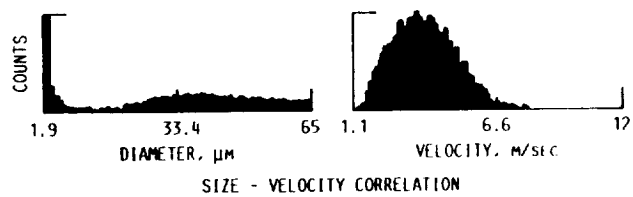

Figure 2.7. - Typical simultaneous size and velocity data taken at a point in particle-laden flow.

2.3.3 Particle Mass Flux

The mass flux of the dispersed phase was measured using an isokinetic sampling probe. The probe used was similar to that reported by Szekely (78). A sketch of the probe appears in figure 2.8. The probe was constructed using a Gelman 2220 stainless steel in-line filter holder. The probe is shown with a 2 mm inside diameter tip. Probe tips were interchangable and a tip with an inside diameter of 5 mm was also used. For the larger diameter probe, the height of the probe was reduced from 12.6 to 6.9 mm to increase the inlet diameter. Two probe inlet diameters were required in order to insure adequate spatial resolution and reasonable sampling times in all regions of the flow. The probe was rigidly mounted on a metal bar attached to a fixed optical table. The cage and injector tube assembly was traversed to sample various locations in the flow.

A sketch of the particle mass-flux measurement system is shown in figure 2.9. A W.M. Welch Duo-Seal vacuum pump was used to withdraw samples isokinetically through the probe. Particles were collected on a Gelman membrane filter (No. 64679, 0.8 μm pore size) for a timed interval and weighed on a digital scale (Mettler PC 2000), accurate to 0.01 g. The sampling interval was timed using an Adanac stopwatch. Sampling probe flow rates were controlled using a needle valve in the probe sample line and a second needle valve in a bypass line. Flowrates were measured using one of three calibrated rotometers (Cole Parmer FM102-05, FM082-03, FM034-39), arranged in parallel. Using

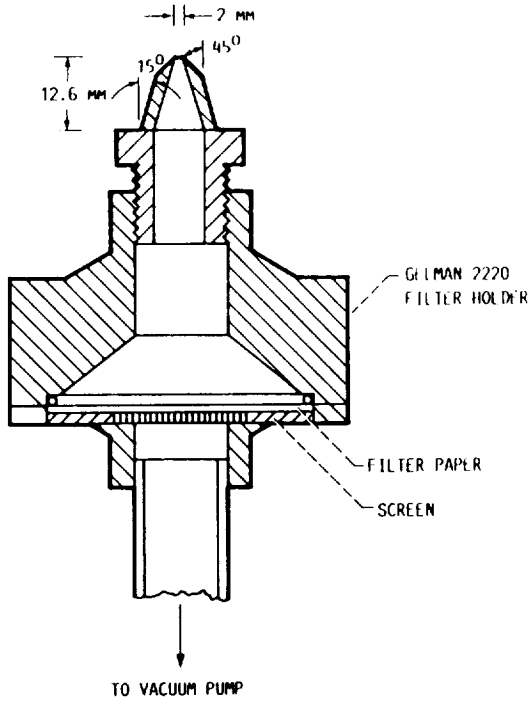

Figure 2.8. - Particle mass flux sampling probe.

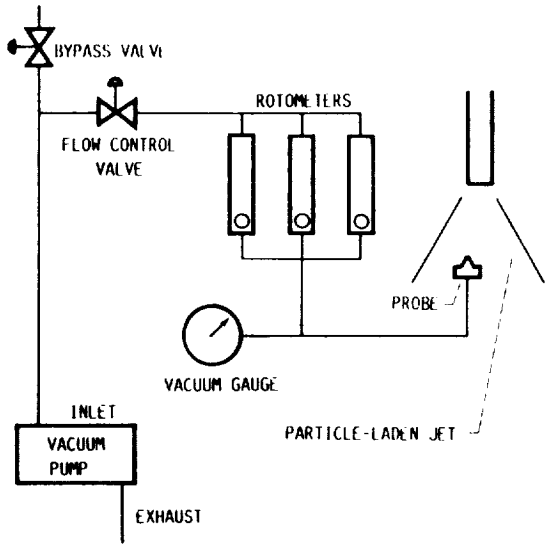

Figure 2.9. - Particle mass flux measurement flow system.

this sampling system, measured particle mass fluxes integrated across the jet were within ±10 percent of the calibrated feeder flow rate at all axial locations. This system was relatively insensitive to the effect of gas-sampling rates. Small variations in sampling rates above and below the mean isokinetic velocity had a negligible effect on the results. Experimental uncertainties for the particle mass flux measurements (95 percent confidence) are estimated to be less than 8 percent, as discussed in Appendix A.

2.4 Test Conditions

Test conditions are summarized in table 2.4. Three single-phase and three particle-laden jets were studied. Swirl numbers were limited to 0.33 or less in order to avoid recirculation zones; therefore, the swirling flows could be classified as weakly swirling flows. A single loading ratio, defined as the ratio between the injected particle mass flow rate and the air mass flow rate, of 0.2 was studied. Based on an average particle size of 30 μm, the spacing between particles at the exit of the tube was about 20 particle diameters. Particles with an SMD of 39 μm were used for all particle-laden flows. The standard deviation of the particle distribution was 15 μm. The average diameter of the particles was 30 μm. The flows were fully turbulent, with initial Reynolds numbers of approximately 20,000 -- based on the total jet momentum per unit mass flow rate and the tube diameter.

Table 2.4 - Summary of Test Conditions[a]

Parameter	Single-phase jets			Particle-laden jets		
	Case 1	Case 2	Case 3	Case 1	Case 2	Case 3
Centerline air axial velocity, m/s[b]	14.86	12.94	13.34	13.75	11.9	12.2
Maximum air angular velocity, m/s[b]	0	3.16	5.92	0	-----	-----
Swirl number[c]	0	.19	.33	0	.16	.3
Centerline particle axial velocity, m/s[b]	-----	-----	-----	13.8	10.39	10.26
Maximum particle angular velocity, m/s[b]	-----	-----	-----	0	1.48	2.26

[a]Ambient temperature and pressures, 296 K, 97 kPa; injector inside diameter, 19 mm; for particle-laden jets, particle SMD of 39 μm, particle mean diameter of 30 μm, particle density of 2500 kg/m^3, and particle loading ratio of 0.2.
[b]Measured at x/d = 0.5.
[c]Calculated from equation (1.1).

Structure measurements were made for $x/d \leq 30$ for flows without swirl and $x/d \leq 20$ for the swirling flows. For the particle-laden flows without swirl, radial profiles of flow properties were measured at $x/d = 0.5$, 5, 15, and 30. For the particle-laden swirling flows, radial profiles were measured at $x/d = 0.5$, 2, 5, 10, and 20.

CHAPTER III

THEORETICAL CONSIDERATIONS

3.1 General Description

The analysis is limited to a steady, axisymmetric, dilute, solid-particle-laden, weakly swirling, turbulent jet in an infinite, stagnant media. The swirl number, calculated from equation (1.1), is restricted to values of approximately 0.5 or less so that adverse pressure gradients caused by the decay of angular velocity are not strong enough to induce a reversal of the axial velocity. The boundary-layer approximations are assumed to be valid; however, the radial pressure gradient, which is usually neglected in the boundary-layer analysis, is considered. The k-ε turbulence model is used to provide closure since this approach has modest computational requirements. Effects of streamline curvature on the k-ε turbulence model are considered. The injector exit Mach number is less than 0.3; therefore, kinetic energy and viscous dissipation of the mean flow are neglected with little error.

Three methods of treating multiphase flow, typical of current practice, are considered, as follows: (1) locally homogeneous flow (LHF), where interphase transport rates are assumed to be infinitely fast and the flow can be treated like a single-phase, variable-density

fluid; (2) deterministic separated flow (DSF), where finite interphase transport rates are considered, but the dispersed phase is assumed to interact only with the mean properties of the continuous phase e.g., particle/turbulence interactions are ignored; and (3) stochastic separated flow (SSF), where both finite interphase transport rates and effects of particle/turbulence interactions are considered, using random-walk methods. All three methods will be discussed in more detail in the following sections.

3.2 Locally Homogeneous Flow

3.2.1 Governing Equations

3.2.1.1 Baseline Version. - Since both phases move at the same velocity under the LHF approximation, this approach treats the flow as a single-phase turbulent fluid with density variations caused by changes in the concentration of the dispersed phase, even though the densities of each phase are constant. Following Bilger (79), Favre (mass)-averaged quantities are used rather than Reynolds (time)-averaged quantities. As discussed by Bilger (79) and Bradshaw, et al. (80), Favre averaging offers advantages for variable density flows because numerous terms involving density fluctuations are eliminated from the governing equations.

Mean (mass averaged) quantities are found by solving governing equations for conservation of mass, momentum, and mixture fraction. The mixture fraction, f, was defined as the mass fraction of particles in the flow. If the diffusivities of both phases are the same, the

mixture fraction becomes a conserved scalar, as described in (79), and all scalar properties are only functions of mixture fraction. The equations are closed using the well-known, two-equation, k-ε turbulence model.

The general form of the governing equations in cylindrical coordinates is as follows:

$$\frac{\partial}{\partial x}\left(\bar{\rho}\tilde{u}\tilde{\phi}\right) + \frac{1}{r}\frac{\partial}{\partial r}\left(r\bar{\rho}\tilde{v}\tilde{\phi}\right) = \frac{1}{r}\frac{\partial}{\partial r}\left\{r\left(\mu + \frac{\mu_t}{\sigma_\phi}\right)\frac{\partial \phi}{\partial r}\right\} + S_\phi \qquad (3.1)$$

where ϕ denotes a Favre-averaged variable, defined as follows:

$$\tilde{\phi} = \frac{\overline{\rho\phi}}{\bar{\rho}} \qquad (3.2)$$

The source terms, S_ϕ, appearing in equation (3.1) are summarized in table 3.1 along with empirical constants established by Jeng (81) for a variety of constant and variable density single-phase jets. The approach, and the empirical constants, however, are not very different from early proposals at Imperial College (74). The governing equation for radial momentum does not fit the form of equation (3.1) and is given later.

Table 3.1. - Source Terms and Empirical Constants used in Equation (3.1)

ϕ	S_ϕ
1	0
$\tilde{u}$	$-\frac{\partial \bar{p}}{\partial x}$
$r\tilde{w}$	$-\frac{1}{r}\frac{\partial}{\partial r}\left\{\left(\mu + \mu_t\right) 2r\tilde{w}\right\}$
$\tilde{f}$	0
k	$\mu_t\left\{\left(\frac{\partial \tilde{u}}{\partial r}\right)^2 + \left[r\frac{\partial}{\partial r}\left(\frac{\tilde{w}}{r}\right)\right]^2\right\} - \bar{\rho}\varepsilon$
ε	$C_{\varepsilon 1}\mu_t \frac{\varepsilon}{k}\left\{\left(\frac{\partial \tilde{u}}{\partial r}\right)^2 + \left[r\frac{\partial}{\partial r}\left(\frac{\tilde{w}}{r}\right)\right]^2\right\} - C_{\varepsilon 2}\bar{\rho}\frac{\varepsilon^2}{k}$

C_μ	$C_{\varepsilon 1}$	$C_{\varepsilon 2}$	σ_k	σ_ε	σ_f
0.09	1.44	1.87	1.0	1.3	0.7

Equation (3.1) is classified as parabolic and was obtained using the usual boundary-layer assumptions. Axial gradients are assumed to be negligible compared to radial gradients, and turbulent correlations are all of the same order of magnitude. Thus, the radial dimensions of the flow are assumed to be much smaller than the axial dimensions, $r/x \ll 1$. Swirling flows exhibit fairly high spreading rates; therefore, the width of a swirling jet can be as large as 30 or 40 percent of the axial dimension (11). Nevertheless, the boundary-layer equations have been applied to weakly swirling flows (swirl numbers up to about 0.5) (8, 10, 11, 16, 18, 22), and this approach is adopted here as well.

In addition to the boundary-layer assumptions, a number of other assumptions are made in the derivation of equation (3.1). The flow is considered to be fully turbulent. Terms involving molecular viscous stress tensor fluctuations have been neglected, however, mean molecular stress is included even though it is considerably smaller than μ_t. Also, a term involving the fluctuating density, velocity, and mean pressure gradient has been neglected in both the k and ε equations in order to reduce the number of empirical constants.

A consequence of the presence of angular velocity is that even though the standard boundary-layer assumptions are made, the radial momentum equation is still present as

$$\frac{\partial \bar{p}}{\partial r} = \frac{\bar{\rho}\tilde{w}^2}{r} \tag{3.3}$$

and cross-stream pressure gradients are not negligible. Also, because of the decay of angular velocity with axial distance, the source term $\partial p/\partial x$ is included in the governing equation for axial momentum.

Under the conserved scalar approach, the instantaneous particle concentration and density are only functions of mixture fraction. The mixture fraction is the mass fraction of particles in the flow, as follows:

$$f = \frac{C_p}{C_a + C_p} \tag{3.4}$$

Using the adiabatic mixing approximation from Shearer and Faeth (55), the density of the mixture can be found from the following equation:

$$\rho = \left[\frac{\left(\rho_a - \rho_p\right) f + \rho_p}{\rho_a \rho_p} \right]^{-1} \tag{3.5}$$

The Favre averaged mean value of a scalar can be found from the following equation (79,81):

$$\tilde{\phi}(f) = \int_0^1 \phi(f)\tilde{P}(f)df \tag{3.6}$$

where $\phi(f)$ is the state relationship for the property, i.e., equation (3.5) in this case. Time-averaged density can be found from from the following equation (81):

$$\frac{1}{\bar{\rho}} = \int_0^1 \frac{1}{\rho} \tilde{P}(f)df \tag{3.7}$$

Since ρ^{-1} is a linear function of f in the domain $0 \leq f \leq 1$, mean values are independent of the form of the probability density function (PDF), $P(f)$, chosen and it is easily shown that $\overline{\rho} = \rho(\widetilde{f})$. Therefore, $\overline{\rho}_{mix}$ and $\widetilde{f}$ can be substituted in equation (3.5) to give $\overline{\rho}_{mix}$ as a function of $\widetilde{f}$.

The turbulent viscosity appearing in equation (3.1) was calculated from k and ε as follows (74):

$$\mu_t = C_\mu \overline{\rho} \frac{k^2}{\varepsilon} \tag{3.8}$$

The source terms given in table 3.1 for k and ε do not include effects of streamline curvature. This is considered in the next section.

3.3.1.2 Streamline Curvature Version. - As discussed in Refs. 82-88, streamline curvature has been shown to produce very large changes in the turbulence structure of shear layers. Bradshaw (82) presents a review of the effects of streamline curvature and discusses a basis for classifying shear flows as simple or complex. Shear flows, where there is only one significant rate-of-strain component, are classified as simple while those subjected to extra rates of strain due to additional velocity gradients are classified as complex.

Numerous modifications of the k-ε turbulence model have been proposed to account for effects of streamline curvature. All of the modifications are based on the hypothesis that the destabilizing effect of swirl can be modeled through an increase in the length scale

of the turbulent eddies. Sharma (83) and Leschziner and Rodi (84) report calculations of curved flow using the k-ε model, where one of the constants in the dissipation equation is made a function of the gradient Richardson number. Leschziner and Rodi (84) also reported results of calculations using a modified dissipation equation based upon a flux Richardson number. Hah and Lakshminarayana (85) report predictions of turbulent wakes using turbulence closure models that were modified for effects of streamline curvature. A modification to the dissipation equation, obtained by simplification of an algebraic Reynolds-stress model, was reported by Leschziner and Rodi (86) and found to yield reasonably good results. Komori and Ueda (87) and Leschziner and Rodi (84), however, reported reasonably good results for calculations of strongly swirling free jets with standard k-ε turbulence models as well.

A recent review paper by Lakshminarayana (88) discusses various turbulence models ranging from algebraic eddy viscosity models to models based on Reynolds-stress transport equations for complex flows. He states that "the field of turbulence modeling for complex flows is confusing and conflicting and that intuition and ad-hoc assumptions dominate the art of turbulence modeling in complex flows." Lakshminarayana (88) concludes that the standard k-ε model is not adequate for prediction of complex flows but modified k-ε models are probably adequate for very mildly complex flows. Since

weakly swirling free jets are mildly complex, modifications to the $k-\varepsilon$ model are considered in the present study.

Two modifications to the dissipation equations were evaluated during the present study. The first, discussed by Leschziner and Rodi (84), involves replacing $C_{\varepsilon 2}$ in table 3.1 with the following expression:

$$C^{*}_{\varepsilon 2} = C_{\varepsilon 2}(1 - 0.2\ R_i) \tag{3.9}$$

where R_i is a gradient Richardson number, which is defined as follows, for the present flows:

$$R_i = \frac{k^2}{\varepsilon^2}\frac{\tilde{w}}{r^2}\frac{\partial(r\tilde{w})}{\partial r} \tag{3.10}$$

This curvature modification performed poorly during the present study and no predictions using it are presented in the following.

The second modification of the dissipation equation also was taken from (84) and involves replacing one of the constants in table 3.1 by a functional relationship. In this case, $C_{\varepsilon 1}$ is replaced by the following expression:

$$C^{*}_{\varepsilon 1} = C_{\varepsilon 1}(1 + 0.9\ R_f) \tag{3.11}$$

where R_f is a flux Richardson number, defined in this case, as follows:

$$R_f = \frac{2\tilde{w}\left(\frac{\partial\tilde{w}}{\partial r}\right)}{\left(\frac{\partial\tilde{u}}{\partial r}\right)^2 + \left[r\frac{\partial}{\partial r}\left(\frac{\tilde{w}}{r}\right)\right]^2} \tag{3.12}$$

3.2.2 Numerical Solution

Equations (3.1) and (3.3) were solved using a modified version of the GENMIX computer code (89). A brief description of the formulation is given in Appendix B. Thirty-three cross-stream grid modes were used during all the calculations. For the nonswirling flows, streamwise step sizes were limited to 5 percent of the current flow width or an entrainment increase of 5 percent—whichever was smaller. For the swirling flows, streamwise step sizes were limited to 2 percent of the current flow width or an entrainment increase of 2 percent - whichever was smaller. Computations performed with streamwise step size decreased by a factor of 2, and with 66 cross-stream grid nodes, showed changes of less than 3 percent in the computed results at $x/d = 20$.

Because of the formulation of the GENMIX algorithm, consideration of angular velocity required modifications of the solution procedure. Downstream values of r, which are required to solve equation (3.2) for the radial pressure distribution (in order to calculate the axial pressure gradient), can only be calculated after downstream values of u are known. Relatively accurate values of $\partial p/\partial x$ are required for the solution of the axial momentum equation. In order to deal with this problem, equation (3.1) for rw was solved first, to obtain downstream values of rw. Then equation (3.3) was integrated radially across the flowfield, to obtain radial pressures, using downstream

values of $r\tilde{\omega}$ and upstream values of r. Then $\partial\bar{p}/\partial x$ was calculated and then corrected based upon conservation of axial momentum flux. Using the corrected source term, $\partial\bar{p}/\partial x$, equation (3.1) was then solved for $\tilde{u}$, $\tilde{f}$, k, and ε. This procedure has been used previously (10, 11, 18). It preserves the marching character of the GENMIX solution procedure for the solution of the parabolic equations. For the present calculations, this procedure was found to conserve axial momentum within 2 percent.

3.3 Separated Flow

3.3.1 Continuous Phase

The treatment of the continuous phase in the separated-flow analysis is similar to the LHF model, except that additional source terms, $S_{p\phi}$, due to interphase transport are included in the governing equations. The flows considered here are very dilute; therefore, effects of the dispersed phase on turbulence quantities are ignored for the present. In addition, since isothermal, solid, particle-laden flows are considered, the only source term involves the exchange of momentum between the continuous and the dispersed phase. Because the density of the continuous phase is constant and its volume fraction is nearly unity, a solution for $\tilde{f}$ is no longer required. Finally, in this case, Favre and Reynolds averaged quantities are identical.

Both separated-flow analyses involve dividing the dispersed phase into n groups and tracking the trajectory of each group through the

flow field. In order to obtain the momentum exchange source term, the continuous-phase flow field is divided into computational cells and the net change in momentum of each particle group as it enters and leaves a computational cell is computed. This is referred to as the "Particle Source in Cell Approach" (PSIC) described by Sharma and Crowe (59). The exact forms of the source terms are given in table 3.2. In order to preserve the marching character of the calculation, no source term is calculated for the radial direction. This can be neglected with little error since the radial momentum equation is only used to calculate the axial pressure gradient which is later corrected.

Particle source terms could also be included in table 3.2 for both k and ε, to represent the effects of the particles on turbulence properties. As discussed by Al Taweel and Landau (90), turbulence intensities of the continuous phase can be reduced as a result of the presence of particles. They concluded that the magnitude of this damping, termed turbulence modulation, increases with increasing particle loading and decreases with increasing particle diameter. There have been a number of attempts to account for the influence of the dispersed phase on turbulence properties using the k-ε turbulence model. Mostafa and Elghobashi (91) derived a two-equation turbulence model for two-phase flows that attempts to account for the additional energy dissipation due to the presence of particles. Mostafa and Mongia (92) evaluated a simplified version of this model which contained one additional constant and found that it

Table 3.2. - Particle Source Terms in the Separated Flow Analysis

ϕ	$S_{p\phi}$
1	0
$\tilde{u}$	$V_j^{-1} \sum_{i=1}^{n} \left[\dot{n}_i m_p \left(u_{pi} \right)_{in} - \left(u_{pi} \right)_{out} \right]_j$
$\widetilde{rw}$	$V_j^{-1} \sum_{i=1}^{n} \left[\dot{n}_i m_p \left(rw_{pi} \right)_{in} - \left(rw_{pi} \right)_{out} \right]_j$
k	0
ϵ	0

yielded slightly better predictions than the standard k-ε model when the constant was optimized for that particular flow considered. Shuen, et al. (40), Shuen (41), and Zhang, et al. (42) also presented a model for turbulence modulation based on the k-ε model. Comparisons with measurements were generally better than the single-phase k-ε model, however, an additional constant was also introduced which could not be easily evaluated. Since the loading ratio of particles is relatively low (0.2) in the present study, turbulence modulation was not considered in the theory.

3.3.2 Dispersed Phase

The dispersed-phase properties are obtained by solving the Lagrangian equation of motion for the particles, assuming that the particles can be approximated as spheres. The general form of the equation (the B-B-O equation that includes effects studied by Basset, Boussinesq, and Oseen), after neglecting effects of particle rotation, can be written as follows (27):

$$\frac{\pi}{6} d_p^3 \rho_p \frac{d\vec{u}_p}{dt_p} = \frac{\pi}{8} d_p^2 \rho C_D |\vec{u} - \vec{u}_p| (\vec{u} - \vec{u}_p) - \frac{\pi}{6} d_p^3 \frac{\partial p}{\partial \vec{r}}$$

$$+ \frac{\pi}{12} d_p^3 \rho \frac{d}{dt_p} (\vec{u} - \vec{u}_p) + \frac{3}{2} d_p^2 (\pi \rho \mu)^{1/2} \int_{t_{po}}^{t_p} \frac{(d/d\xi(\vec{u} - \vec{u}_p))}{(t_p - \xi)^{1/2}} d\xi + F_e \tag{3.13}$$

where the time derivative is taken following the motion of the particle

$$\frac{d}{dt_p} = \frac{\partial}{\partial t} + \vec{u}_p \frac{\partial}{\partial \vec{r}} \tag{3.14}$$

The term on the left-hand side of equation (3.13) represents the inertia of the particle sphere. Taken in order, the terms on the right-hand side of equation (3.13) represent: the drag force on the sphere, which conventionally includes both skin friction and form drag; the force on the sphere due to static pressure gradients in the flow; the force on the sphere due to the inertia of fluid displaced by its motion, which is often called the virtual mass term; the Basset term, which allows for effects of the deviation of the flow from a steady flow pattern around the sphere; and the external or body force term, e.g., the force due to gravity.

Assumptions made to calculate particle trajectories were as follows: dilute particle-laden flow with drag equivalent to a single particle in an unbounded environment; particle collisions neglected; drag treated empirically, assuming quasisteady flow for spherical particles; and since $\rho_p/\rho > 200$, effects of static pressure gradients, virtual mass, Basset forces, Magnus forces, etc., can be neglected with little error. The remaining assumptions are typical of separated-flow models of dilute particle-laden flows and are described more completely in Refs. 54 and 57.

After adopting these assumptions, equation (3.13) can be greatly simplified with the result that the position and velocity of each particle group can be found by integrating:

$$\frac{dx_{pi}}{dt} = u_{pi}, \quad i = 1,2,3 \tag{3.15}$$

$$\frac{du_{pi}}{dt} = \frac{3\rho C_D}{4 d_p \rho_p} \left(u_i - u_{pi}\right) \left|\vec{u} - \vec{u}_p\right| + a_i, \quad i = 1,2,3 \qquad (3.16)$$

The drag coefficient was calculated from a standard empirical correlation for solid spheres, recommended by Faeth (52-54), as follows:

$$C_D = \frac{24}{Re_p}\left(1 + \frac{Re_p^{2/3}}{6}\right), \quad Re_p \leq 1000$$
$$C_D = 0.44, \qquad Re_p > 1000 \qquad (3.17)$$

Equation (3.16) was integrated using a second-order algorithm similar to Shuen (41).

3.3.3 Deterministic Separated Flow

For the deterministic separated flow approach, the dispersed phase is assumed to interact only with mean properties of the continuous phase. Since mean properties are only considered for the deterministic separated flow model, all terms in equation (3.16) are considered to be time averaged and the local mean velocity is used as the ambient velocity for each particle group.

The coupled parabolic equations, (3.1), (3.3), and (3.16) were solved in an iterative fashion. Equations (3.1) and (3.3) were solved first with the particle source term from the previous step. Then equation (3.16) was solved to determine particle trajectories and to update source terms for the continuous phase. At least 1400 particle groups were tracked during these calculations in order to find statistically significant flow properties.

3.3.4 Stochastic Separated Flow

The stochastic separated flow approach involves finding the motion of a statistically significant sample of particles as they leave the injector and encounter a succession of turbulent eddies. Treatment of the continuous phase is identical to the deterministic separated flow model. Equations (3.15) and (3.16) are also solved for particle motion, however, instantaneous properties are used rather than mean continuous-phase properties. The method of specifying instantaneous eddy properties and treating particle/eddy interactions follows a proposal of Gosman and Ioannides (66), as modified by Shuen (41).

Important properties of the stochastic separated flow computation are the physical properties of each eddy and the interaction time between a particle group and particular eddy. The velocity within each eddy is assumed to be constant but eddy properties are assumed to vary randomly from one eddy to the next. Eddy velocities are found using Monte Carlo methods, after defining a probability density function (PDF) for each component of velocity. Velocity fluctuations are assumed to be isotropic, with a Gaussian PDF having a standard deviation of $(2\ k/3)^{1/2}$ and mean values $\tilde{u}$, $\tilde{v}$, and $\tilde{w}$. The cumulative distribution function (CDF) of each velocity component is constructed and randomly sampled. This involves choosing three random numbers in the range 0-1 with a random number generator and then finding the

three velocities at these values of the CDF. This procedure assures random selection of velocities in a manner that satisfies the PDF of velocity.

Particle groups are assumed to interact with a particular eddy for a time either as long as the eddy lifetime or the time required for a particle to traverse the eddy, whichever is shorter. Following Shuen (41), characteristic eddy sizes and lifetimes are specified as follows:

$$L_e = C_\mu^{3/4} \frac{k^{3/2}}{\varepsilon} \tag{3.18}$$

$$t_e = \frac{L_e}{\left(\frac{2k}{3}\right)^{1/2}} \tag{3.19}$$

Particles and eddies are assumed to interact as long as the time of interaction and the relative displacement of the particle and the eddy (from the start of the interaction) are both less than t_e and L_e. When the interaction ends by the L_e criterion, the particles have traversed the eddy. Ending the interaction by the t_e criterion implies that the eddy has captured the particle.

The remaining computations are similar to the deterministic separated flow model. The random-walk calculations for each particle group, however, required a larger number of particle groups to obtain statistically significant results: at least 7000 particle groups were employed during the present computations.

CHAPTER IV

RESULTS AND DISCUSSION

4.1 Single-Phase Jets

Single-phase jets were studied initially in order to assess the suitability of the experimental configuration, to provide baseline results for comparison with measurements for the particle-laden jets, and to assess the capability of the continuous-phase model without the complications resulting from the presence of a dispersed phase. Experimental results obtained during the present study are discussed first. Predictions are then compared with measurements obtained both during the present study, as well as other measurements in swirling jets taken from the literature. All data obtained during the present study are tabulated in Appendix C.

4.1.1 Experimental Results

Measured properties of the present single-phase jets are illustrated in figures 4.1 to 4.13. Based on the measurements illustrated in figures 4.1, 4.2, and 4.3, for $S = 0$, 0.19, and 0.33, respectively, it is clear that swirl has a large effect on streamwise properties along the flow axis. The rate of decay of the axial velocity with streamwise distance, seen in figure 4.1, increases as swirl number increases. For example, the mean centerline axial

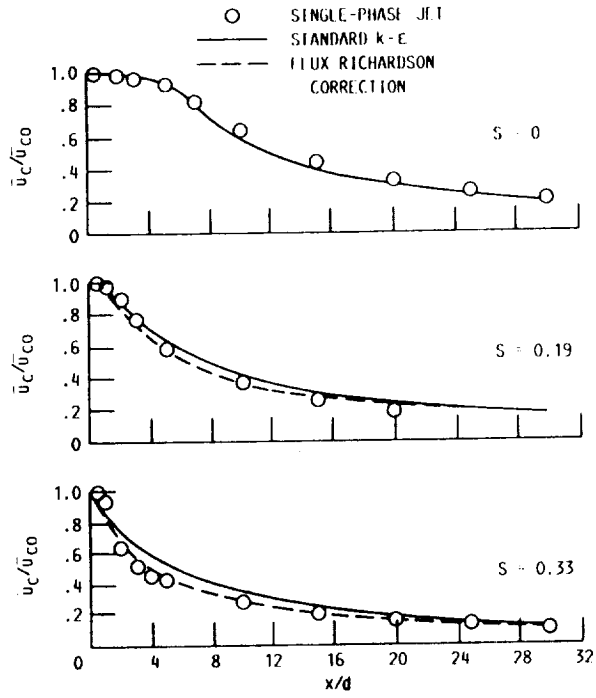

Figure 4.1. - Axial variation of centerline axial velocity with streamwise distance for the single-phase nonswirling and swirling jets (S = 0, 0.19, 0.33).

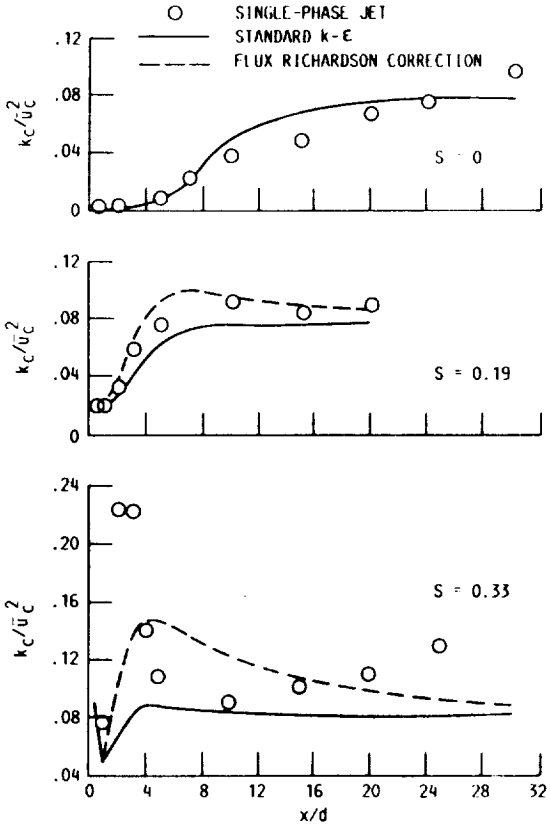

Figure 4.2. - Axial variation of centerline turbulence kinetic energy with streamwise distance for the single-phase nonswirling and swirling jets (S = 0, 0.19, and 0.33).

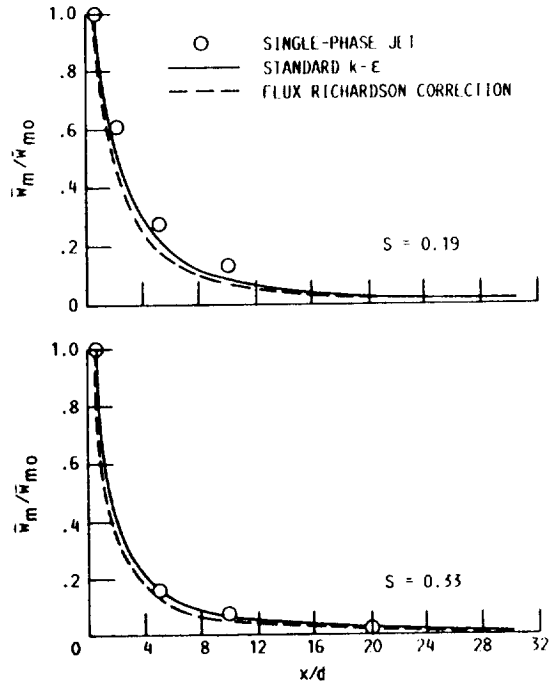

Figure 4.3. - Axial variation of maximum angular velocity with streamwise distance for the single-phase swirling jets (S = 0.19 and 0.33).

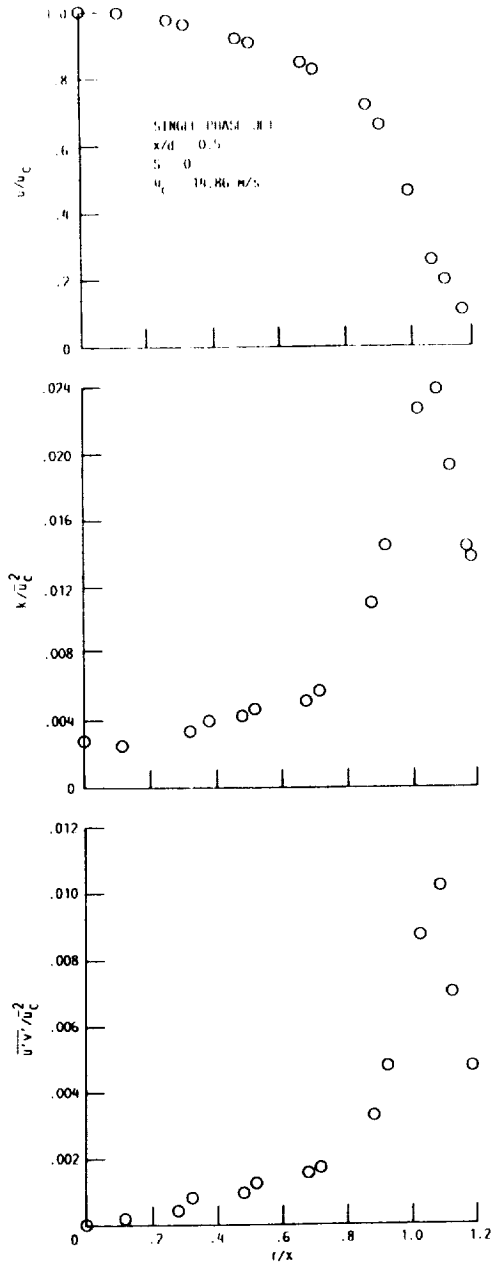

Figure 4.4. - Radial variation of flow properties at x/d = 0.5 for the single-phase nonswirling jet.

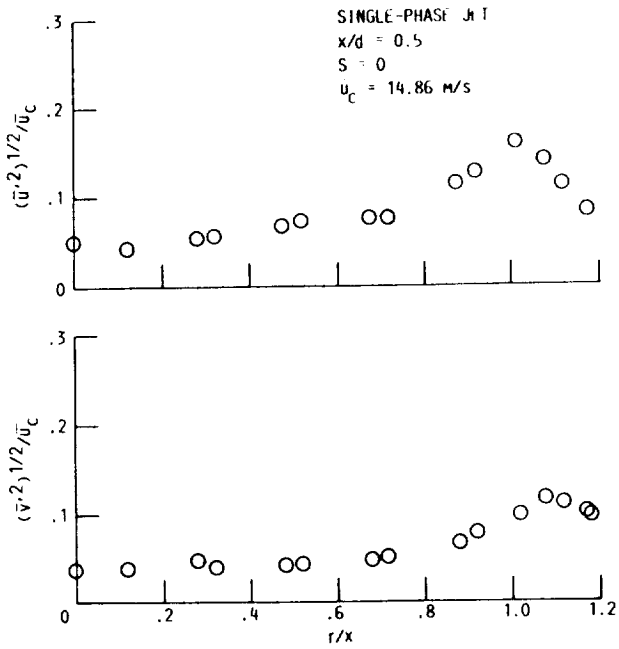

Figure 4.4. - Cont.

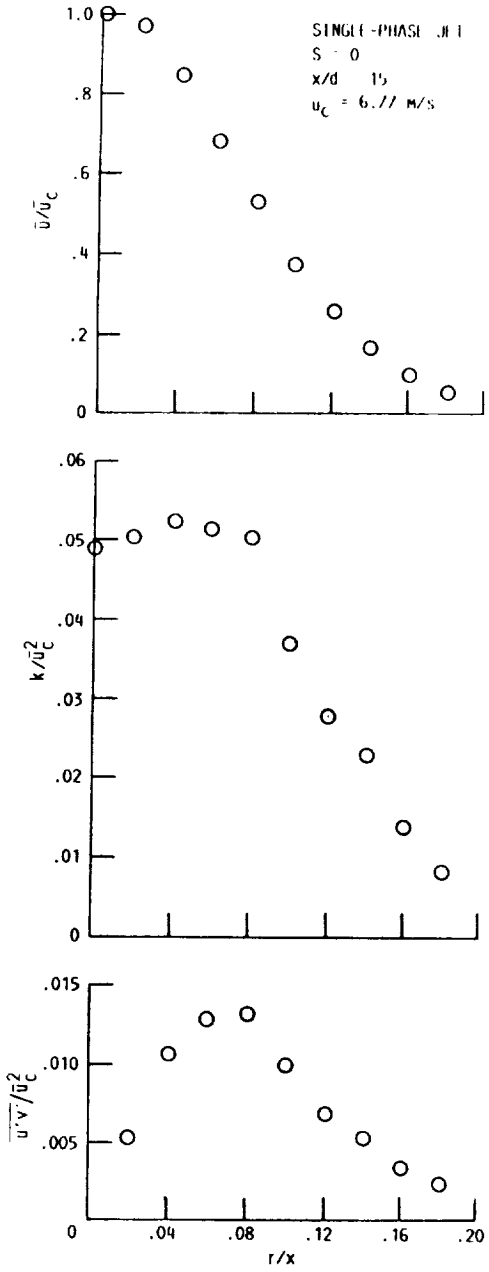

Figure 4.5. - Radial variation of flow properties at x/d = 15 for the single-phase nonswirling jet.

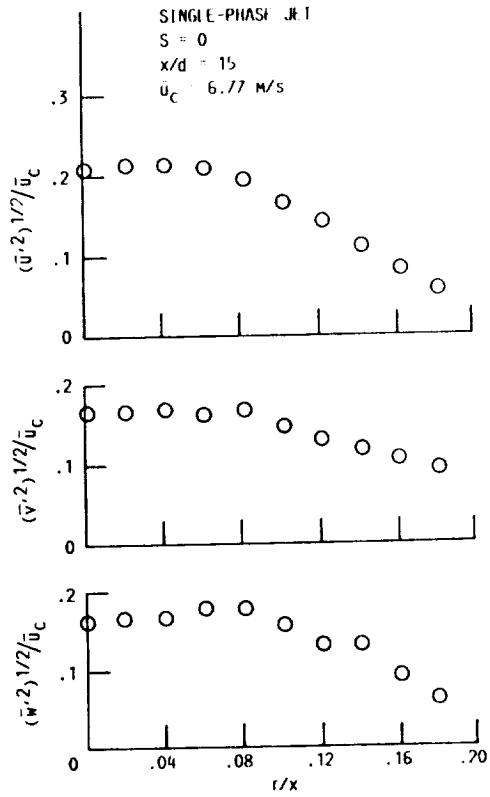

Figure 4.5. - Cont.

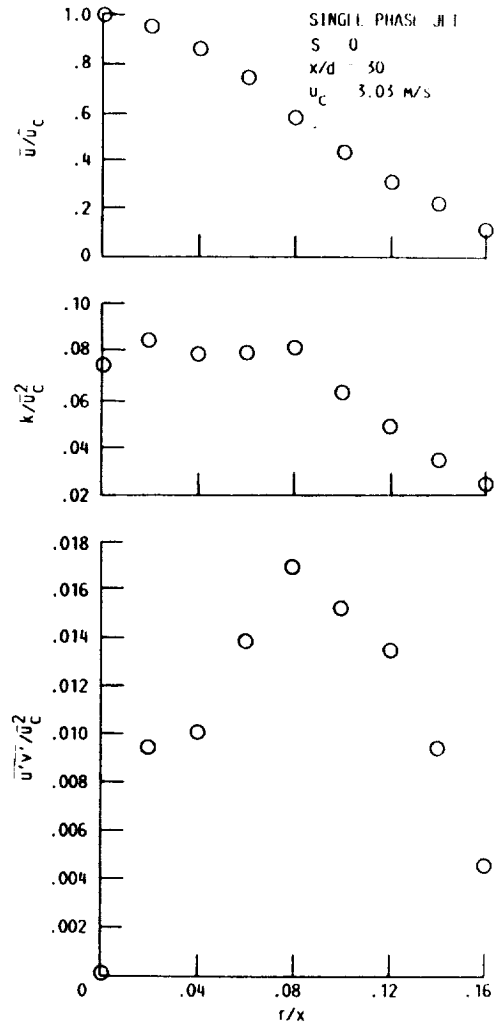

Figure 4.6. - Radial variation of flow properties at x/d = 30 for the single-phase nonswirling jet.

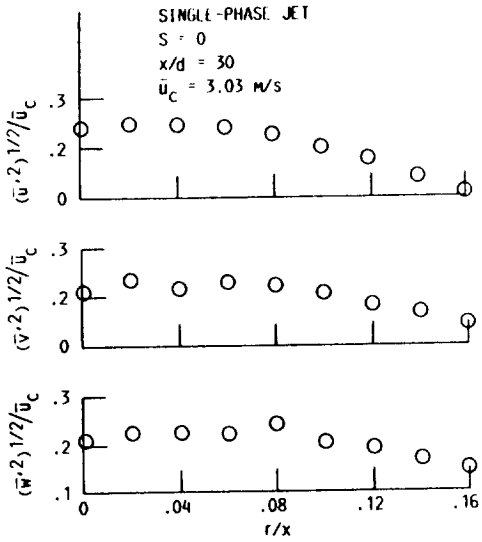

Figure 4.6. - Cont.

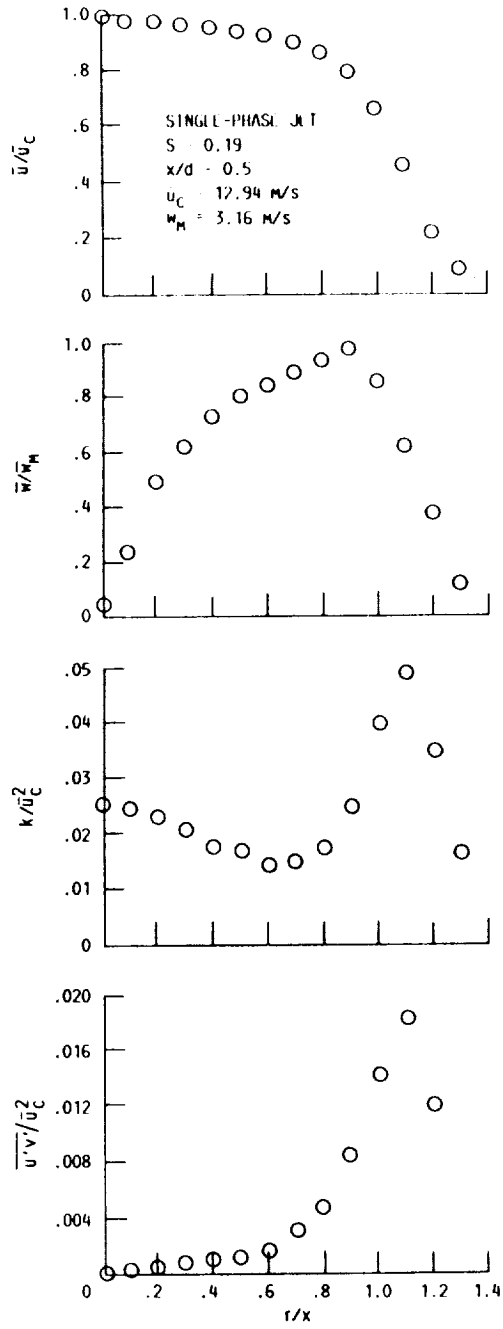

Figure 4.7. - Radial variation of flow properties at x/d = 0.5 for the single-phase swirling jet (S = 0.19).

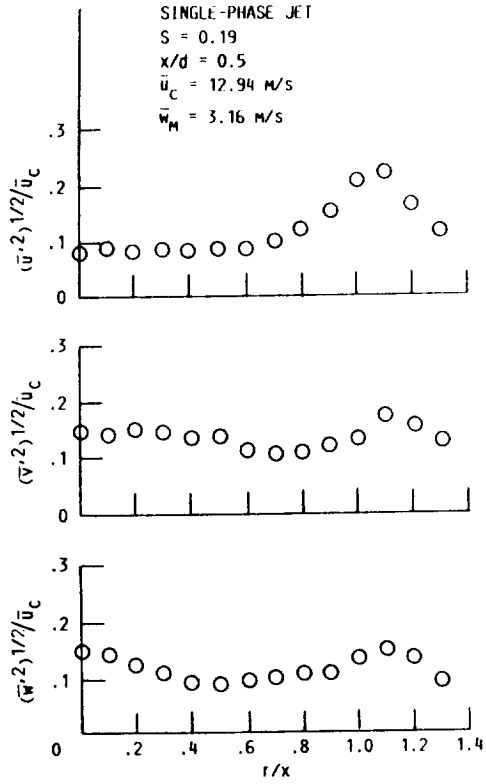

Figure 4.7. - Cont.

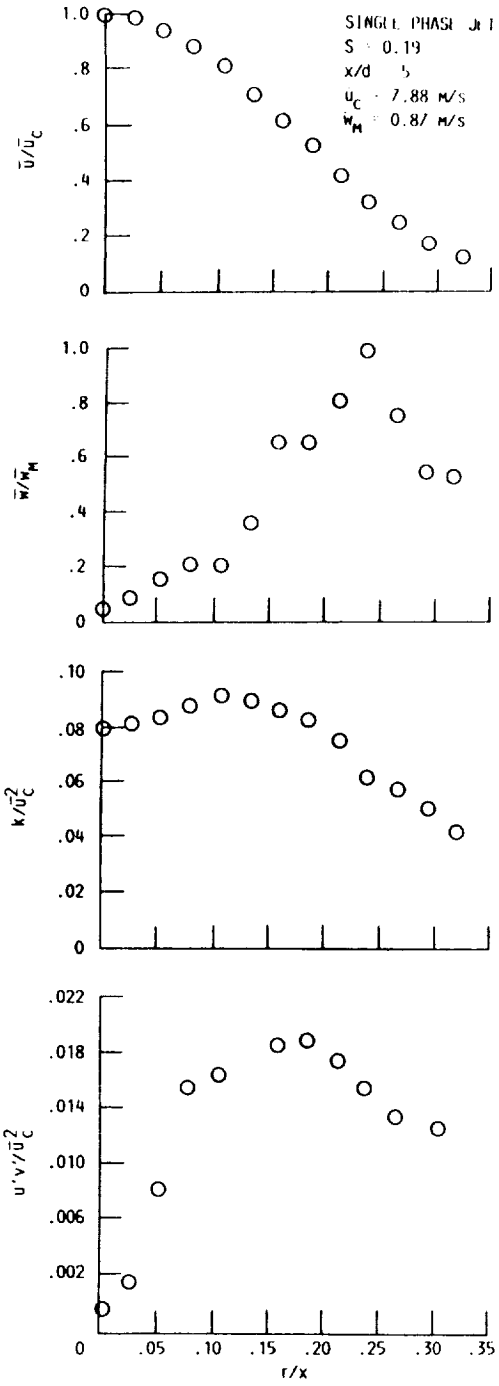

Figure 4.8. - Radial variation of flow properties at x/d = 5 for the single-phase swirling jet (S = 0.19).

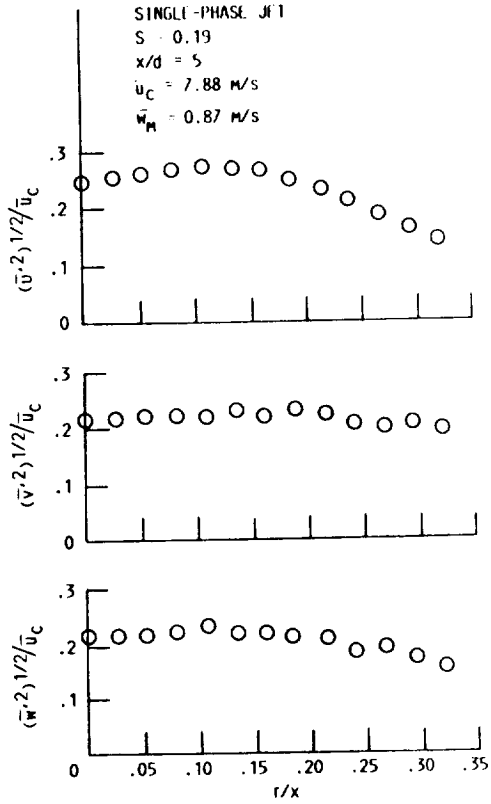

Figure 4.8. - Cont.

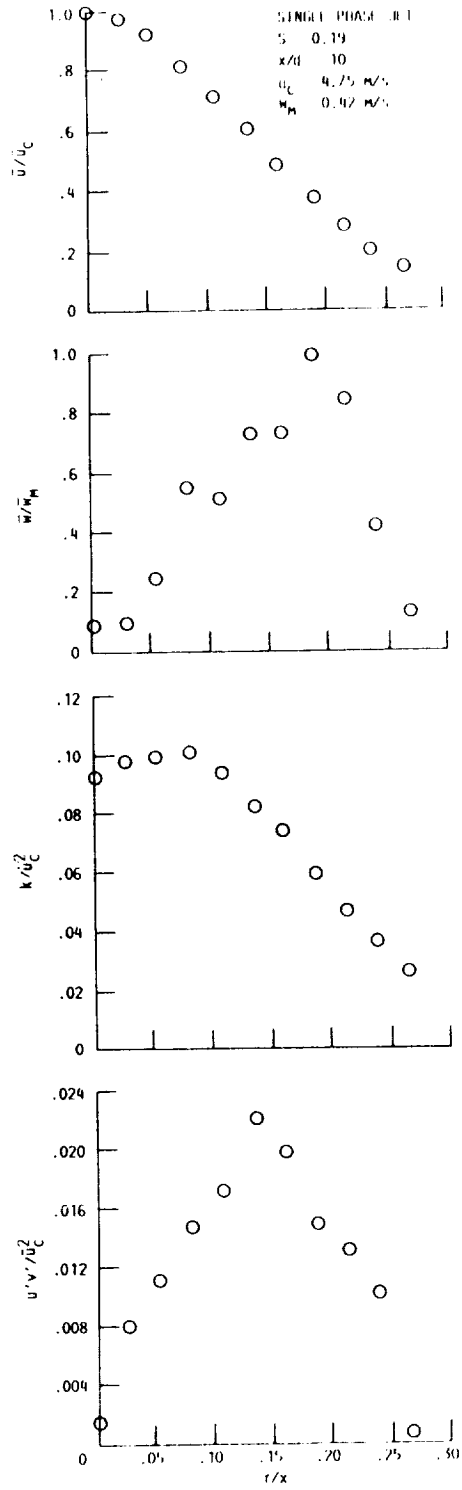

Figure 4.9. - Radial variation of flow properties at x/d = 10 for the single-phase swirling jet (S = 0.19).

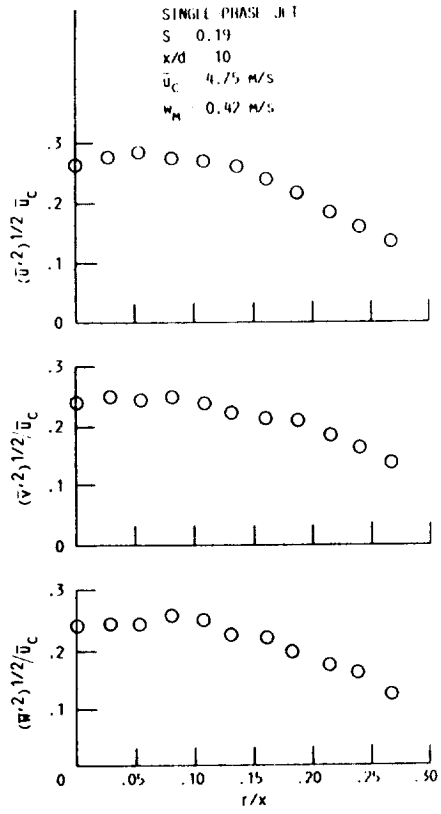

Figure 4.9. - Cont.

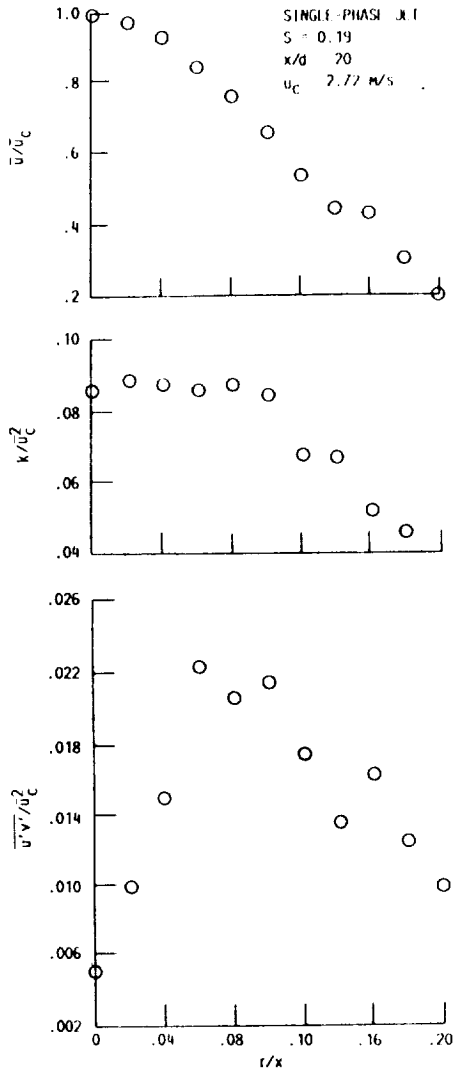

Figure 4.10. - Radial variation of flow properties at x/d = 20 for the single-phase swirling jet (S = 0.19).

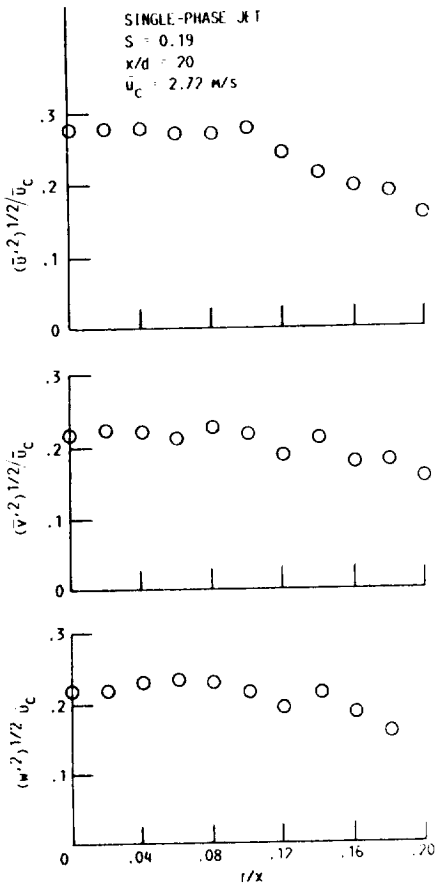

Figure 4.10. - Cont.

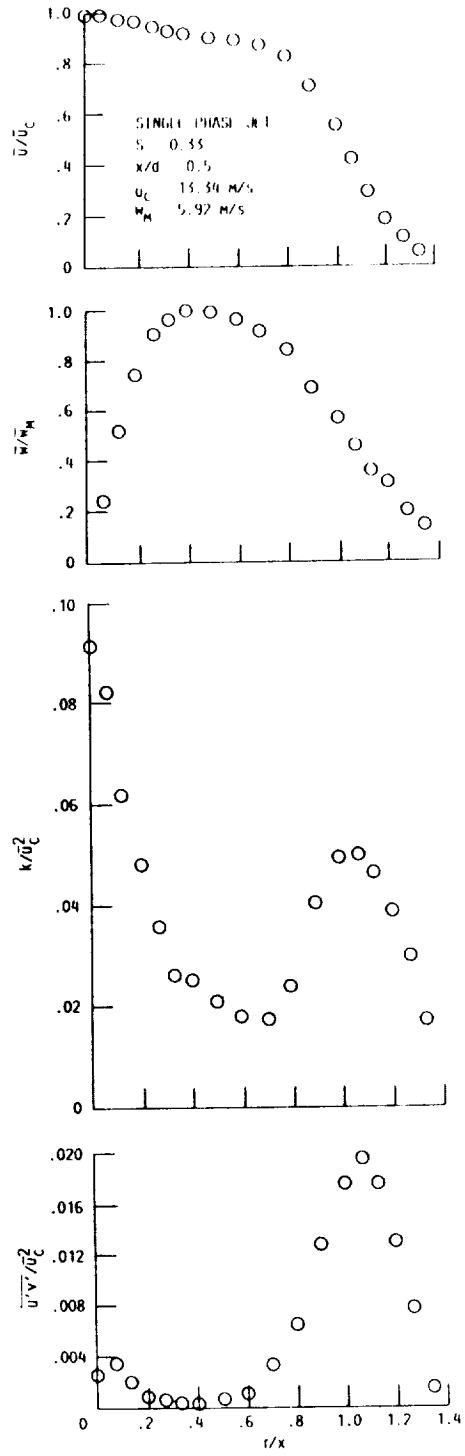

Figure 4.11. - Radial variation of flow properties at x/d = 0.5 for the single-phase swirling jet (S = 0.33).

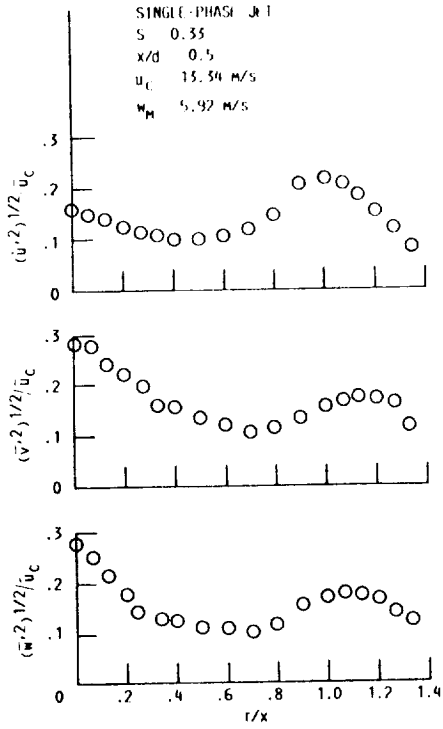

Figure 4.11. - Cont.

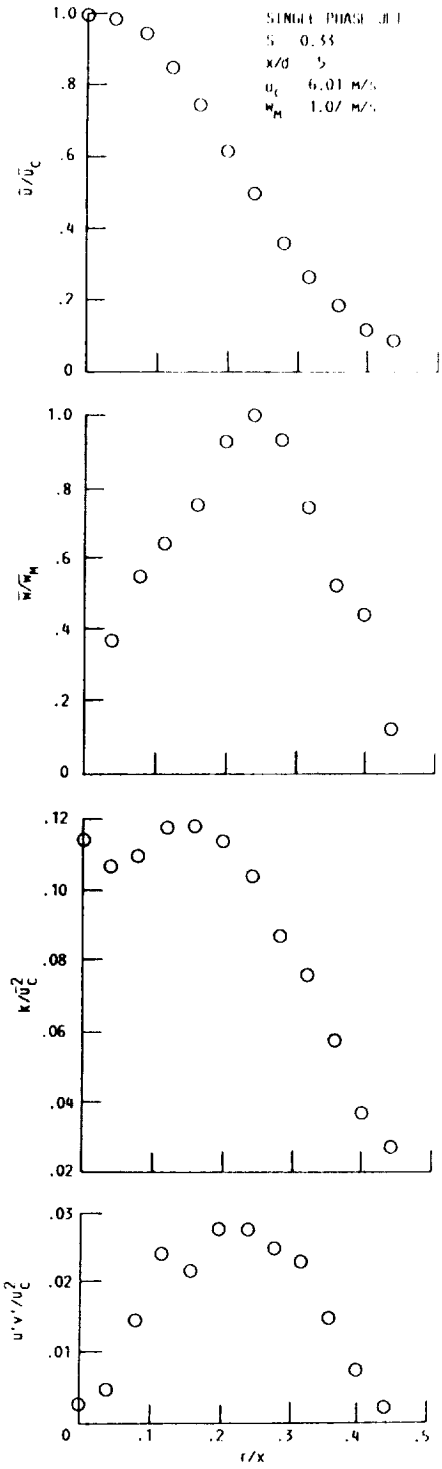

Figure 4.12. - Radial variation of flow properties at x/d = 5 for the single-phase swirling jet (S = 0.33).

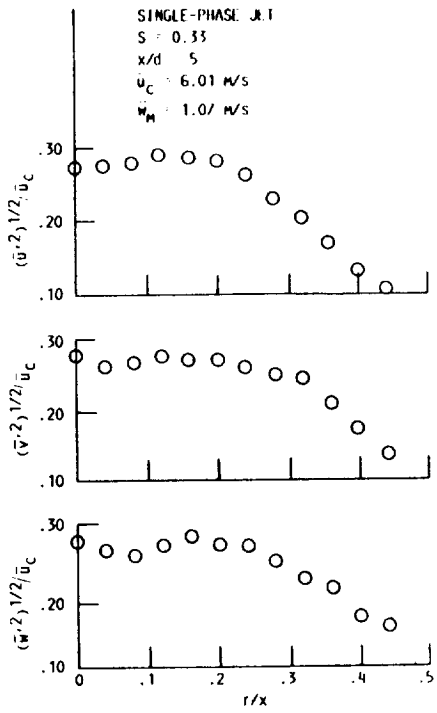

Figure 4.12. - Cont.

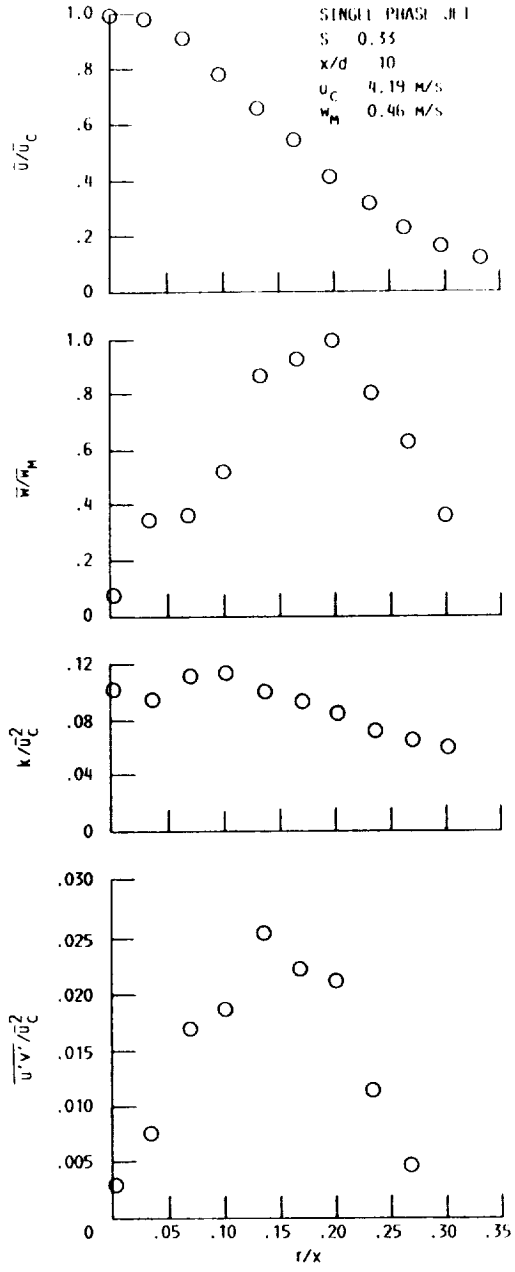

Figure 4.13. - Radial variation of flow properties at x/d = 10 for the single-phase swirling jet (S = 0.33).

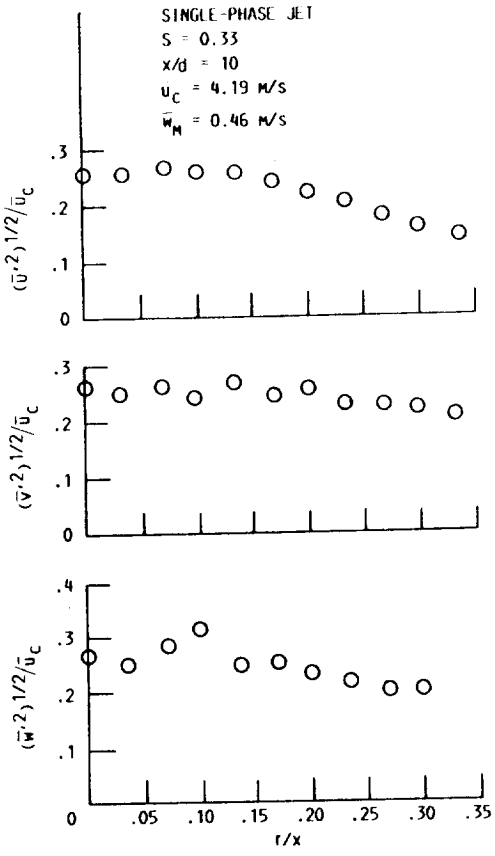

Figure 4.13. - Cont.

velocity decays to one-half its original value (measured at $x/d = 0.5$) in approximately 3.5 injector diameters for $S = 0.33$, while approximately 13 injector diameters are required for the jet without swirl. Turbulence kinetic energy near the injector exit increases dramatically with increasing swirl (see figure 4.2). At $x/d = 0.5$, normalized k_c is approximately 25 times higher for $S = 0.33$ than for the nonswirling jet. For the swirling jets, the development of k_c with streamwise distance is strongly influenced by the swirl number. For $S = 0.19$, shown in figure 4.2, normalized k_c begins to increase near the injector exit and rises monotonically to an asymptotic value on the order of 0.10. For $S = 0.33$, also shown in figure 4.2, normalized k_c increases even more sharply near the injector exit, reaching a peak of approximately 0.22 at $x/d = 2$, and then decays to approximately the same asymptotic value as $S = 0.19$. Angular velocity, see figure 4.3, decays quite rapidly with streamwise distance. For $S = 0.33$, angular velocity has decayed to one-half its original value (at $x/d = 0.5$) at approximately $x/d = 2$. Increasing swirl increases the rate of angular velocity decay.

Radial profiles of measured properties in the single-phase jets are illustrated in figures 4.4 to 4.6 for $S = 0$, figures 4.7 to 4.10 for $S = 0.19$, and figures 4.11 to 4.13 for $S = 0.33$. At $x/d = 0.5$, peak values of k are increased by a factor of two for $S = 0.33$, when compared with the no-swirl case as shown in figures 4.4 and 4.11. Similar results are observed for Reynolds stress. The results

illustrated in figures 4.4, 4.7, and 4.11 also indicate that, at x/d = 0.5, measured values of velocity fluctuations increase as the swirl number is increased, as expected. Even at x/d = 0.5, increasing the swirl number increased the jet width; this can be seen by comparing figure 4.4 for S = 0, and figure 4.11 for S = 0.33.

Radial profiles of measured properties for the swirling jets at x/d = 5 are illustrated in figures 4.8 and 4.12. As expected, the jet width for the higher swirl number jet (S = 0.33) is larger than the S = 0.19 jet. Measured values of fluctuating quantities also increase with increasing swirl number. For S = 0.33, shown in figure 4.12, measured values of all components of the velocity fluctuations are approximately equal at x/d = 5. For S = 0.19, however, the streamwise velocity fluctuations are slightly higher than the other two components at this axial location.

Radial profiles of measured properties for the single-phase jets with swirl at x/d = 10 appear in figures 4.9 and 4.13 for S = 0.19 and S = 0.33, respectively. Angular velocities have decayed to approximately 0.4 m/s for both swirling jets at this location, and as a result, the structure of both jets is similar. However, the jet width is still wider for the higher swirl number jet than for the lower swirl number jet.

Radial profiles of measured properties for the S = 0.19 swirling jet at x/d = 20 are illustrated in figure 4.10. The mean angular velocity has decayed to a negligible value and measured values are

similar to a jet without swirl at this location. For comparison, radial profiles of the nonswirling jet at $x/d = 15$ and 30 appear in figures 4.5 and 4.6, respectively.

4.1.2 Single-Phase Jet Predictions

In order to initiate evaluation of predictions, calculations were completed for comparison with representative measurements for weakly swirling single-phase free jets, taken from the literature. Only measurements where initial conditions were known reasonably well were considered. Swirl numbers for these flows ranged from 0.25 to 0.5.

Initial conditions for the predictions are taken at the measurement location nearest to the injector exit. Starting values of ε were determined from the definition of a turbulent length scale, as follows:

$$\varepsilon_o = C_\mu \frac{k^{3/2}}{L} \tag{4.1}$$

where L was chosen as a fraction of the initial jet half-width to provide reasonably good agreement with initial streamwise changes of k. The value used for L was on the order of 0.3 of the initial half-width of the flow.

Results using the measurements reported by Morse (11) are illustrated in figures 4.14 to 4.17. Morse (11) obtained measurements using a single hot-wire probe for two weakly swirling free jets having swirl numbers of 0.25 and 0.35. Initial flow properties were measured at $x/d = 0.5$. Predictions using the standard $k - \varepsilon$ turbulence

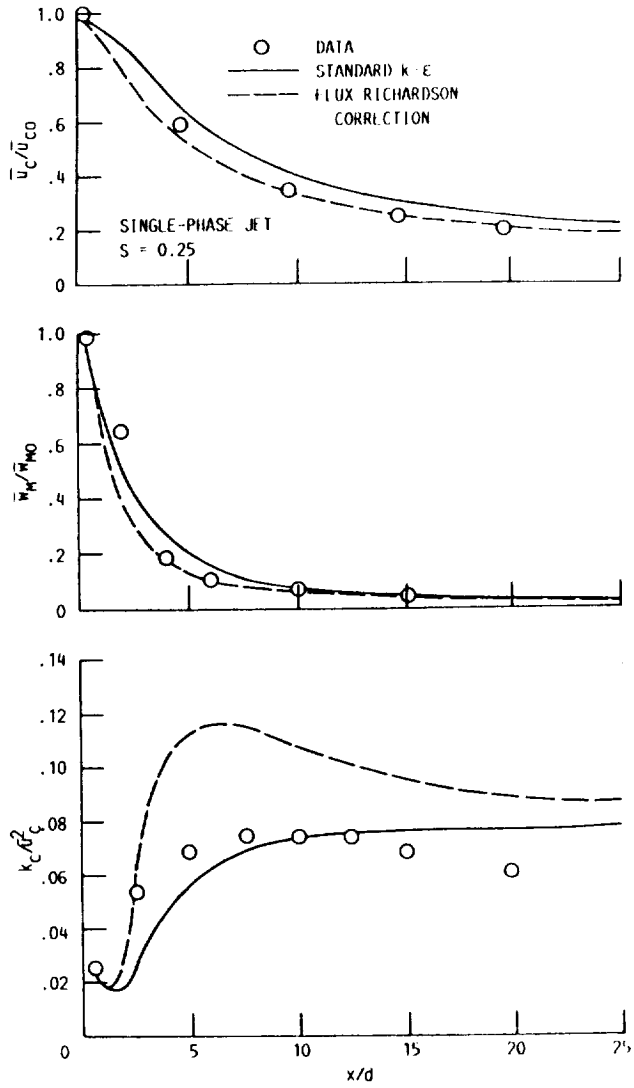

Figure 4.14. - Predicted and measured variation of flow properties in the streamwise direction for the single-phase swirling jet (S = 0.25). Data from Morse (11).

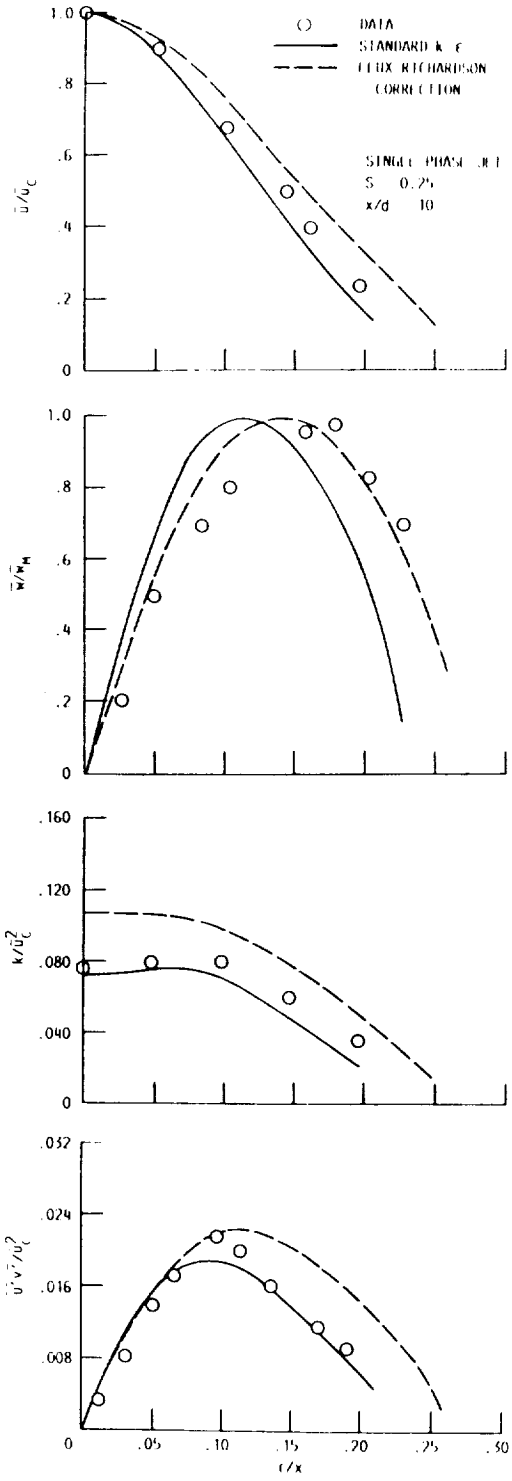

Figure 4.15. - Predicted and measured radial variation of flow properties at x/d = 10 for the single-phase swirling jet jet (S = 0.25). Data from Morse (11).

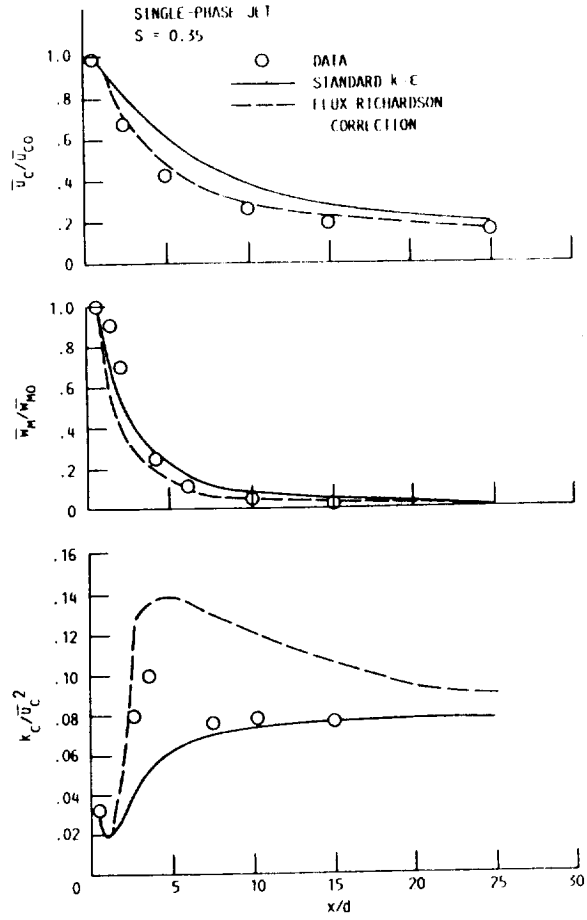

Figure 4.16. - Predicted and measured variation of flow properties in the streamwise direction for the single-phase swirling jet (S = 0.35). Data from Morse (11).

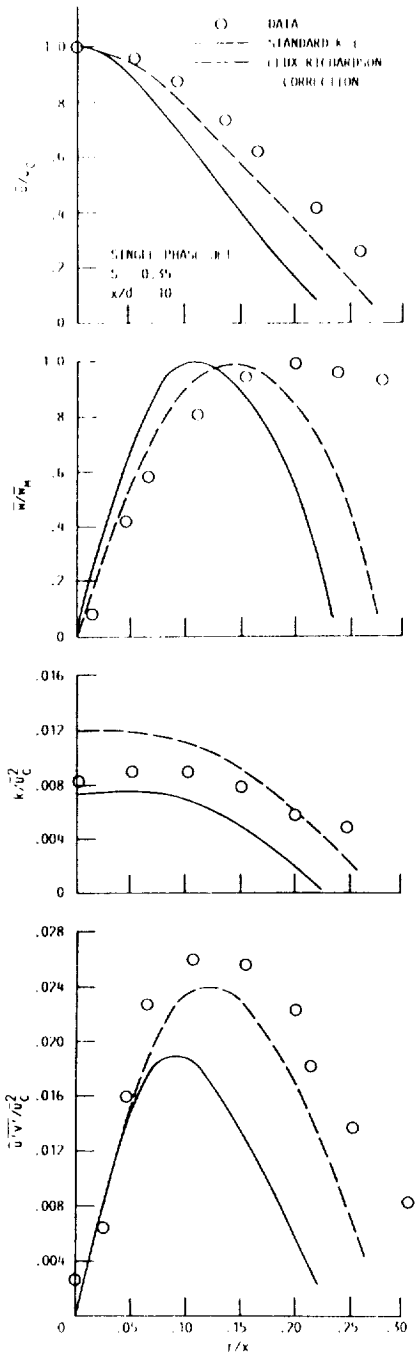

Figure 4.17. - Predicted and measured radial variation of flow properties at x/d = 10 for the single-phase swirling jet (S = 0.35). Data from Morse (11).

model and the modification for streamline curvature based on the flux Richardson number (equation (3.12)) are shown on the figures.

The streamwise variation of flow properties for $S = 0.25$ is illustrated in figure 4.14. For these results, the approach using a curvature correction gave better agreement with the measurements than the standard $k - \varepsilon$ turbulence model, however, the differences between the two are not very large. The curvature modification, however, caused predicted values of k along the axis to be significantly overestimated. Measurements of k_c reported by Morse (11), however, are somewhat lower than values obtained during the present study, which may be a factor in this apparent deficiency of the curvature correction approach. Radial profiles at $x/d = 10$ for measurements with $S = 0.25$ reported by Morse (11), are shown in figure 4.15. Again, the predictions are reasonably good. The standard $k - \varepsilon$ turbulence model somewhat underestimates the jet width at $x/d = 10$ based on the streamwise mean velocities while use of the flux Richardson correction causes the width of the jet to be slightly overestimated. The comparison between predicted and measured values of k and the Reynolds stress, illustrated in figure 4.15, is similar to the mean streamwise velocity.

Measurements and predictions for a jet having $S = 0.35$, reported by Morse (11), are illustrated in figures 4.16 and 4.17. For the higher swirl number flow, predictions using the curvature correction are in better agreement with measurements of the decay of mean axial

C-2

and maximum angular velocity. The development of k with streamwise distance is again overestimated using the curvature correction, however, measured values of k reported by Morse (11) were somewhat lower than those obtained during the present study. Normalized values for the decay of mean centerline axial and maximum angular velocity reported by Morse (11) show good agreement with those obtained during the present study. Radial profiles for the $S = 0.35$ jet measurements reported by Morse (11) at $x/d = 10$ are shown in figure 4.17. Again, predictions using the curvature correction show better agreement with measurements than the standard $k - \varepsilon$ model, although the jet width at $x/d = 10$ is slightly underestimated, even with the curvature correction. Morse (11) states, however, that edge values of angular velocity are not reliable and should be used with caution. The agreement between the radial profiles at $x/d = 10$ reported by Morse (11), shown in figure 4.17, and measurements obtained in the present study for similar conditions, figure 4.13, is reasonably good.

Measurements at a higher swirl number, $S = 0.5$, are reported by Sislian and Cusworth (5). These measurements were obtained using a single-channel LV system. Initial conditions were measured very close to the injector exit, at $x/d = 0.125$. Measurements were only made near the jet exit, ending at $x/d = 5$. The variation of streamwise flow properties is shown in figure 4.18 for this flow, Mean centerline axial and maximum angular velocities are predicted reasonably well for $x/d > 3$, using the curvature correction.

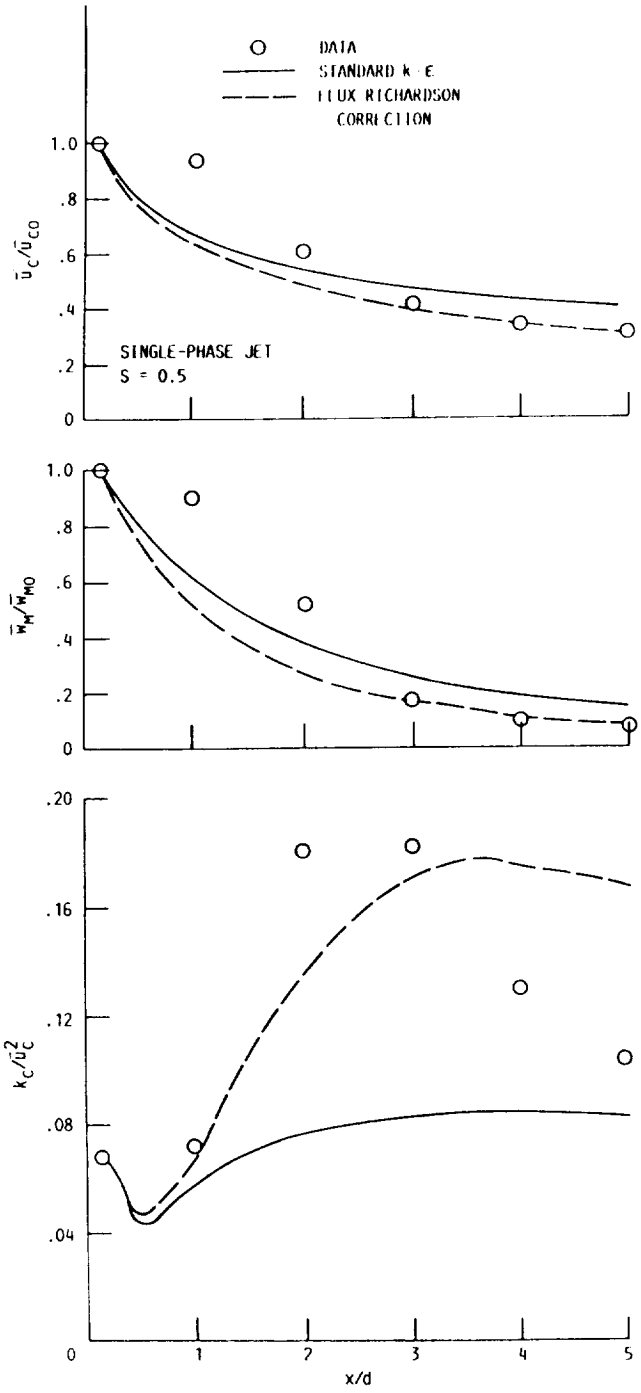

Figure 4.18. - Predicted and measured variation of flow properties in the streamwise direction for the single-phase swirling jet (S = 0.5). Data from Sislian and Cusworth (5).

Predicted rates of decay are overestimated, however, very close to the injector exit. Since the swirl number is relatively high for this flow, it may not be well represented by parabolic governing equations.

Measurements and predictions of radial flow profiles at $x/d = 4$ are shown in figure 4.19, for the measurements of Sislian and Cusworth (5). The agreement between the predictions and measurements is quite good for the approach using the curvature correction. No radial profiles at streamwise distances greater than $x/d = 4$ were reported.

Comparisons between the measurements and predictions obtained during the present study are illustrated in figures 4.20 to 4.22 for the single-phase jets without swirl. The predictions generally are in reasonably good agreement with the measurements for the nonswirling jets. For example, predictions of the rate of decay of mean centerline axial velocities with streamwise distance and radial profiles of axial velocity, both show good agreement with measurements. However, at $x/d = 15$, illustrated in figure 4.21, predictions of k and Reynolds stresses are slightly higher than measurements, particularly near the flow axis. In contrast, the jet width at this position is predicted quite well. Farther downstream, predictions of k and Reynolds stress are in better agreement with measurements, see the findings at $x/d = 30$, illustrated in figure 4.22.

Predictions and measurements are illustrated in figures 4.23 to 4.26 for the $S = 0.19$ weakly swirling jet of the present study. As shown in figure 4.23 for flow properties along the axis, the approach

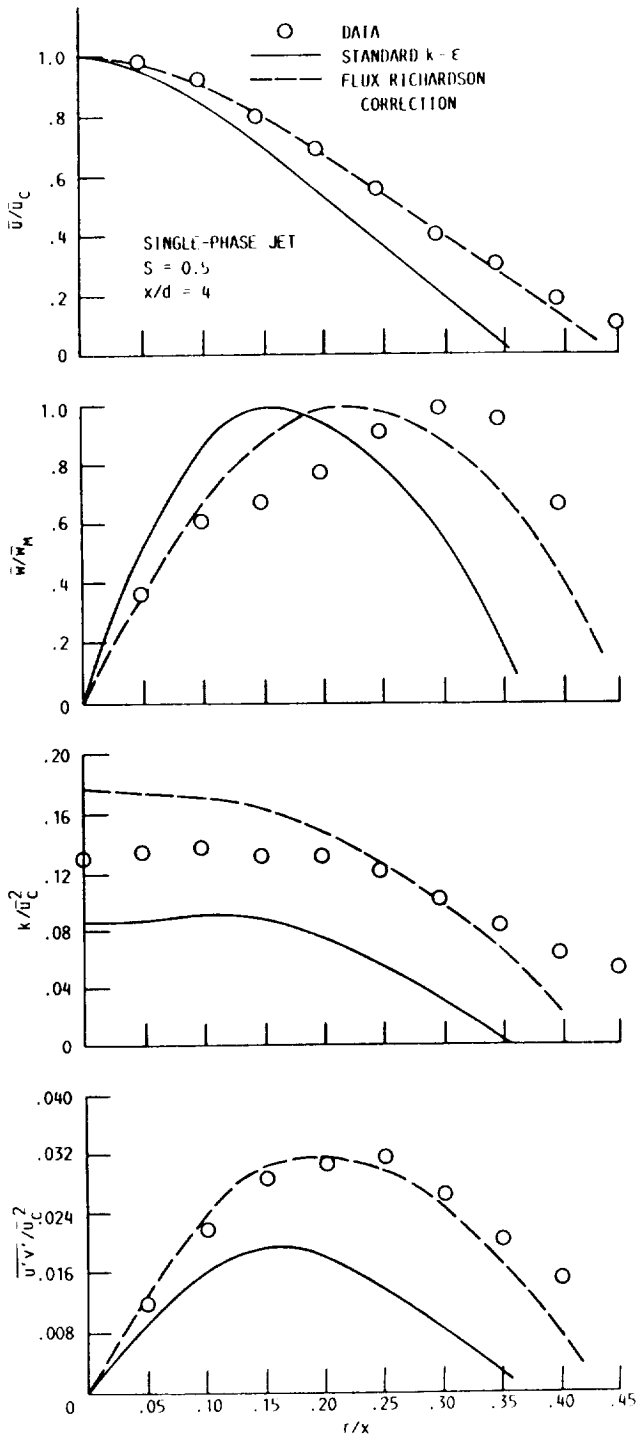

Figure 4.19. - Predicted and measured radial variation of flow properties at x/d = 4 for the single-phase swirling jet (S = 0.5). Data from Sislian and Cusworth (5).

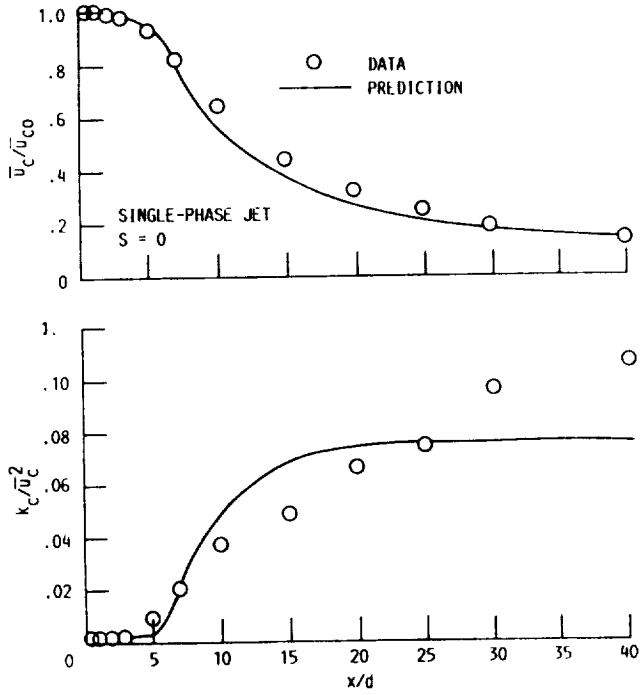

Figure 4.20. - Predicted and measured variation of flow properties in the streamwise direction for the single-phase nonswirling jet.

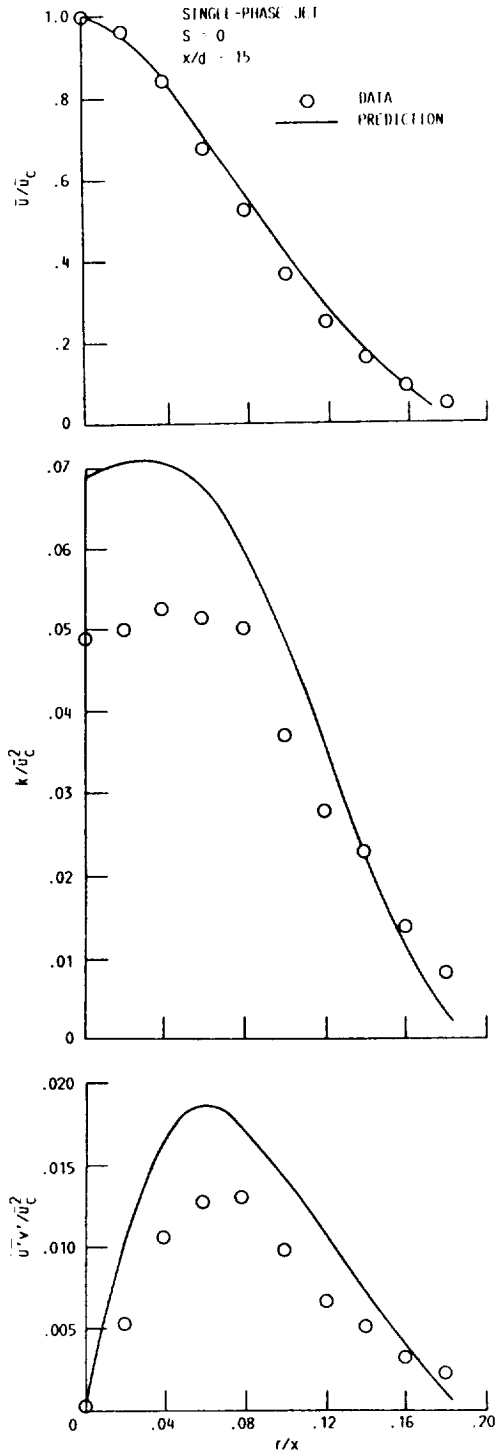

Figure 4.21. - Predicted and measured radial variation of flow properties at x/d = 15 for the single-phase nonswirling jet.

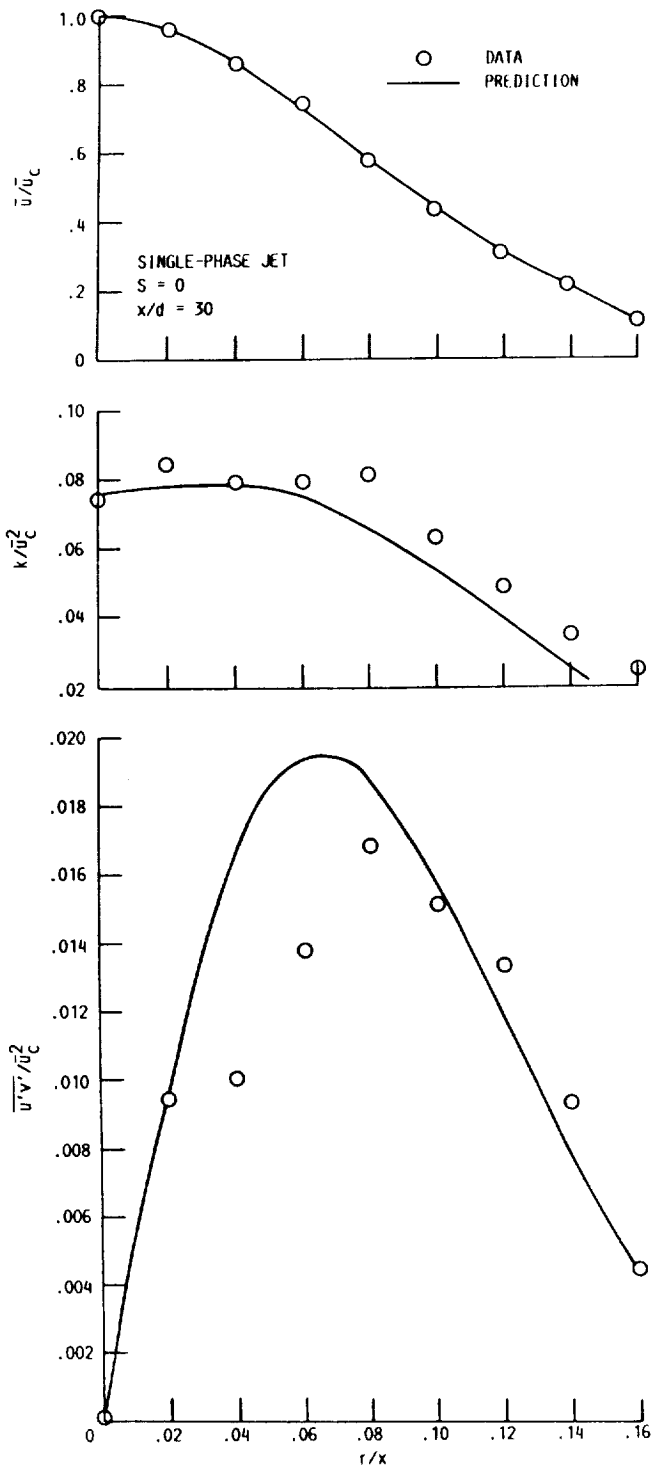

Figure 4.22. - Predicted and measured radial variation of flow properties at x/d = 30 for the single-phase nonswirling jet.

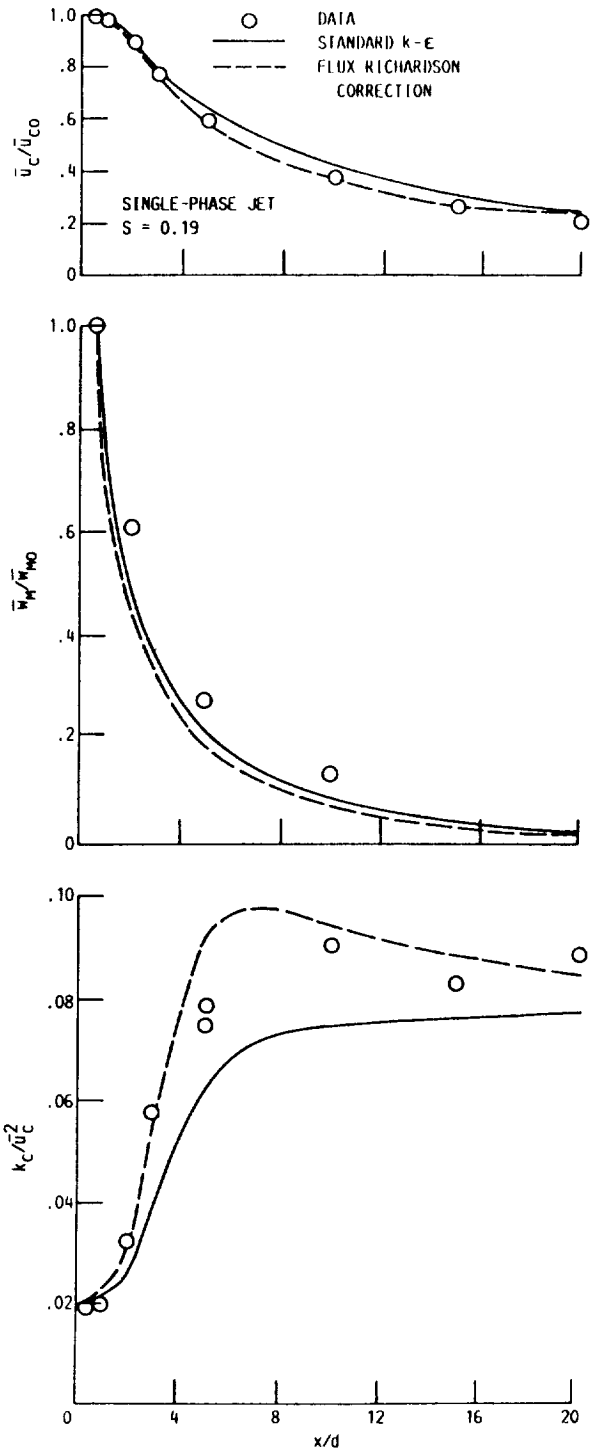

Figure 4.23. - Predicted and measured radial variation of flow properties in the streamwise direction for the single-phase swirling jet (S = 0.19).

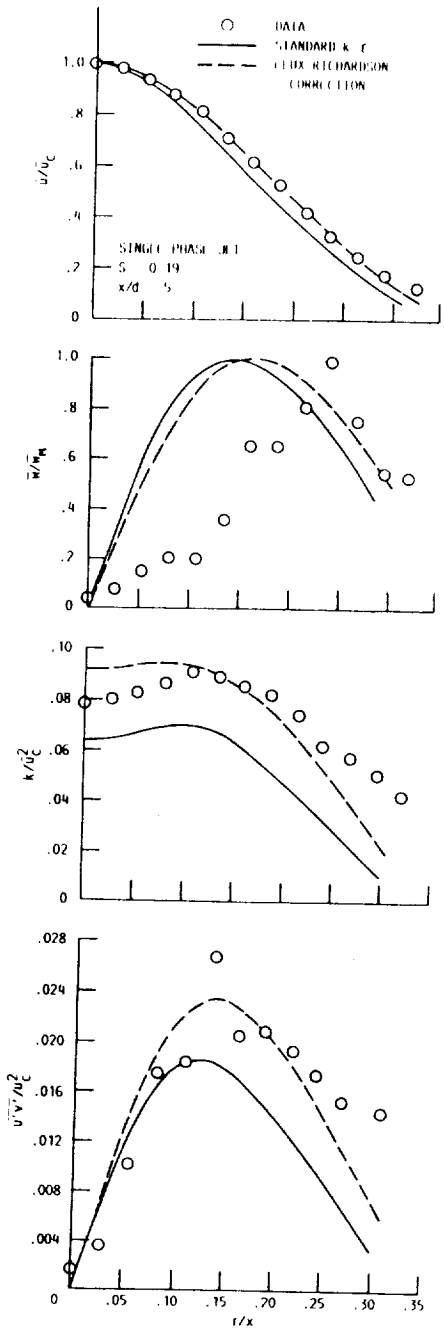

Figure 4.24. - Predicted and measured radial variation of flow properties at x/d = 5 for the single-phase swirling jet (S = 0.19).

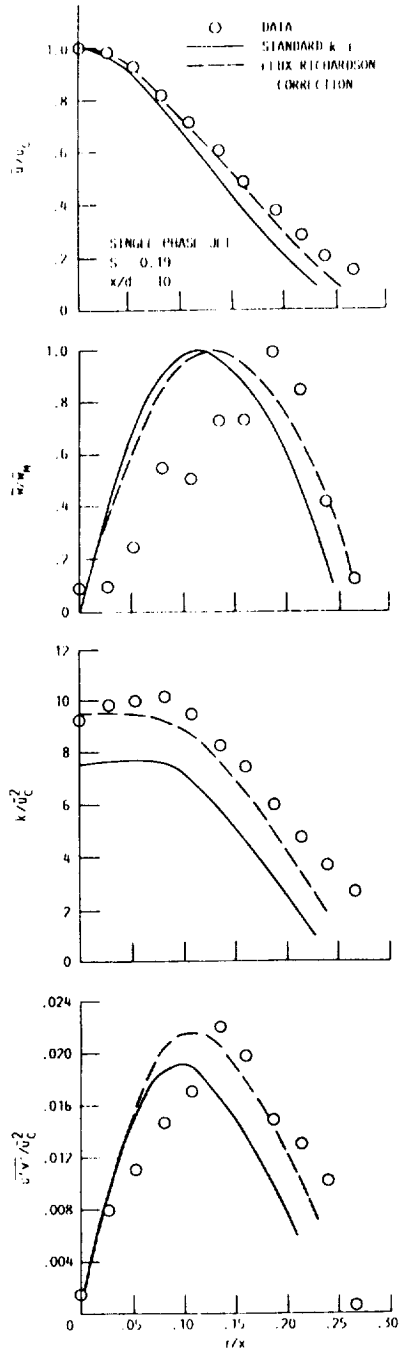

Figure 4.25. - Predicted and measured radial variation of flow properties at x/d = 10 for the single-phase swirling jet (S = 0.19).

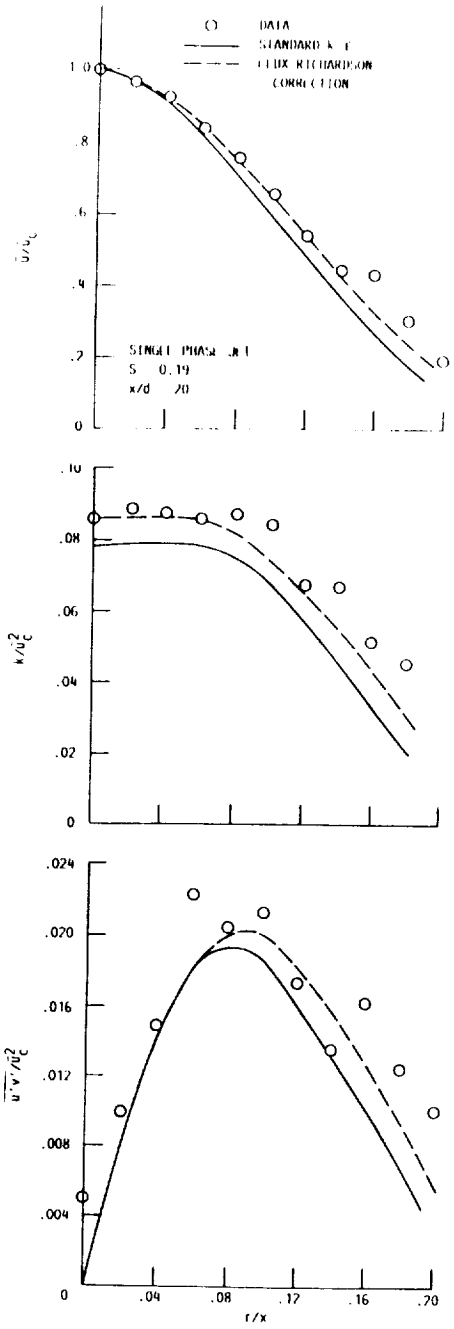

Figure 4.25. - Predicted and measured radial variation of flow properties at x/d = 20 for the single-phase swirling jet (S = 0.19).

using the streamline curvature correction based on the flux Richardson number gave better results than the standard $k - \varepsilon$ turbulence model. Predictions and measurements of radial flow properties at $x/d = 5$, 10, and 20 are shown in figures 4.24, 4.25, and 4.26, respectively. Again, predictions using the curvature correction are in better agreement with measurements than the standard $k - \varepsilon$ turbulence model. The curvature modification always increases levels of k across the entire width of the jet. This increases both the jet width and rate of decay of mean velocity components with streamwise distance. As expected, as the angular velocity decreases, differences between predictions for turbulence models with and without the curvature modification are decreased as well.

Results are not shown for the curvature modification based on the gradient Richardson number (equation (3.10)). This modification produces a turbulence damping effect over regions of the jet where $\partial r\tilde{w}/\partial r$ is positive. Levels of k are only increased in the edge regions of the jet where $\partial r\tilde{w}/\partial r$ is negative. This is clearly not correct for the swirling free jets considered during the present study. In contrast, the curvature modification based on the flux Richardson number tends to increase turbulence levels regardless of the sign of $\partial r\tilde{w}/\partial r$.

Comparisons between measurements and predictions for $S = 0.33$, from the present study, are illustrated in figures 4.27 to 4.29. Flow properties along the axis are illustrated in figure 4.27 and demonstrate that predictions are reasonably good, especially when

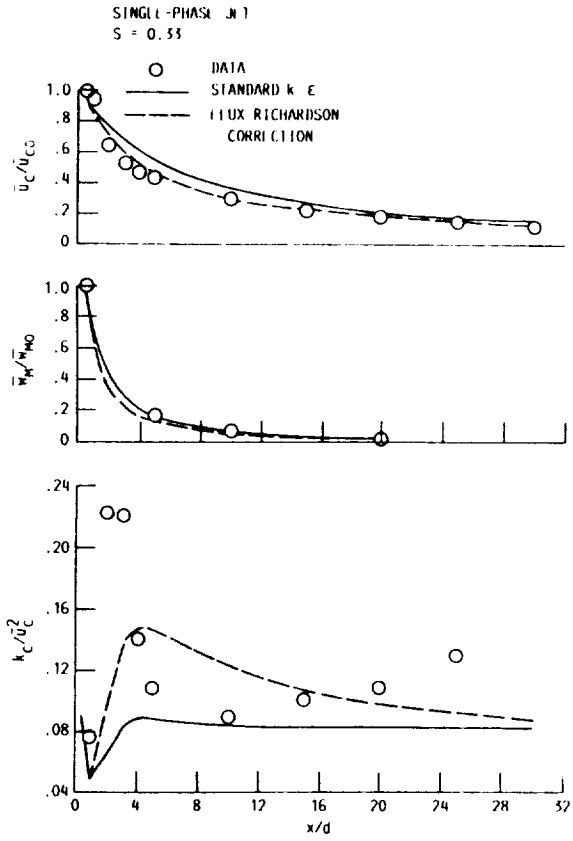

Figure 4.27. - Predicted and measured variation of flow properties in the streamwise direction for the single-phase swirling jet (S = 0.33).

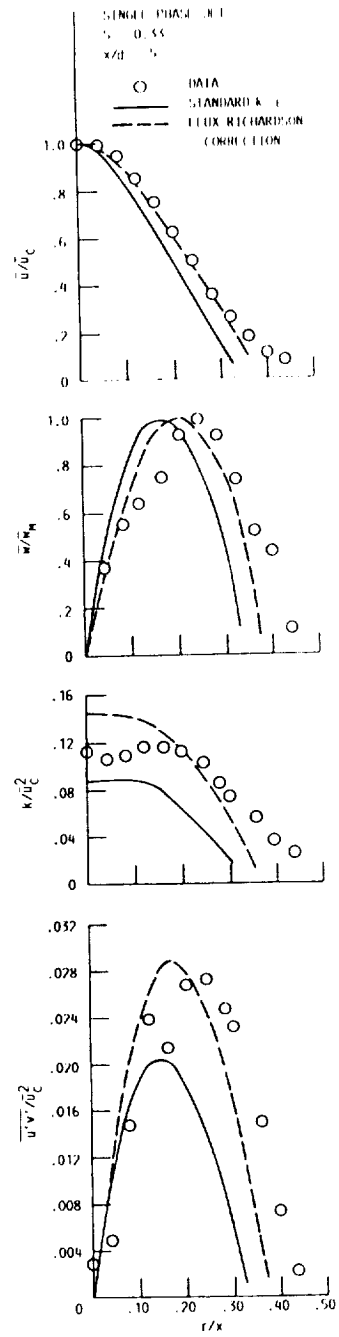

Figure 4.28. - Predicted and measured radial variation of flow properties at x/d = 5 for the single-phase swirling jet (S = 0.33).

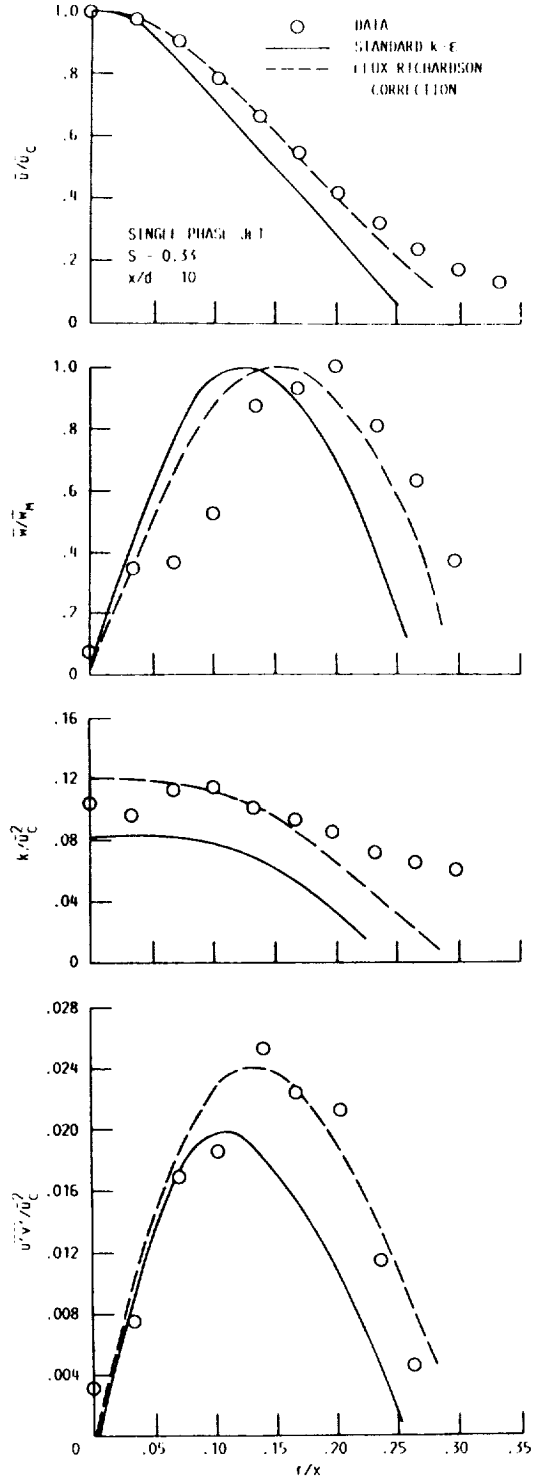

Figure 4.29. - Predicted and measured radial variation of flow properties at x/d = 10 for the single-phase swirling jet (S = 0.33).

using the curvature correction. The sharp increase in k at $x/d = 2$ is not predicted very well, however, even with the streamline curvature modification. The variation of mean centerline axial and maximum angular velocity with streamwise distance is well predicted. Predicted and measured radial variations of flow properties for the $S = 0.33$ jet of the present study at $x/d = 5$ and 10 are shown in figures 4.28 and 4.29, respectively. Again, the curvature modification shows better agreement with measurements than the standard $k - \varepsilon$ turbulence model. Predictions are reasonably good at both axial locations.

The predicted static pressure variation with streamwise distance for the $S = 0.19$ and 0.33 swirling single-phase jets is illustrated in figure 4.30. Static pressures along the centerline are slightly below atmospheric pressure. For the higher swirl number, $S = 0.33$, the maximum pressure difference is 70 Pa. The static pressure along the axis rapidly approaches atmospheric pressure since angular velocity decays rapidly. Predictions illustrated in figure 4.30 were obtained with the flux Richardson number modification to the $k - \varepsilon$ turbulence model. Predicted static pressures using the standard $k - \varepsilon$ model were similar.

Based upon the single-phase results, the flow structure of the single-phase weakly swirling jets appears to be reasonably well predicted with turbulence models that were considered during this study. The modification of the dissipation equation to account for

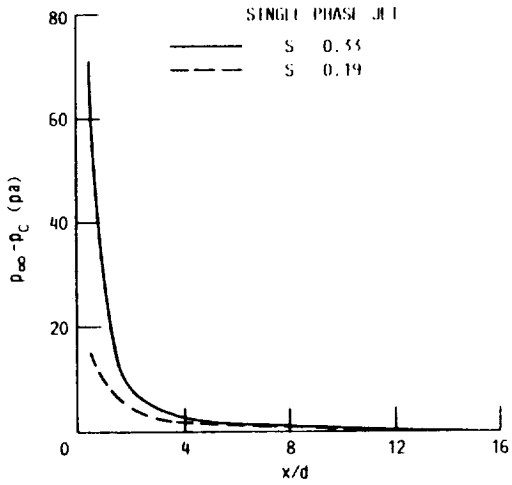

Figure 4.30. - Predicted variation of static pressure along the axis for the single-phase swirling jets (S = 0.19 and 0.33).

effects of streamline curvature, based on the flux Richardson number, generally improved the predictions.

4.2 Particle-Laden Jets

4.2.1 No-Swirl Conditions

Measurements and predictions, using the three two-phase flow models for the nonswirling jet are discussed in this section. Initial conditions for the particle-laden jets were measured at $x/d = 0.5$: the results of these measurements are illustrated in figures 4.31 and 4.32 for, $S = 0$.

Figure 4.31 illustrates number-averaged particle velocities which are averaged over all size groups, while figure 4.32 illustrates mean particle axial velocities for particle diameters of 23, 43, and 63 μm. From figure 4.32, it is evident that at $x/d = 0.5$, the larger particles are moving slower than the smaller particles at the center of the jet, but their radial profile is flatter than the smaller particles so the larger particles are moving faster near the edge of the jet. Differences in axial velocity between size groups are quite large near the edge of the jet.

A single loading ratio of 0.2 was used for all test conditions (summarized in table 2.4) and the particles had an SMD of 39 μm with a standard deviation of 15 μm. Because of instrument limitations, only mean and fluctuating axial velocities of the gas phase could be measured, as discussed in the Experimental Methods section. Therefore, it was necessary to estimate initial values of turbulence

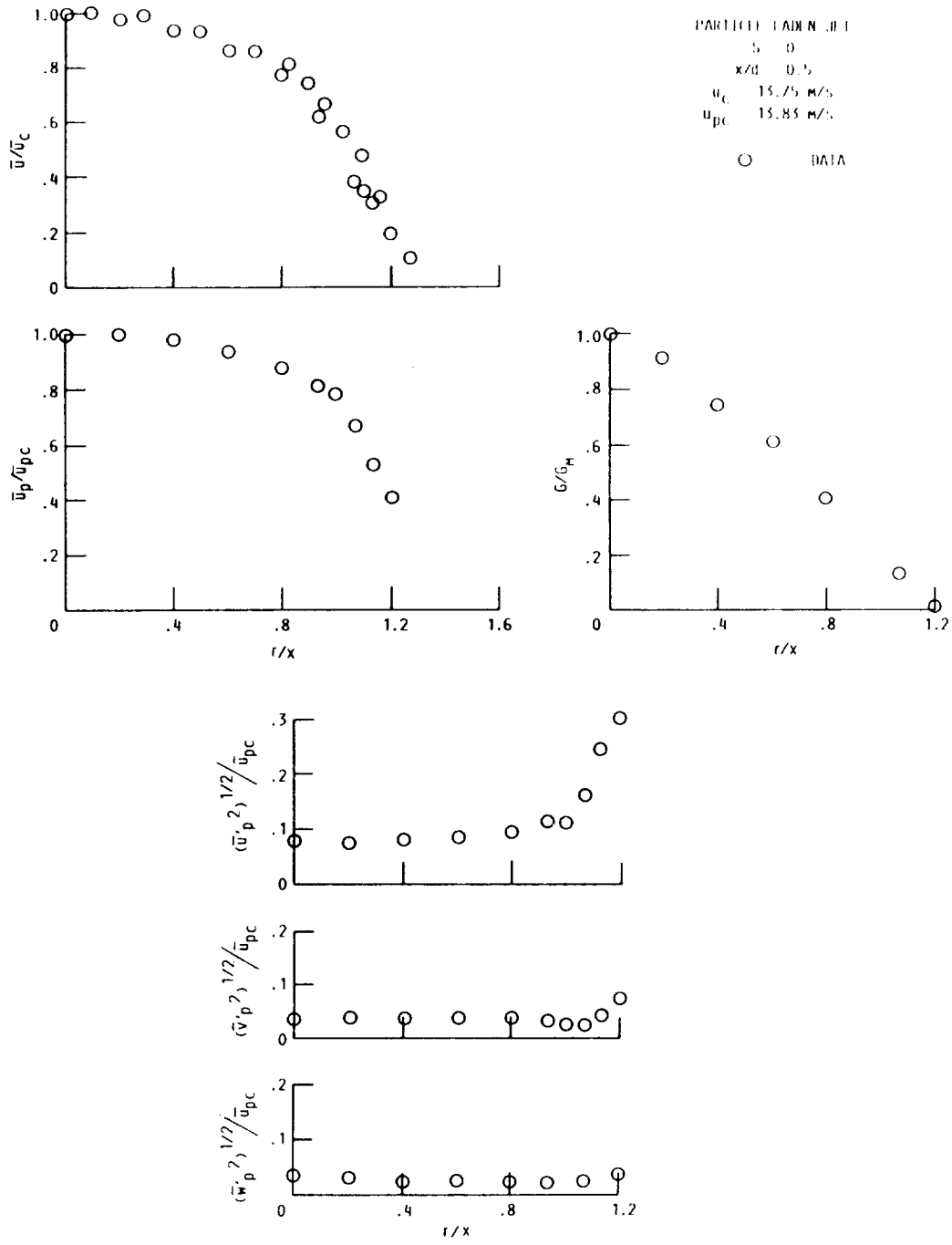

Figure 4.31. - The initial conditions for the particle-laden jet at x/d = 0.5 (S = 0).

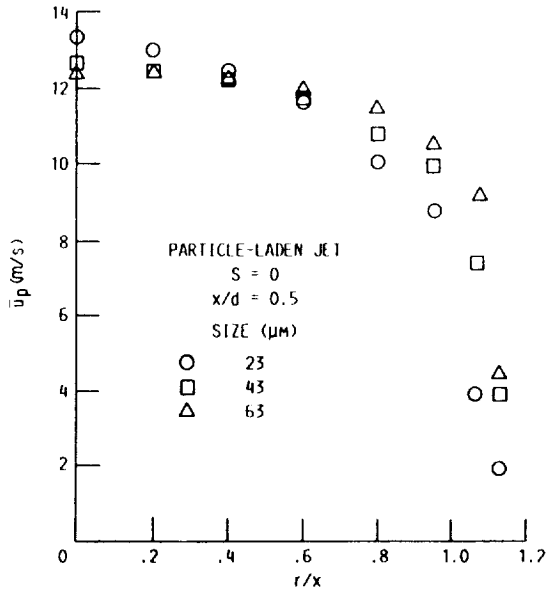

Figure 4.32. - Radial variation of mean axial velocity of 23, 43, and 63 micron particles at x/d = 0.5 (S = 0).

kinetic energy for the gas phase. For the predictions shown, initial values of k were assumed to be the same as the single-phase flows. Measured values of $(u'^2)^{1/2}$ for the gas phase were approximately 20 percent lower across the entire jet width for the particle-laden jets (at the initial condition of $x/d = 0.5$) than for the corresponding single-phase jets. Predictions showed that reductions of k of 20 percent caused negligible changes in flow properties, however, except very close to the injector. Initial values of ε for the particle-laden jet predictions were also unchanged from the single-phase jets. For predictions using the separated-flow models, seven particle size groups ranging in size from 12.5 to 72.5 microns in 10 micron increments were tracked through the flowfield. Measured mean and fluctuating particle axial velocities at $x/d = 0.5$ from the phase/Doppler particle anemometer were used as initial conditions. Initial values of mean and fluctuating particle radial velocities were taken from LV measurements at $x/d = 0.5$, which were number averaged over all particle sizes. Fluctuating gas-phase axial velocities are not shown in figure 4.32, however, they, along with all data taken during the present study, are tabulated in Appendix C.

The predicted and measured variation of axial velocities in the streamwise direction for the nonswirling, particle-laden jet are illustrated in figure 4.33. Measured particle velocities reported in figure 4.33 are number averaged over all particle sizes. For comparison with these measurements, predictions from the

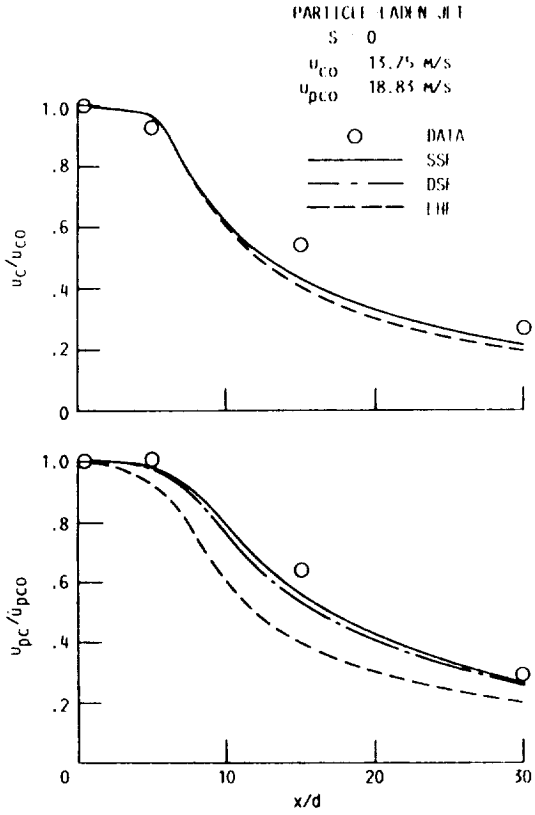

Figure 4.33. - Streamwise variation of number averaged axial velocity for the particle-laden jet (S = 0).

separated-flow models were number averaged over all seven size groups as well. By comparing figures 4.1 and 4.33, it is evident that axial velocity decays more slowly for the particle-laden flow than for the single-phase flow due to momentum exchange from the particles. Because the particle loading ratio is relatively low, predictions from both the locally homogeneous flow and stochastic separated flow models are nearly identical and also show reasonably good agreement with the experimental measurements. For the gas-phase axial velocity, deterministic separated flow model predictions were identical to those from the stochastic separated flow model and are not shown. Predictions using the locally homogeneous flow and separated-flow models for particle axial velocities show distinct differences. The neglect of particle inertia, illustrated by predictions from the locally homogeneous flow model, overestimates the rate of decay of particle axial velocity. Predictions from both the stochastic and deterministic models are similar and show reasonably good agreement with measurements for particle axial velocity decay.

Radial profiles of flow properties, number averaged over all particle sizes, for the particle-laden jets without swirl, are illustrated in figures 4.34 to 4.36. Measurements and predictions are illustrated for $x/d = 5$, 15, and 30. Gas-phase jet widths are slightly overestimated for the particle-laden flows at $x/d = 15$ and 30, see figures 4.35 and 4.36. The overestimation of gas-phase flow width is probably caused by turbulence modulation due to the

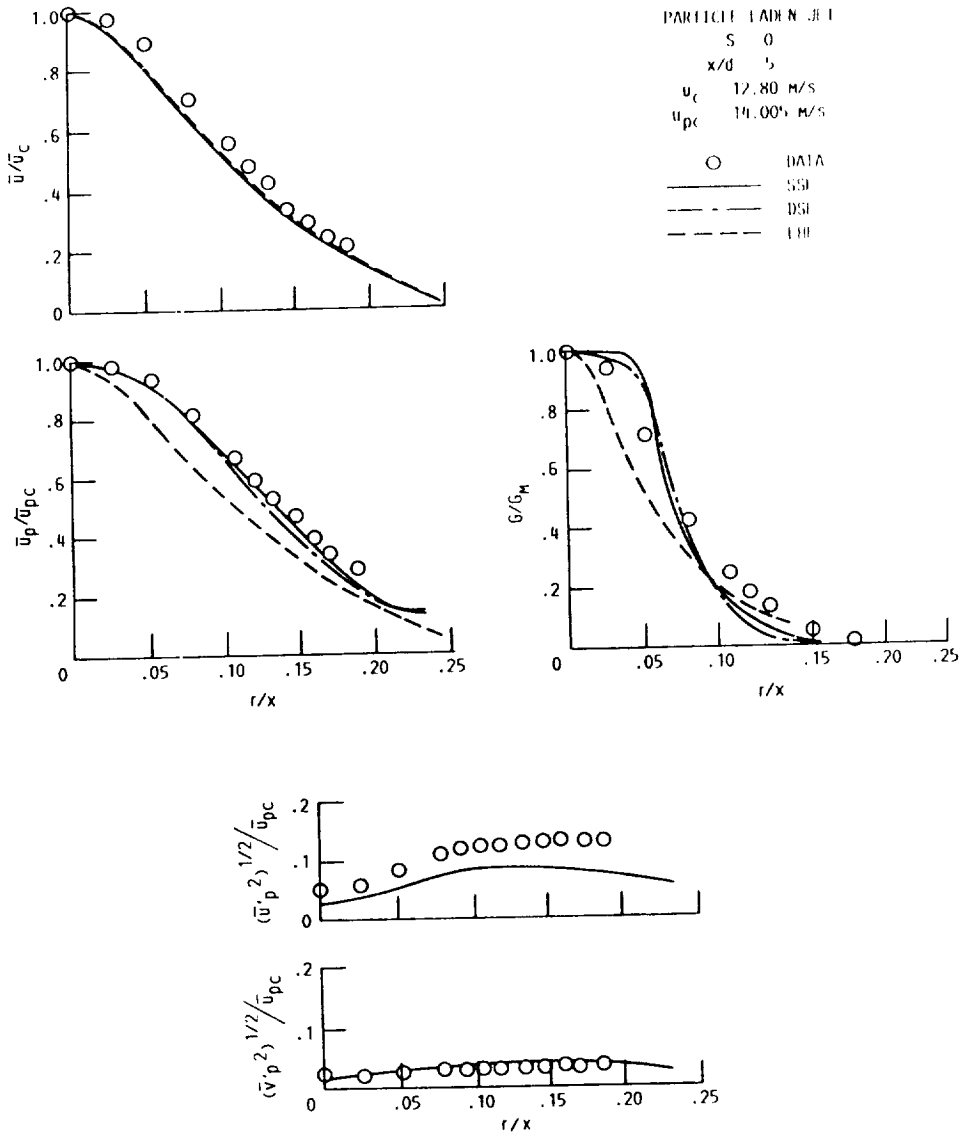

Figure 4.34. - Radial variation of number-averaged flow properties at x/d = 5 for the particle-laden jet (S = 0).

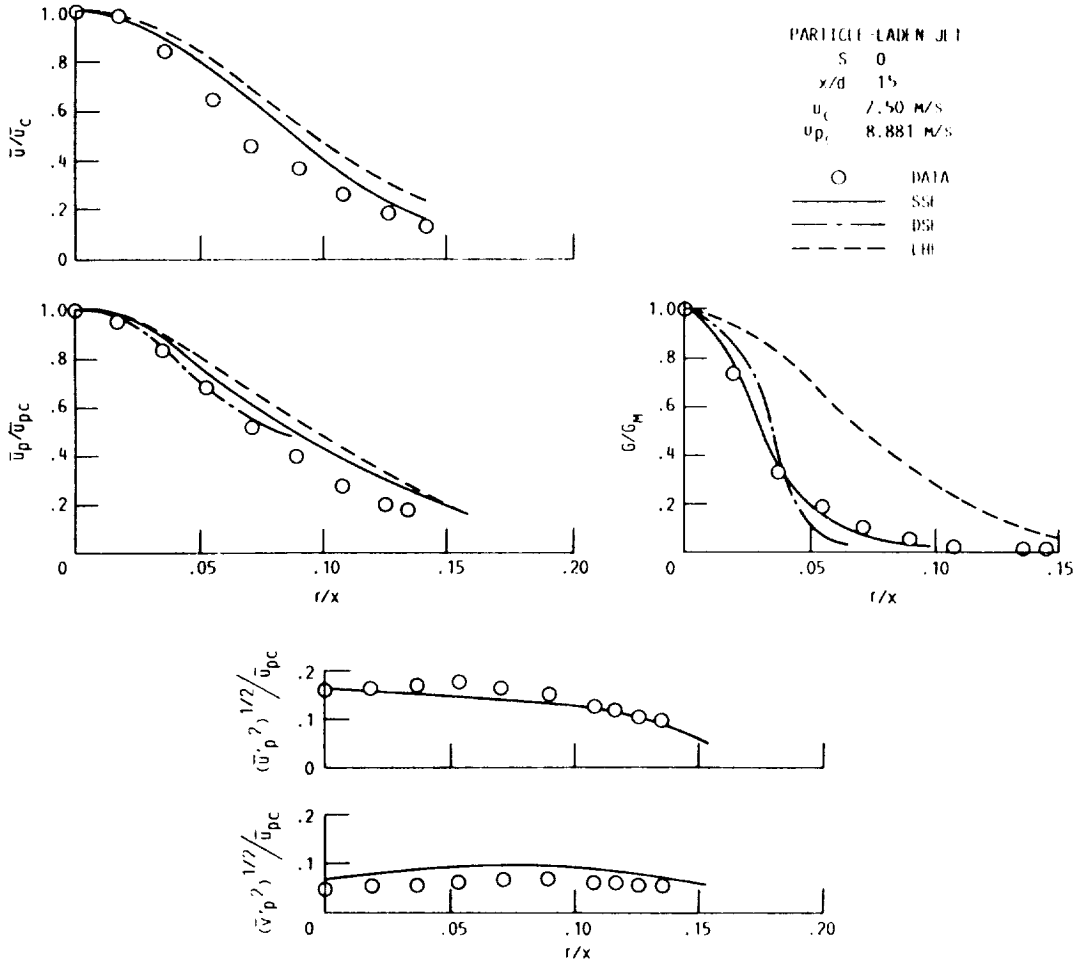

Figure 4.35. - Radial variation of number-averaged flow properties at x/d = 15 for the particle-laden jet (S = 0).

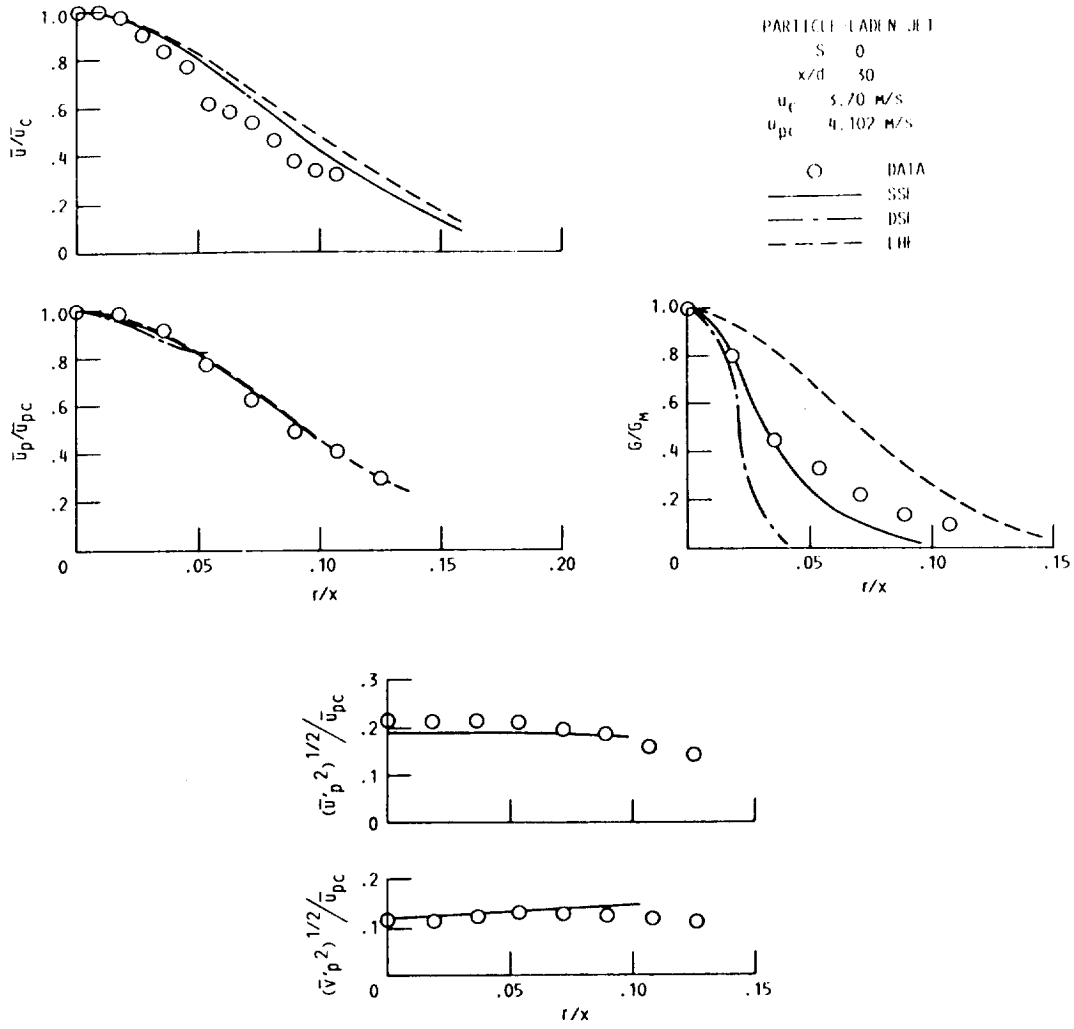

Figure 4.36. - Radial variation of number-averaged flow properties at x/d = 30 for the particle-laden jet (S = 0).

particles. Even though the loading ratio was relatively low, values of $(u'^2)^{1/2}$ for the particle-laden jets are reduced compared to the single-phase jets. The reductions in fluctuating velocities reduce turbulent mixing rates and, thus, the jet width. Particle axial velocity profiles are reasonably well predicted by all the models, however, since the locally homogeneous flow model overestimates the rate of axial velocity decay with streamwise distance, the values of axial velocity predicted by this approach are generally lower than the measurements.

Radial profiles of particle mass flux illustrate the different physical assumptions embodied in the three models. As illustrated in figures 4.35 and 4.36, the no-slip assumption of the locally homogeneous flow model causes the radial dispersion of the particles to be overestimated. At $x/d \leq 15$, both separated-flow models give similar predictions of particle mass flux. However, at larger streamwise distances, see figure 4.36, the neglect of turbulent dispersion of the particles causes the deterministic separated flow model to underestimate the spread of the particles. Since mean gas-phase radial velocities are quite small at these axial distances, turbulent dispersion is the only mechanism available for radial spread of the particles. Only the stochastic separated flow model, which accounts for both particle inertia and turbulent disperison of the particles, correctly predicts the radial distribution of particle mass flux at $x/d = 30$ (see figure 4.36).

The predictions of fluctuating particle properties for the stochastic separated flow model, also illustrated in figures 4.34 to 4.36, are reasonably good, however, $(\overline{u_p'^2})^{1/2}$ is slightly underestimated at x/d = 30. This is probably caused by the assumption of isotropic velocity fluctuations, which causes streamwise continuous-phase velocity changes experienced by the particle to be underestimated. In particular, measured values of $(\overline{u'^2})^{1/2}$ were always greater than $(\overline{v'^2})^{1/2}$ and $(\overline{w'^2})^{1/2}$ for the single-phase jet and it is expected that this behavior should be similar for the particle-laden jet.

These results for the particle-laden jets without swirl are similar to those previously reported by other investigators for similar flows (38 to 41).

Measurements and predictions of particle mean axial velocity for 23, 43, and 63 μm particles at x/d = 5, 15, and 30 are illustrated in figure 4.37 for the nonswirling jet. Only predictions from the stochastic separated flow model are presented. As illustrated in figure 4.37, decay of axial velocity of the larger particles is slower than the smaller particles. By x/d = 15, the 63 micron particles have the highest velocity. Predictions from the stochastic separated flow model are in reasonably good agreement with measurements and correctly show the general trends.

4.2.2 Swirling Conditions

Measurements and predictions for the particle-laden swirling jets are discussed in this section. Initial conditions for the

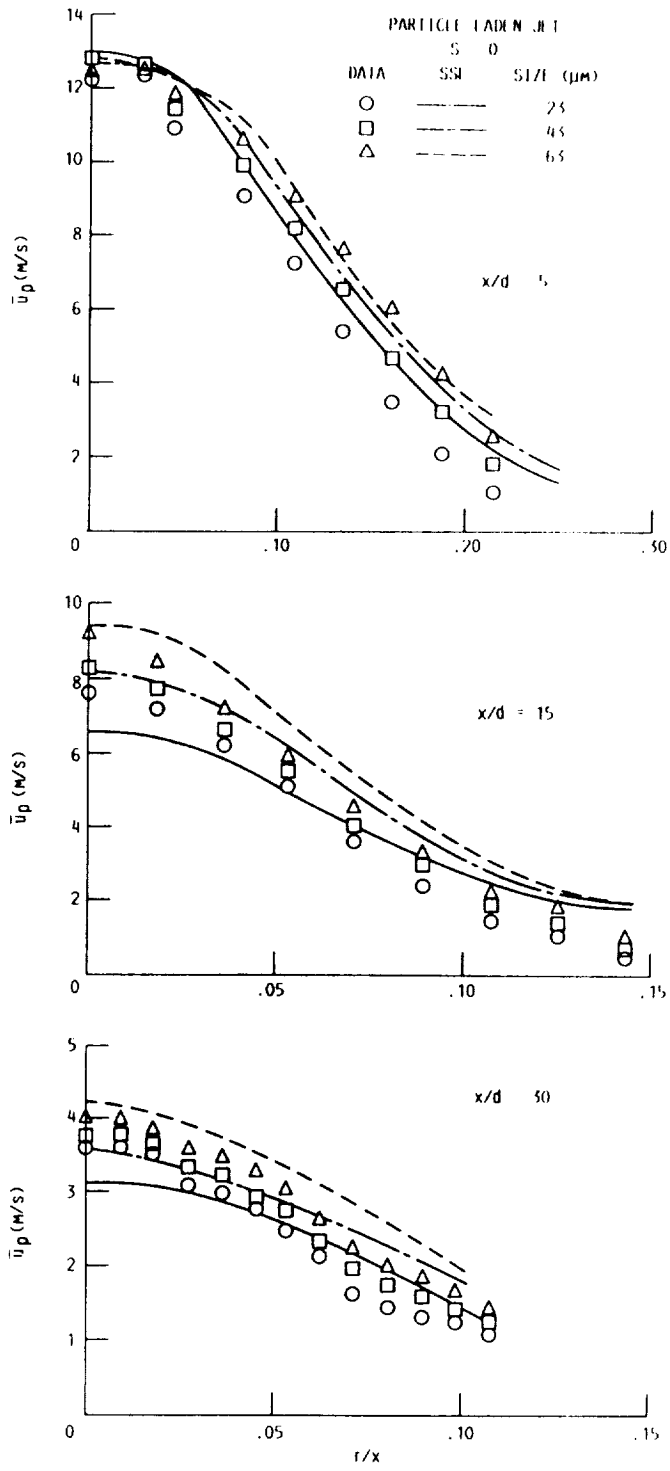

Figure 4.37. - Radial variation of mean axial velocity of 23, 43, and 63 micron particles at x/d = 5, 15, and 30 (S = 0).

particle-laden swirling jets were measured at $x/d = 0.5$. Jets having swirl numbers of $S = 0.16$ and 0.3 were studied. A single loading ratio of 0.2 was also used for the swirling flows. Test conditions are summarized in table 2.4. As previously discussed, LV particle velocity measurements were number averaged over all particle sizes. In addition, simultaneous particle sizes and axial velocities were measured using the phase/Doppler particle anemometer.

Measurements of flow properties, averaged over all particle sizes, are illustrated in figures 4.38 and figure 4.39 for the particle-laden swirling jets. Mean axial velocities of 23, 43, and 63 μm particles at $x/d = 0.5$, are illustrated in figure 4.40. It is apparent that the presence of swirl has a large effect on the particle-laden jets, see figures 4.38 and 4.39. Compared to the jet without swirl, the maximum particle mass flux has shifted outward from the centerline of the jet to $r/x = 0.8$. Particle velocity fluctuations also increase with increasing swirl. In addition, increasing swirl also increases the variation of mean axial velocity with particle size, as illustrated in figure 4.40. At $x/d = 0.5$, larger particles are moving at a lower axial velocity than smaller particles throughout most of the jet. The radial velocity profile of the larger particles is much flatter than the smaller particles: as a result, the velocities of the larger particles are greater than the smaller particles near the edge of the jets. Fluctuating particle axial velocities for each size group are not shown in the figures but are tabulated in Appendix C.

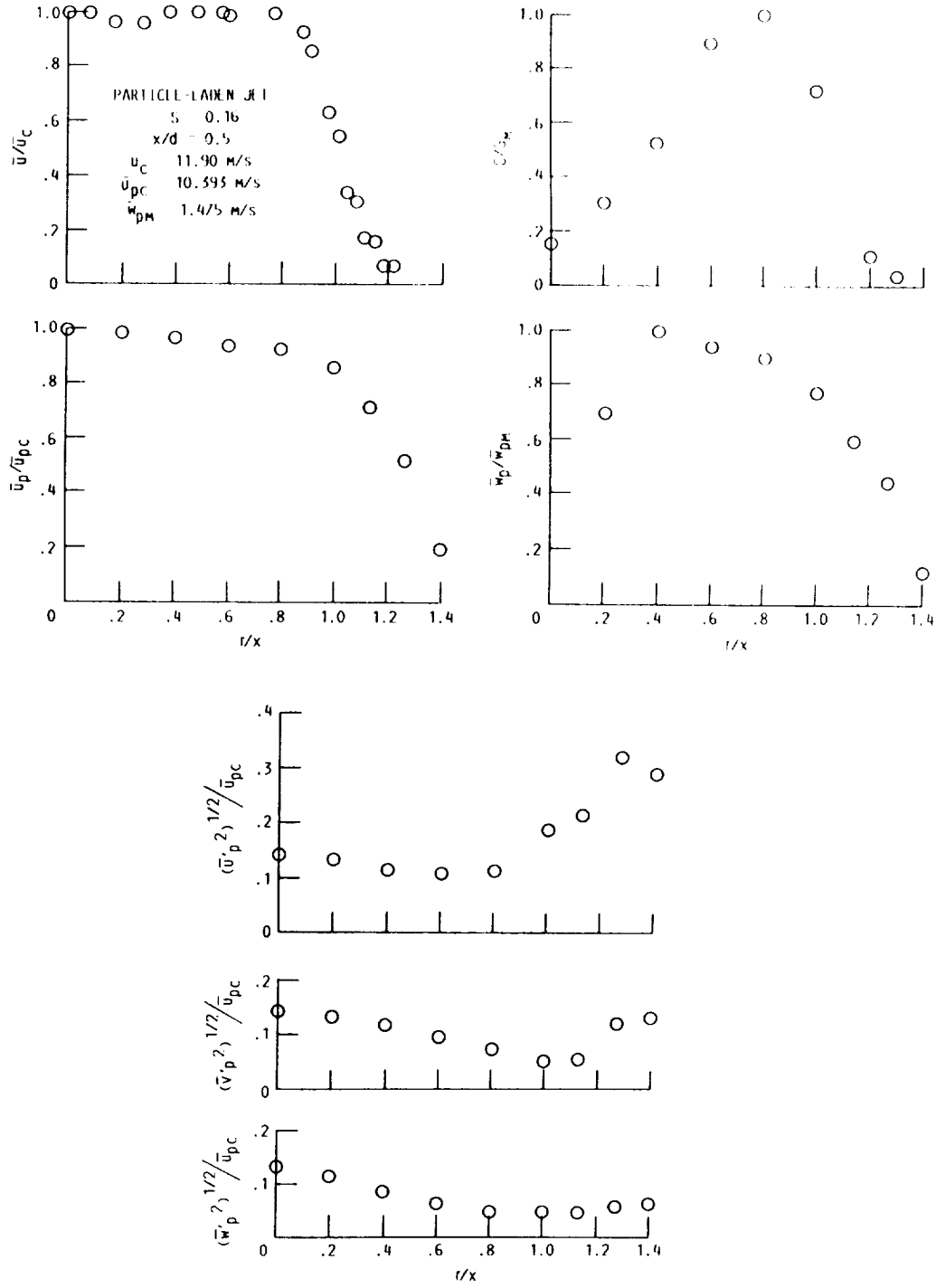

Figure 4.38. - The number-averaged initial conditions for the particle-laden swirling jet (S = 0.16)--radial variation of flow properties at x/d = 0.5.

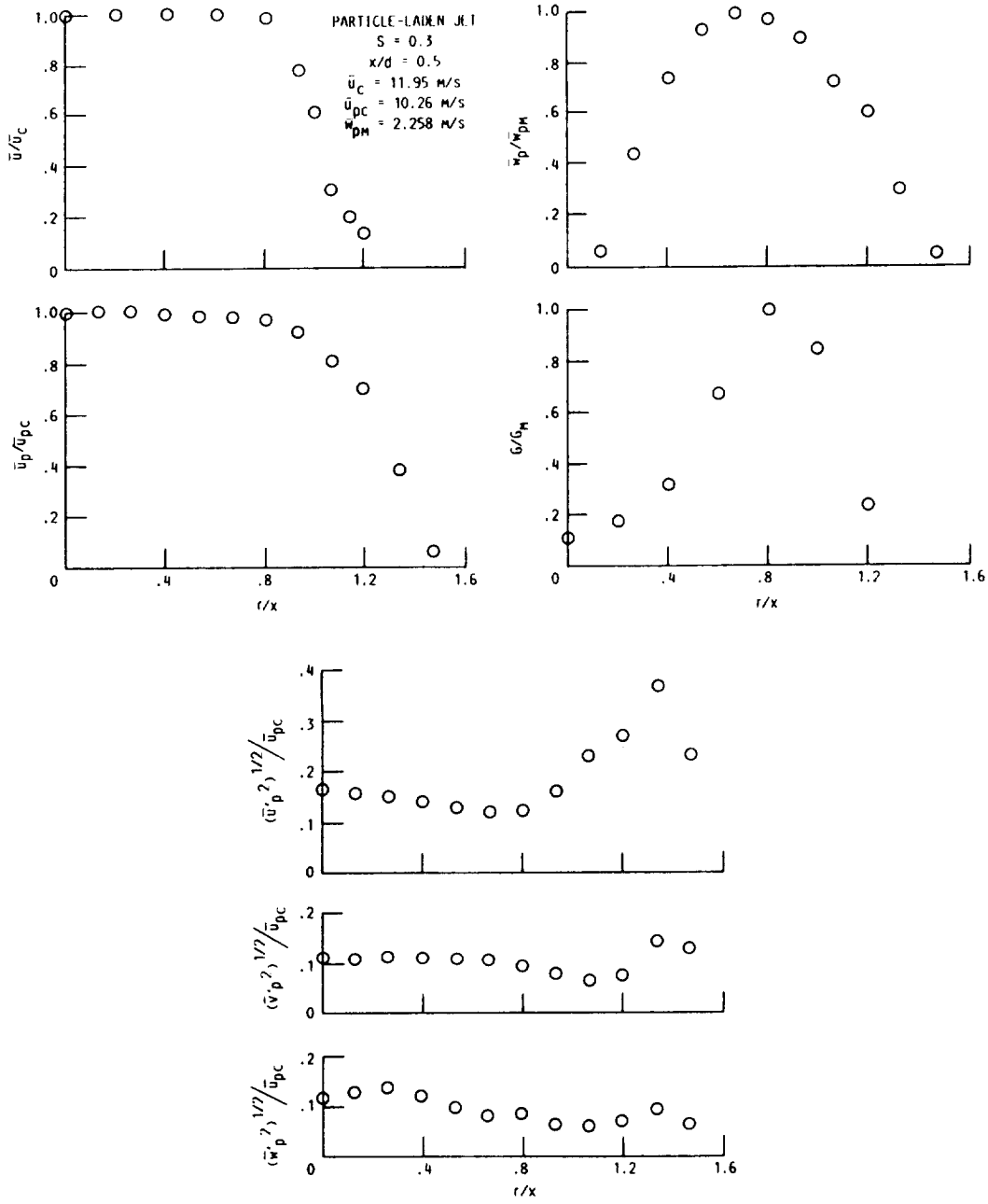

Figure 4.39. - The number-averaged initial conditions for the particle-laden swirling jet (S = 0.3)--radial variation of flow properties at x/d = 0.5.

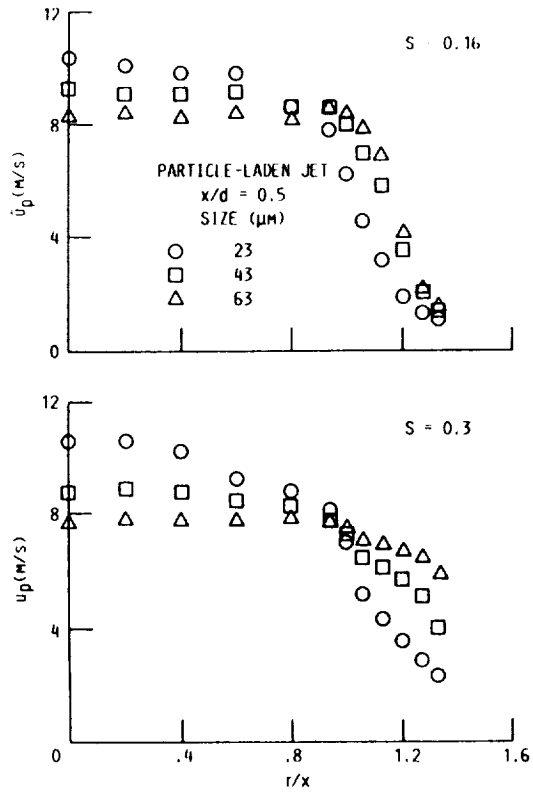

Figure 4.40. - Radial variation of mean axial velocity for 23, 43, and 63 micron particles at x/d = 0.5 for the particle-laden swirling jets (S = 0.16 and 0.3).

As discussed earlier for the particle-laden jets, only mean and fluctuating axial velocities of the gas phase could be measured. Thus, it was necessary to estimate initial values of the gas-phase angular velocity and the turbulence kinetic energy in order to initiate calculations. The initial angular velocity of the continuous phase was estimated by subtracting the measured initial particle-phase angular momentum from the values obtained for the single-phase flows. For both swirling flows, particle-phase angular momentum was approximately 10 percent of the measured single-phase angular momentum. Initial values of k and also ε were assumed to be the same as the single-phase flows. Separated-flow predictions were made using seven particle size groups having diameters ranging from 12.5 to 72.5 μm, in 10 μm increments. Initial values of particle mean and fluctuating axial velocities for each size group were obtained from phase/Doppler measurements at $x/d = 0.5$. Initial values of particle radial and angular velocities were assumed to be identical for all size groups, and were obtained from number-averaged LV measurements. Sensitivity of the predictions to initial values is discussed in a later section.

Predicted and measured flow properties in the streamwise direction are illustrated in figures 4.41 to 4.43 for the swirling particle-laden jets. Only the standard $k - \varepsilon$ turbulence model was employed for predictions of the particle-laden flows reported in the following. Reasons for not considering a correction for streamline curvature are discussed later.

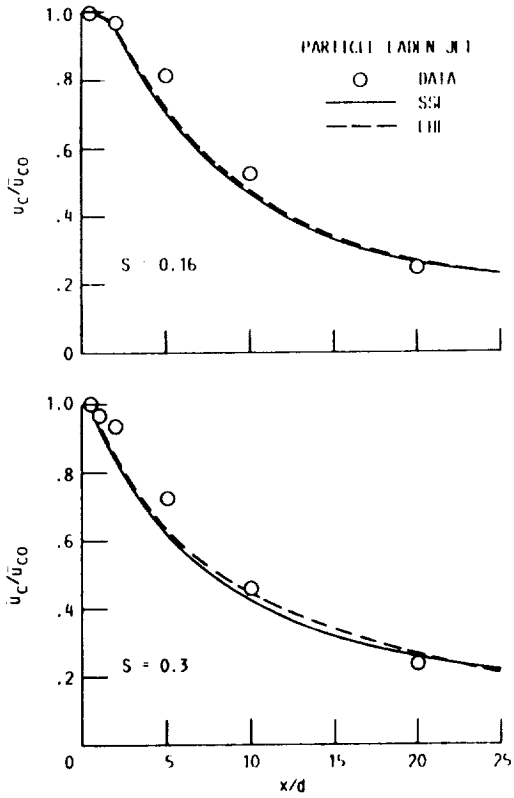

Figure 4.41. - Streamwise variation of gas-phase axial velocity for the particle-laden swirling jets (S = 0.16 and 0.3).

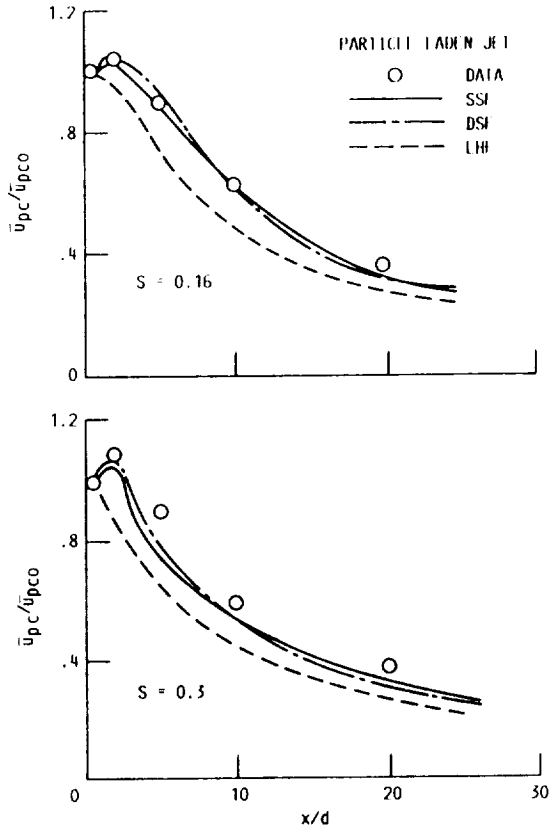

Figure 4.42. - Streamwise variation of number-averaged particle axial velocity for the particle-laden swirling jets (S = 0.16 and 0.3).

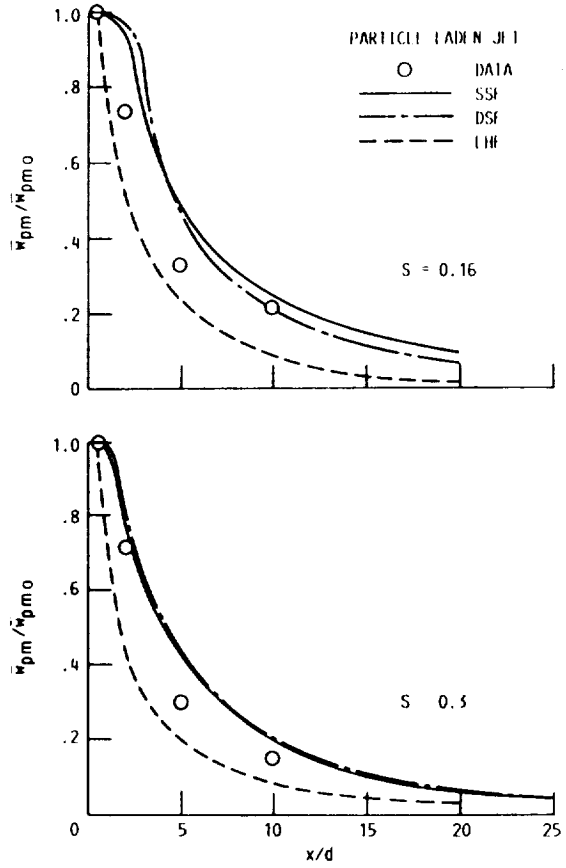

Figure 4.43. - Streamwise variation of number-averaged particle maximum angular velocity for the particle-laden swirling jets (S = 0.16 and 0.3).

Predicted and measured gas-phase axial velocities are shown in figure 4.41 for swirl numbers of 0.16 and 0.3. As illustrated in figure 4.41, increasing swirl increases the rate of decay of axial velocity, similar to single-phase flows. Predictions from the locally homogeneous flow and stochastic separated flow models are nearly identical and show reasonably good agreement with measurements for both swirling flows. Again, predictions of gas-phase axial velocity using the deterministic separated flow model are nearly identical to predictions using the stochastic separated flow model and are not shown in the figure.

Particle mean axial and maximum angular velocities, number averaged over all particle sizes, are plotted as a function of streamwise distance in figures 4.42 and 4.43, respectively. As expected, neglecting slip between the phases causes predictions from the locally homogeneous flow model to overestimate the rate of decay of particle velocities. Differences between predictions from the deterministic and stochastic separated flow models were small: both show good agreement with measurements. At the initial condition (x/d = 0.5), axial velocities of the particles were lower than the continuous phase except near the edge of the jet for both swirling flows, see figures 4.38 and 4.39. Particle axial velocities initially increase, due to momentum exchange from the continuous phase, before beginning to decay. As can be seen from figure 4.42, both separated-flow models correctly predict this behavior.

Radial profiles of flow properties for the particle-laden swirling jets are illustrated in figures 4.44 to 4.53. Velocity measurements, number averaged over all particle sizes, are illustrated in figures 4.44 to 4.51. Particle mean axial velocities for three size groups are illustrated in figures 4.52 and 4.53 for the two swirling flows.

Measurements and predictions of radial flow profiles at $x/d = 2$ are illustrated in figures 4.44 and 4.45 for $S = 0.16$ and $S = 0.3$, respectively. Similar to the results observed for the nonswirling particle-laden flow, predictions of gas-phase velocities using the locally homogeneous flow and stochastic separated flow models are nearly identical and both slightly overestimate the gas-phase flow width. Again, the probable cause is turbulence modulation by the particles, which was not considered by the present models. All predictions reported here employed the standard $k - \varepsilon$ turbulence model. For single-phase jets with swirl, the jet width was always underestimated using the standard $k - \varepsilon$ turbulence model and streamline curvature modifications were introduced which increased the predicted jet width. Because of the turbulence modulation by the particles, predictions with the streamline curvature modification showed even poorer agreement with the measurements than the standard $k - \varepsilon$ model and are not illustrated in the figures. At $x/d = 2$, the stochastic separated flow model overestimates particle velocities for r/x greater than about 0.2. Predictions of particle axial velocity

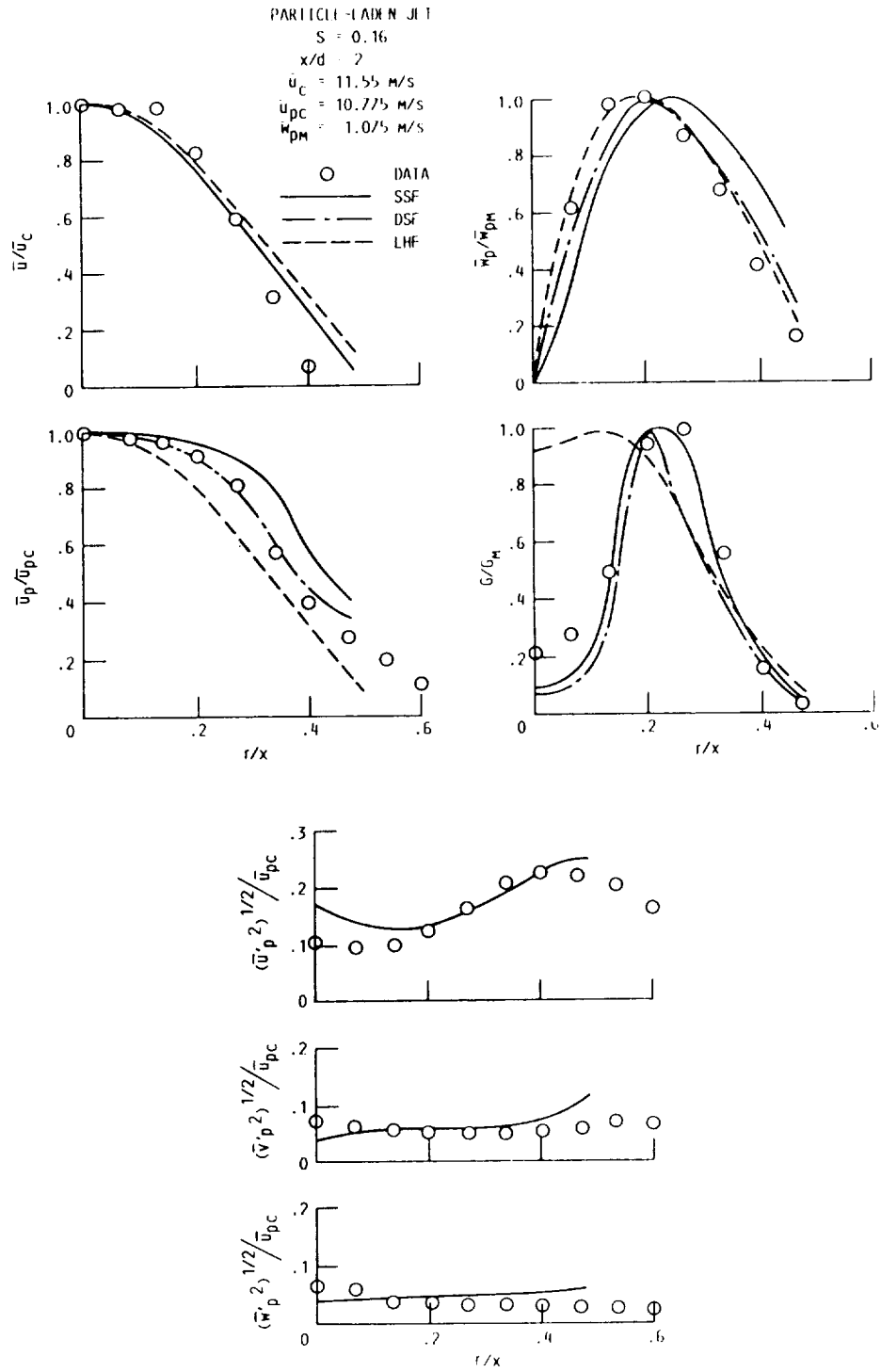

Figure 4.44. - Radial variation of number-averaged flow properties at x/d = 2 for the particle-laden swirling jet (S = 0.16).

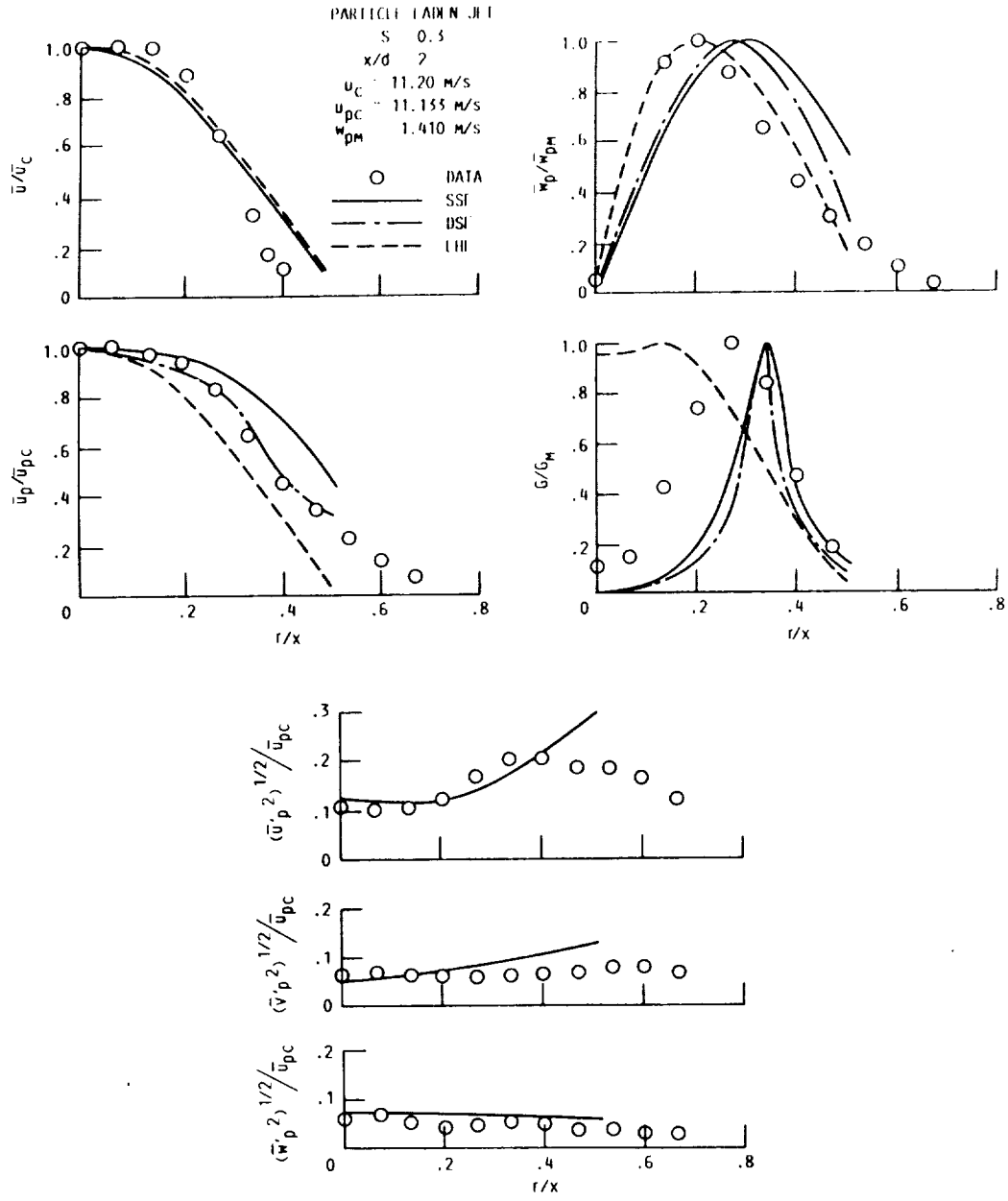

Figure 4.45. - Radial variation of number-averaged flow properties at x/d = 2 for the particle-laden swirling jet (S = 0.3).

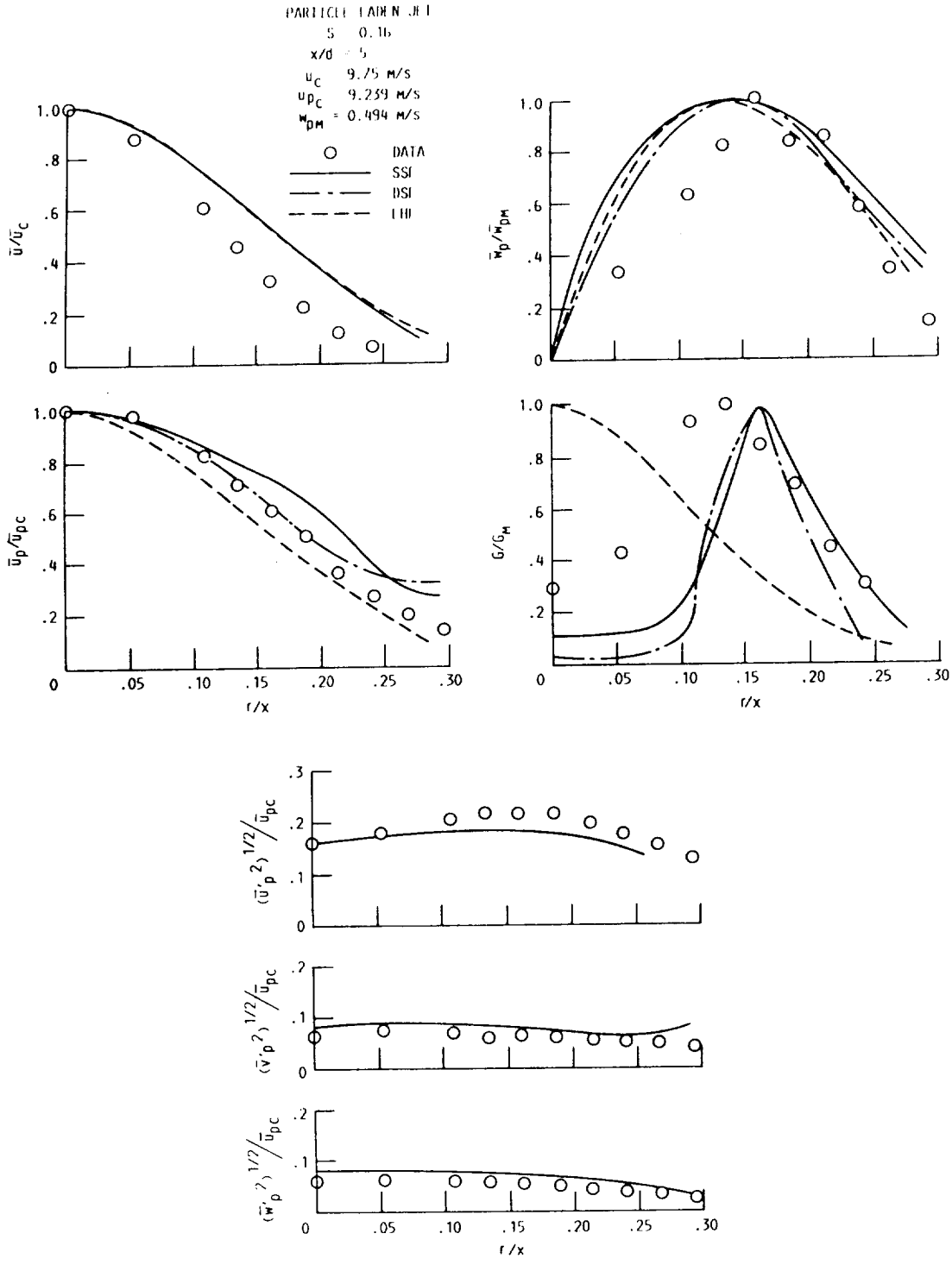

Figure 4.46. - Radial variation of number-averaged flow properties at x/d = 5 for the particle-laden swirling jet (S = 0.16).

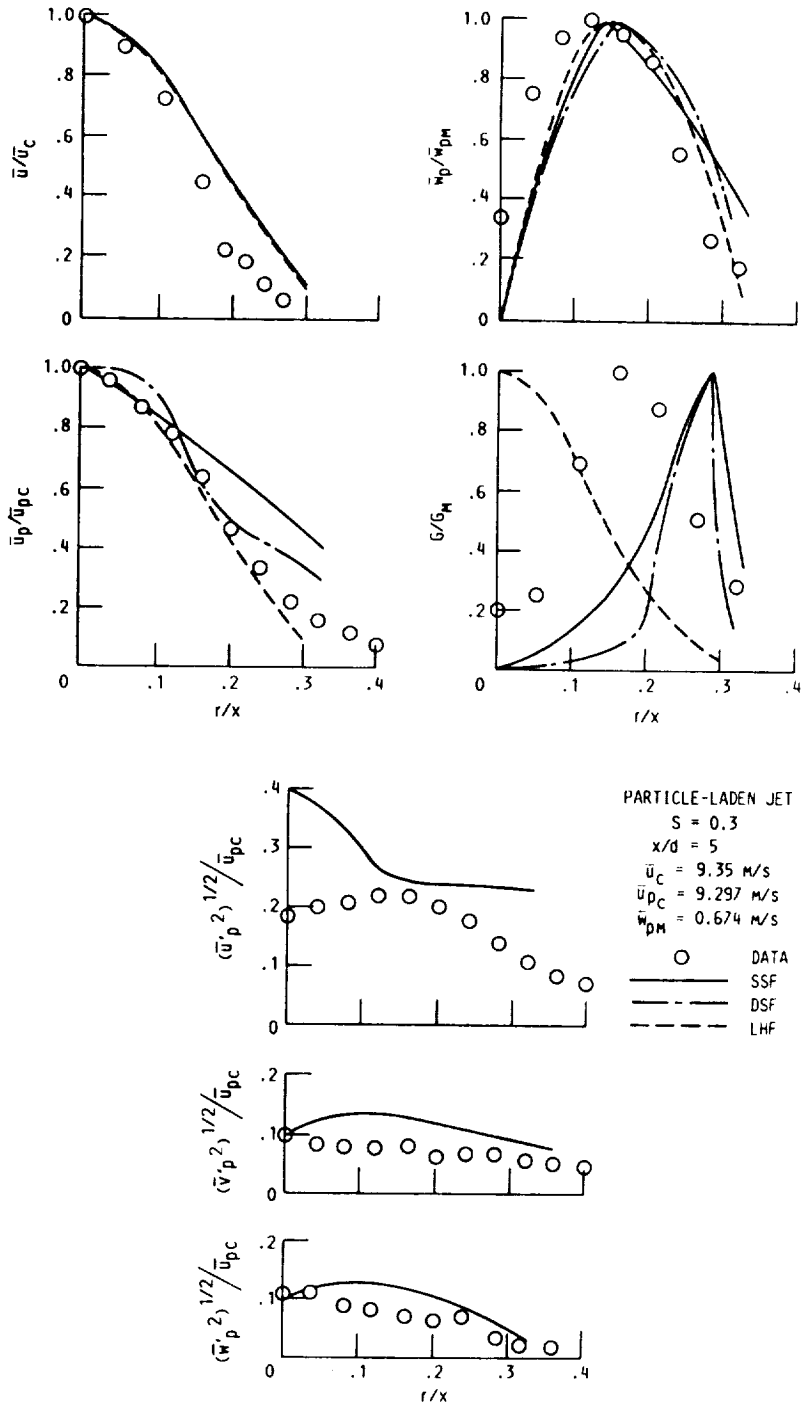

Figure 4.47. - Radial variation of number-averaged flow properties at x/d = 5 for the particle-laden swirling jet (S = 0.3).

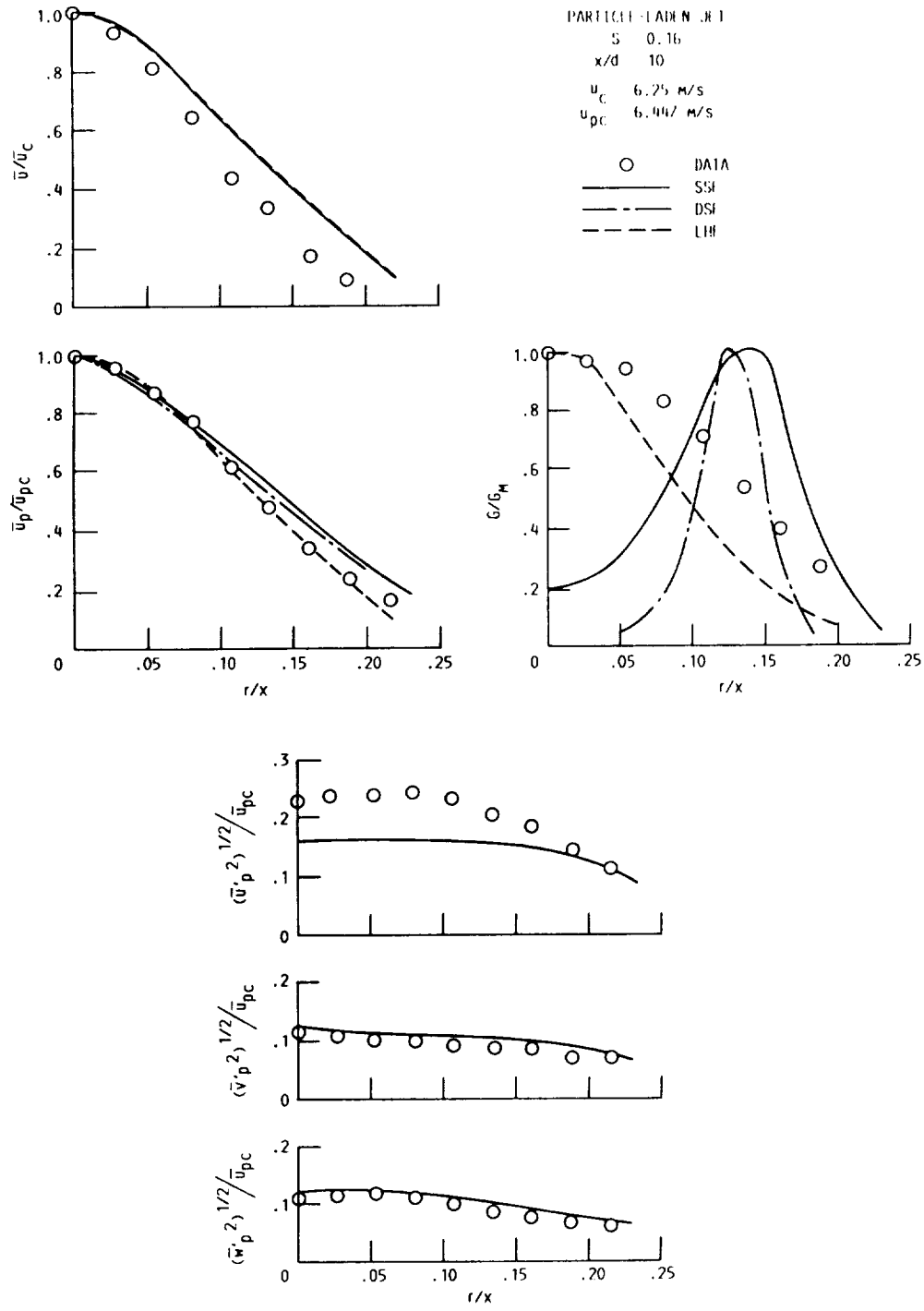

Figure 4.48. - Radial variation of number-averaged flow properties at x/d = 10 for the particle-laden swirling jet (S = 0.16).

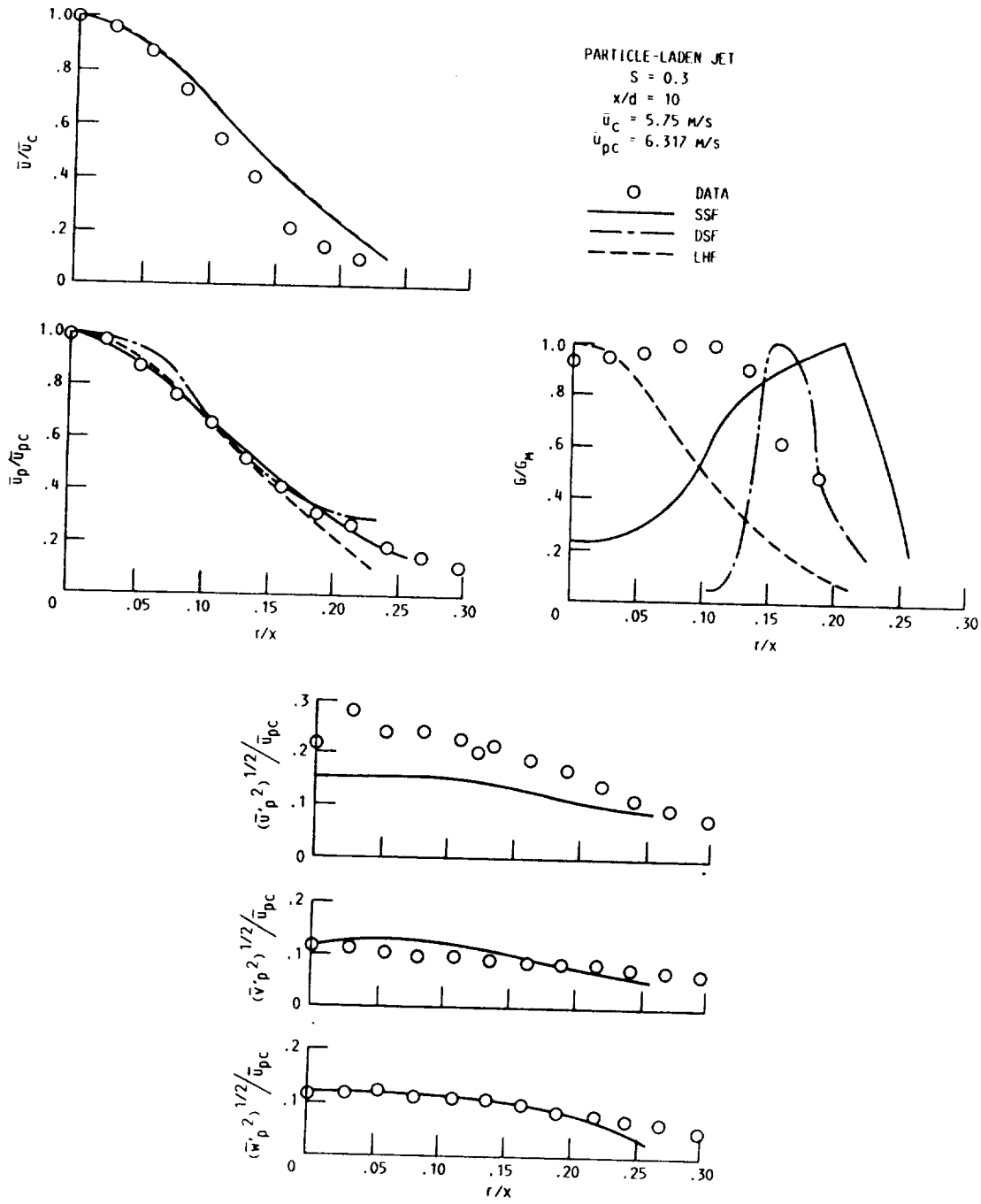

Figure 4.49. - Radial variation of number-averaged flow properties at x/d = 10 for the particle-laden swirling jet (S = 0.3).

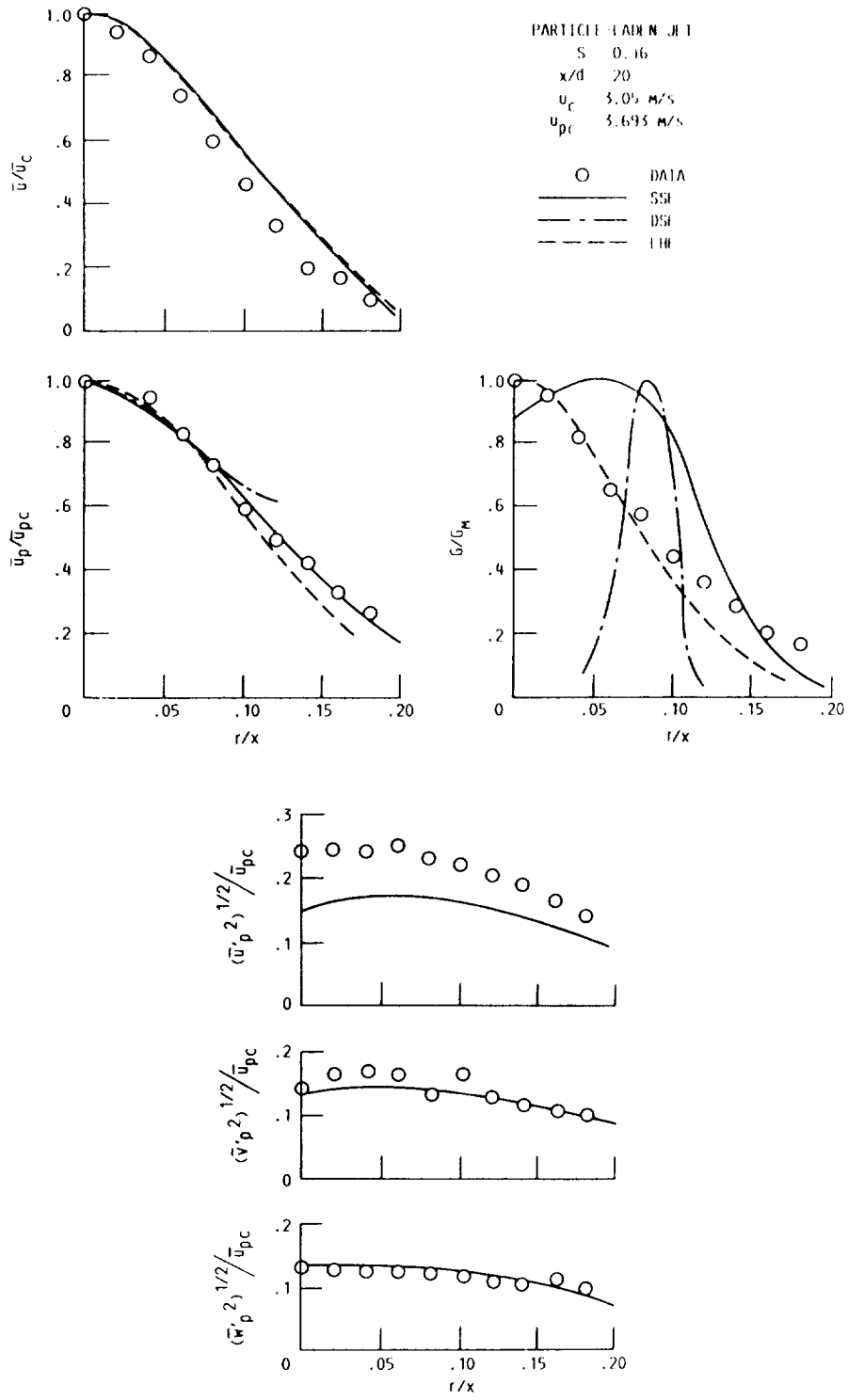

Figure 4.50. - Radial variation of number-averaged flow properties at x/d = 20 for the particle-laden swirling jet (S = 0.16).

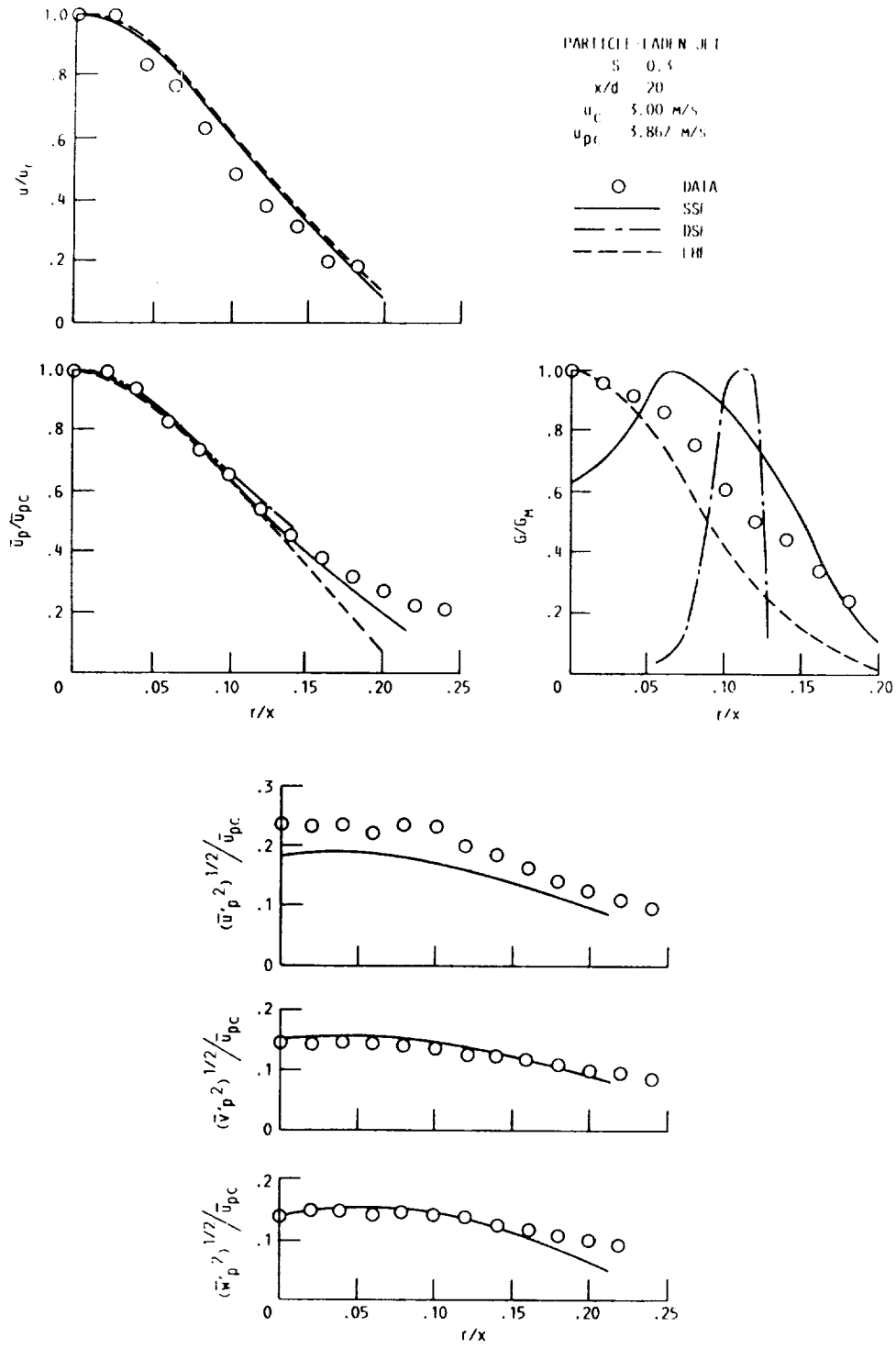

Figure 4.51. - Radial variation of number-averaged flow properties at x/d = 20 for the particle-laden swirling jet (S = 0.3).

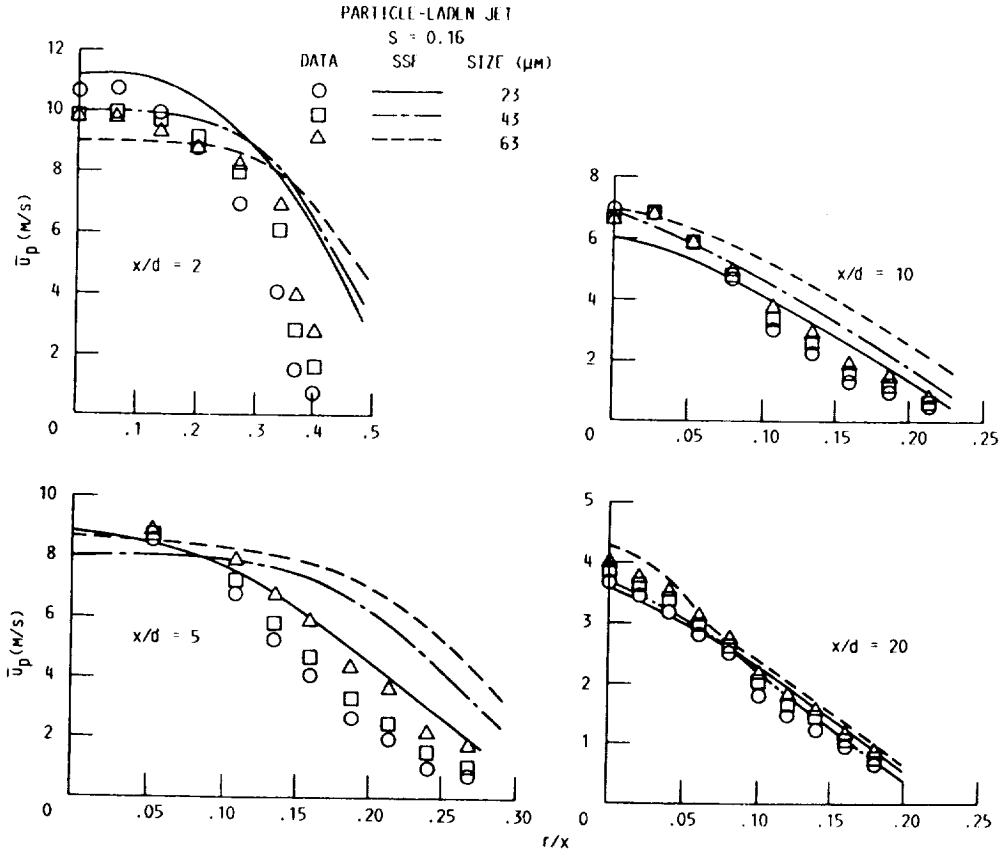

Figure 4.52. - Radial variation of mean axial velocity for 23, 43, and 63 micron particles at x/d = 2, 5, 10, and 20 for the particle-laden swirling jet (S = 0.16).

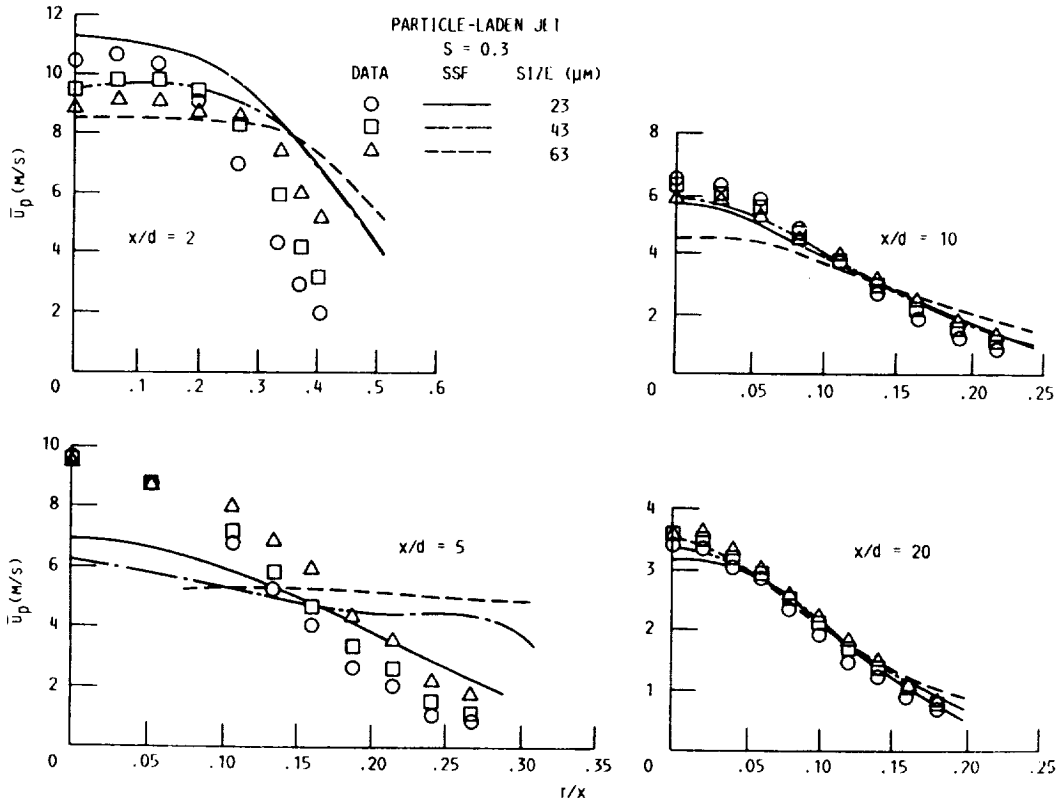

Figure 4.53. - Radial variation of mean axial velocity for 23, 43, and 63 micron particles at x/d = 2, 5, 10, and 20 for the particle-laden swirling jet (S = 0.3).

from the deterministic separated flow model show the best agreement with the measurements at $x/d = 2$. The locally homogeneous flow model underestimates particle axial velocity due to the neglect of particle inertia. Predictions this close to the injector exit are extremely sensitive to initial conditions, however, which may be a factor in these results.

The radial profile of particle mass flux illustrates the differences between the three models. In contrast to the nonswirling flow, the peak particle mass flux for the swirling flows is not found at the centerline of the jet, but is shifted radially outward due to centrifugal forces. Calculations for all three models were initiated at $x/d = 0.5$ using the experimentally measured particle mass fluxes as initial conditions. As illustrated in figures 4.44 and 4.45, the locally homogeneous flow model predicts a shift in the maximum mass flux to the center of the jet, because turbulent dispersion of the particles is overestimated due to the no-slip assumption. Predictions of particle mass flux from both of the separated-flow models are similar and show better agreement with measurements. Stochastic separated flow model predictions of particle fluctuating velocities at $x/d = 2$ are also illustrated in figures 4.44 and 4.45 and show good agreement with measurements. Even though continuous-phase fluctuations are assumed to be isotropic, predicted fluctuating particle axial velocities are greater than fluctuating radial or angular velocities because particles with different axial velocities

are transported radially by fluctuating radial and angular velocities. Also illustrated in figures 4.44 and 4.45 are particle angular velocities. Angular velocities at $x/d = 2$ appear to be better predicted using the locally homogeneous flow model, however, this may be the result of inaccurate initial gas-phase angular velocities or the assumption of equal initial angular velocities of all size groups, as discussed earlier. Measured angular velocities also have relatively high uncertainties, as discussed in Appendix A.

Radial profiles of number-averaged flow properties for the swirling, particle-laden jets at $x/d = 5$ are illustrated in figures 4.46 and 4.47 for $S = 0.16$ and 0.3, respectively. As expected, increasing the swirl number increases the width of the particle-laden jet, similar to the behavior observed for the single-phase jets. The gas-phase flow width is slightly overestimated at $x/d = 5$ for both swirling flows. Again, this is probably due to turbulence modulation by the particles, as discussed earlier. Also, because the gas-phase flow width is overestimated, particle axial velocities are also overestimated for the separated-flow models. The stochastic separated flow model overestimates particle axial velocities to a greater extent than the deterministic separated flow model. The locally homogeneous flow model, however, underestimates particle axial velocities, due to the neglect of particle inertia. At $x/d = 5$, particle axial velocities, number averaged over all size groups, are nearly equal to the continuous phase. A comparison between predictions and

measurements of particle mass flux at $x/d = 5$ shows similar results to those observed at $x/d = 2$. However, differences between the model predictions are more pronounced. For both swirling flows, the locally homogeneous flow model predicts the maximum particle mass flux at the center of the jet, which is clearly not correct. The neglect of turbulent dispersion of the particles, illustrated by the deterministic separated flow model, causes the particles to be confined to a relatively narrow region of the flow. If only mean properties of the continuous phase are considered, the particles are transported by centrifugal forces to regions where radial velocity is small and tend to remain there. Considering turbulent fluctuations of the continuous phase gives better predictions of particle mass flux at $x/d = 5$. The predicted maximum particle mass flux is shifted radially outward when compared to the measurements. This is again probably caused by the overestimation of jet width at this streamwise location. Predictions of mean particle angular velocities and fluctuating particle velocities are quite good for the $S = 0.16$ flow, see figure 4.46. For the higher swirl number flow, $S = 0.3$, particle fluctuating axial velocities are overestimated, however, predictions of the other two fluctuating particle velocities show better agreement with measurements.

At the streamwise location of $x/d = 10$, number-averaged particle velocities, averaged over all sizes, are greater than the continuous phase for both swirling flows considered during the present study.

Radial profiles of flow properties are illustrated in figures 4.48 and 4.49 for $S = 0.16$ and 0.3, respectively. The continuous-phase flow width is again slightly overestimated, however, predictions show better agreement with measurements at $x/d = 10$ than at locations closer to the injector. For the lower swirl number flow, $S = 0.16$, particle axial velocities are well predicted with the stochastic separated flow model. Predictions based on the locally homogeneous flow model also are quite good, however, this model overestimates the rate of decay of axial velocities see figure 4.42; therefore the unnormalized predicted velocities are lower than the measurements. At this streamwise distance, angular velocities have decayed to negligible values and are not reported. As illustrated in figures 4.48 and 4.49, the radial distribution of particle mass flux at $x/d = 10$ has significantly shifted from the profiles found at $x/d = 5$. By $x/d = 10$, the particles have dispersed sufficiently so that the maximum mass flux has shifted to the center of the jet for the $S = 0.16$ flow and is clearly headed in that direction for the $S = 0.3$ flow. Neglecting turbulent dispersion of the particles causes the particles to remain in a relatively narrow region for both swirling flows. For the $S = 0.3$ flow, no particles whatsoever are predicted for r/x less than about 0.1 with the deterministic separated flow model. The stochastic separated flow model does not adequately predict this abrupt shift in particle mass flux at this streamwise location. Predicted values of fluctuating radial and angular number-averaged particle

velocities are lower than measurements for both swirl flows. This is probably due to the assumption of isotropic velocity fluctuations for the eddies in the stochastic model.

Radial profiles of gas-phase properties at $x/d = 20$ are illustrated in figures 4.50 and 4.51 for both swirl flows. Predictions are in better agreement with measurements at this position than closer to the injector, although the jet width is still slightly overestimated. Predictions at $x/d = 20$ are not as sensitive to initial conditions and the swirl component has almost completely decayed. Again, there is little difference between predictions of gas-phase properties for the no-slip and separated-flow models. Predictions of axial velocities are in good agreement with measurements for all three models. However, since the locally homogeneous flow model overestimates the rate of decay of axial velocities, predicted unnormalized velocities from this model are lower than the measurements. Predicted values of $(\overline{u'^2_p})^{1/2}$ underestimate the measurements while $(\overline{v'^2_p})^{1/2}$ and $(\overline{w'^2_p})^{1/2}$ are in reasonably good agreement with measurements using the stochastic model. Since effects of swirl have decayed at this axial location, ignoring the anisotropy of the continuous phase is the main reason for this behavior. The particle mass flux predictions again highlight the different physical assumptions of the three models. Particle mass flux measurements indicated that between $x/d = 5$ and $x/d = 10$, the maximum mass flux shifted to the center of the jet for both swirl cases. Since angular

and radial velocities have decayed to relatively small values at this distance, and would tend to move particles outward, the only mechanism for transport inward is turbulent dispersion. As shown in figures 4.50 and 4.51, the predicted maximum particle flux from the stochastic separated flow model has not completely shifted to the center of the jet, however, it is clearly evolving in this direction. In contrast, the deterministic separated flow model predicts a very narrow distribution with no particles at the center of the jet. Compared to the nonswirling case, the locally homogeneous flow model underestimates particle dispersion for both swirling flows at $x/d = 20$. This behavior is caused by neglecting the angular inertia of the particles which tends to transport them radially.

Measurements and stochastic separated flow model predictions of mean axial velocities, for particle diameters of 23, 43, and 63 μm in the two swirling flows, are illustrated in figures 4.52 and 4.53. Radial profiles of $\overline{u}_p$ are shown at axial locations of $x/d = 2$, 5, 10, and 20. At $x/d = 2$, the velocity of the smaller particles is larger than the larger particles near the center of the jet. Due to their increased inertia, the axial velocities of the larger particles decay at a slower rate than smaller particles, and by $x/d = 20$, larger particles are moving at higher velocities than the smaller particles at all streamwise locations. Increasing swirl increases the variation of velocity with particle size, see figures 4.52 and 4.53.

Stochastic separated flow model predictions of mean particle axial velocity for each size group show better agreement with measurements as distance from the injector exist increases. At streamwise distances of $x/d = 10$ and less, radial profiles of axial velocity are overestimated for both swirling flows. As discussed earlier, this is probably due to turbulence modulation since the continuous-phase jet width was also overestimated for these flows, see figures 4.44 to 4.49. At $x/d = 5$, particle velocities are underestimated for both swirling flows. Since predicted centerline particle velocities were higher for the deterministic separated flow model at $x/d = 5$ and 10, this appears to be the result of eddy specification in the stochastic model. This is especially true for the 23 μm particles. Eddies are assumed to travel at the gas-phase velocity at their point of origination; therefore, the smaller particles, which have shorter relaxation times, tend to remain in a particular eddy longer than larger particles.

Predictions from the stochastic model display the correct trends with respect to changes of particle velocities with streamwise distance. Predictions at $x/d = 20$ exhibit good agreement with measurements for both swirling flows.

4.3 Sensitivity Study

Based upon the results of the present study, the stochastic separated flow model appears to be reasonably successful in treating weakly swirling, particle-laden jets. All predictions, however,

depend on the prescription of initial conditions and the empirical correlations for C_D. The sensitivity of the stochastic separated flow model to variations in various parameters is examined in the present section.

Nine key parameters were considered during the sensitivity study. The initial turbulence kinetic energy was considered since it could not be measured for the particle-laden jets and single-phase jet measurements were used instead. Similarly, ε_o was computed using k_o and a length scale based upon the jet width; therefore, effects of uncertainties of ε_o were also studied. Since the present flows were not monodisperse, d_p was also chosen as a variable in the sensitivity study. Standard particle drag empirical relations were adopted, thus, C_D was also considered. The eddy length scale, which was adopted from Gosman and Ioannides (66), as modified by Shuen (41), was also considered. Since initial particle radial and angular velocities were number averaged over all size groups, these were considered as well. For completeness, initial particle axial velocities were also considered. Finally, since gas-phase angular velocities could not be measured in the particle-laden jets, and were estimated by subtracting particle angular momentum from single-phase measurements, initial values of $\overline{w}$ were also considered during the sensitivity study.

Results of the sensitivity study are summarized in tables 4.1 and 4.2. The percent change in the computed output variable for a

Table 4.1 - Results of the Sensitivity Study at $x/d = 5$ for $S = 0.3$ Particle-Laden Swirling Jet[a]

Parameter	$\bar{u}_c$	$\frac{k_c}{\bar{u}_c^2}$	$\bar{w}_m$	$\bar{u}_{pm}$	$\bar{w}_{pm}$	G_m[b]
k_o	-0.8	2.5	-1.6	-1.8	-3.5	~0
ε_o	.3	-.6	.6	.8	3.2	-4
$\bar{w}_o$	-5.6	9.5	19.5	-10.0	4.5	~0
$\bar{u}_{po}$	~0	~0	-0.1	-2.8	1.2	~0
$\bar{w}_{po}$	~0	.2	1.1	-9.1	-5.6	8
$\bar{v}_{po}$	~0	~0	~.2	-10.4	-1.3	~0
C_D	.1	-.1	-.3	-.6	3.6	-17
d_p	.7	-2.5	-1.9	46.0	-6.6	-8
L_e	-.1	.3	-.6	3.3	.3	8

[a]Percent change in output variable for a 25 percent increase in input variable.
[b]Percent change in radial location of G_m.

Table 4.2 - Results of the Sensitivity Study at $x/d = 20$ for $S = 0.3$ Particle-Laden Swirling Jet[a]

Parameter	$\bar{u}_c$	$\frac{k_c}{\bar{u}_c^2}$	$\bar{u}_{pm}$	G_m[b]
k_o	-0.9	0.5	3.5	23
ε_o	0.3	-.1	3.6	-1
$\bar{w}_o$	-2	-1.6	-2.5	23
$\bar{u}_{po}$	~0	.1	2.9	22
$\bar{w}_{po}$	-.7	.8	1.2	1
$\bar{v}_{po}$	~0	-.2	3.0	22
C_D	.2	.5	2.8	0
d_p	3.5	-5.9	5.3	23
L_e	-.7	.4	-1.9	-44

[a]Percent change in output variable for a 25 percent increase in input variable.
[b]Percent change in radial location of G_m.

25 percent increase in the input variable are tabulated. The sensitivity study was conducted using the stochastic separated flow analysis. Baseline predictions were generated using initial conditions of the $S = 0.3$, particle-laden jet, with a single particle size of 39 microns.

At $x/d = 5$, see table 4.1, a 25 percent increase in any of the input parameters has a relatively small effect on all gas-phase predicted properties, except for $\overline{w}_o$. This is not surprising since jet structure is very sensitive to swirl number. Increasing $\overline{w}_o$ by 25 percent increases both the turbulence kinetic energy and maximum angular velocity. A 25 percent increase in $\overline{w}_o$ causes a 5 percent decrease in centerline axial velocity since the width of the jet is increased. Gas-phase predicted properties are not greatly influenced by initial particle parameters since this flow is relatively dilute.

Predictions of particle properties at $x/d = 5$ show a greater dependence on initial conditions than the continuous phase. As illustrated in table 4.1, increasing the particle diameter by 25 percent produces the largest effect on predictions of particle properties at $x/d = 5$. The increased particle diameter causes the predicted mean particle axial centerline velocity to increase by nearly 50 percent due to the increased inertia of the larger particles. Predictions of particle properties are less sensitive to initial values of particle angular and radial velocities. Increasing $\overline{w}_{po}$ causes the particles to move to larger radial locations where

they encounter reduced continuous-phase axial and angular velocities, tending to reduce particle velocities. Increasing $\overline{w}_{po}$ also causes an increase of the radial location of G_M. Increasing $\overline{v}_{po}$ also decreases particle velocities, however, G_M is not affected. Variations in the other parameters considered during the sensitivity study produced smaller changes in particle properties at $x/d = 5$, see table 4.1.

Table 4.2 presents the results of the sensitivity study at $x/d = 20$. For the baseline case considered, all velocities have decayed to relatively low values, especially the angular velocities of both phases, which are negligible at this streamwise location and are not reported. As expected, sensitivity of the predictions to changes in initial conditions is reduced at $x/d = 20$ compared to $x/d = 5$, with the exception of the radial location of G_M. At $x/d = 20$, the radial location of G_M is shifted toward the center of the jet, so that small variations in the predicted location show up as large percentage changes. It is evident from table 4.2 that the predictions show the largest sensitivity to the particle diameter but the increase in particle axial velocity is reduced to about 5 percent at $x/d = 20$. Predictions are less sensitive to the other parameters at $x/d = 20$.

For the weakly swirling particle-laden jet considered during the sensitivity study, the stochastic separated flow predictions are most sensitive to particle size. Predictions are less sensitive to initial values of $\overline{w}$, $\overline{w}_p$, and $\overline{v}_p$, although these parameters are still important. Predictions appeared relatively insensitive to the other parameters considered during the sensitivity study.

CHAPTER V

SUMMARY AND CONCLUSIONS

5.1 Summary

The overall objective of the present study was to investigate weakly swirling, particle-laden, turbulent jets. Measurements were emphasized, however, predictions were used to help interpret the measurements and to initiate evaluation of methods to estimate flow properties.

Experiments were initially conducted for three, single-phase jets having swirl numbers of 0, 0.19, and 0.33 to provide baseline data for the particle-laden jets. Measured flow properties for the single-phase jets included: mean and fluctuating axial and angular velocities, fluctuating radial velocity, turbulence kinetic energy,and Reynolds stress. A two-color LV system was used to measure velocities of the single-phase jets.

Experiments were also conducted for three particle-laden jets with swirl numbers of 0, 0.16, and 0.3. The particle size distribution had a SMD of 39 μm while a single mass loading ratio of 0.2 was used. For the continuous phase, mean and fluctuating axial velocities were measured with a single-channel phase/Doppler anemometer. For the particle phase, mean and fluctuating axial, radial, and angular velocities were measured using a two-color LV

system. Also for the particle phase, mean and fluctuating axial velocities for each particle size were measured using a single-channel phase/Doppler anemometer. Isokinetic sampling was used to measure particle mass flux distributions.

For the single-phase flows, governing equations for conservation of mass and momentum were solved using the finite-difference code, GENMIX (89). The equations were closed using a k-ε turbulence model which had been calibrated for constant and variable density, single-phase, round jets. Two modifications of the k-ε model, which attempt to account for effects of streamline curvature, were also evaluated.

Three two-phase flow models were evaluated for the particle-laden flows. They included: (1) a locally homogeneous flow (LHF) model, where interphase transport rates are assumed to be much faster than the rate of development of the flow as a whole; (2) a deterministic separated flow (DSF) model, which allows for finite interphase transport rates (evaluated using the mean properties of the continuous phase), but ignores interactions between the particles and turbulent fluctuations; and (3) a stochastic separated flow (SSF) model, where finite interphase transport rates and interactions of particles with turbulent eddies are considered using Monte-Carlo methods.

The governing equations for the continuous phase were based on the Favre-averaged conservation equations written in an Eulerian coordinate system. The dispersed phase was treated (for the separated

flow models) by solving Lagrangian equations-of-motion for the particles. A modified version of the GENMIX program (89), combined with a second-order Runge-Kutta ordinary differential equation solver for particle motion, was used to solve the governing equations.

5.2 Conclusions

The major observations and conclusions of the present study are as follows:

(1) For the weakly swirling free jets, increasing the swirl number increases the rate of mean axial and angular velocity decay with streamwise distance. Increasing the swirl number also increases the turbulence kinetic energy, the Reynolds stress, and the width of the swirling jets.

(2) For the single-phase, weakly swirling jets, a version of the $k-\varepsilon$ turbulence model, which was modified to include effects of streamline curvature, showed better agreement with measurements than the standard $k-\varepsilon$ turbulence model. This modification involved replacing one of the constants in the dissipation equation with a function of the flux Richardson number.

(3) Predictions using the stochastic separated flow model showed reasonable agreement with measurements for the nonswirling, particle-laden jets. In general, the locally homogeneous flow model overestimated both the rate of particle velocity decay and the rate of spread of particles in the nonswirling jet due to the neglect of particle inertia. The deterministic separated flow model

underestimated particle spreading rates due to the neglect of the effect of turbulent fluctuations on particle motion. Only the stochastic separated flow model, which accounts for both particle inertia and effects of turbulent fluctuations, correctly predicted particle spreading rates over the entire flowfield.

(4) Particle axial fluctuating velocities were generally underestimated at far downstream locations. This is probably due to the assumption of isotropic velocity fluctuations in the stochastic separated flow model, since fluctuating axial velocities are expected to be greater than fluctuating radial on angular velocities.

(5) Near the injector exit, jet widths were overestimated with the separated-flow models. This was probably caused by turbulence modulation by the particles, which was not considered in the analysis.

(6) Mean axial velocities for each particle size group were reasonably well predicted for the particle-laden jets using the stochastic separated flow model. Predictions showed the same trends as measurements for particle streamwise axial velocity decay of each size group.

REFERENCES

1. Rose, W.G., "A Swirling Round Turbulent Jet, 1-Mean-Flow Measurements," Trans. ASME, J. Appl. Mech., Vol. 29, 1962, pp. 615-625.
2. Pratt, D.B. and Keffer, J.F., "The Turbulent Swirling Jet," ASME J. Basic Engr., Vol. 94, 1972, pp. 739-748.
3. Mathur, M.L. and Mccallum, N.R.L., "Swirling Air Jets Issuing from Vane Swirlers, Part 1: Free Jets," J. Institute Fuel, Vol. 40, 1967, pp. 214-225.
4. Kerr, N.M. and Fraser, D., "Swirl. Part I: Effect on Axisymmetric Turbulent Jets," J. Institute Fuel, Vol. 38, 1965, pp. 519-526.
5. Sislian, J.P., and Cusworth, R.A., "Laser Doppler Velocimetry Measurements of Mean Velocity and Turbulent Stress Tensor Components in a Free Isothermal Swirling Jet," UTIAS, Report No. 281, 1984.
6. Chigier, N.A. and Beer, J.M., "Velocity and Static-Pressure Distributions in Swirling Air Jets Issuing from Annular and Divergent Nozzles," J. Basic Engr., Vol. 86, 1964, pp. 788-796.
7. Ribeiro, M.M. and Whitelaw, J.H., "Coaxial Jets With and Without Swirl," J. Fluid Mech., Vol. 96, 1980, pp. 769-795.
8. Craya, A. and Darrigol, M., "Turbulent Swirling Jet," Phys. Fluids Suppl., Vol. 10, 1967, pp. S197-S199.

9. Chigier, N.A. and Chervinsky, A., "Experimental Investigation of Swirling Vortex Motion in Jets," Trans. ASME J. Appl. Mech., Vol. 89, 1967, pp. 443-451.

10. Siddhartha, V., "Boundary Layers with Swirl," Ph.D. Thesis, Department of Mechanical Engineering, Imperial College of Science and Technology, London, 1971.

11. Morse, A.P., "Axisymmetric Free Shear Flows With and Without Swirl," Ph.D. Thesis, Department of Mechanical Engineering, Imperial College of Science and Technology, London, 1980.

12. Gouldin, F.C., Depsky, J.S., and Lee, S-L., "Velocity Field Characteristic of a Swirling Flow Combustor," AIAA J., Vol. 23, No. 1, 1985, pp. 95-102.

13. Kawaguchi, O., and Sato, G.T., "Experimental Investigation of Premixed Swirling Jet Flames," Bulletin JSME, Vol. 14, No. 11, 1971, pp. 248-255.

14. Murthy, S.N.B., "Survey of Some Aspects of Swirling Flows," ARL 71-0244, 1971.

15. Gupta, A.K., Lilley, D.G., and Syred, N., Swirl Flows, Abacus Press, Kent, 1984.

16. Lee, S-L., "Axisymmetric Turbulent Swirling Jet," ASME J. Appl. Mech., Vol. 32, 1965, pp. 258-262.

17. Rhode, D.L., Lilley, D.G., and McLaughlin, D.K., "Mean Flow Fields in Axisymmetric Combustor Geometries with Swirl," AIAA J., Vol. 21, No. 4, 1983, pp. 593-600.

18. Lilley, D.G., "Prediction of Inert Turbulent Swirl Flows," AIAA J., Vol. 11, No. 7, 1973, pp. 955-960.

19. Lilley, D.G. and Rhode, D.L., "A Computer Code for Swirling Turbulent Axisymmetric Recirculating Flows in Practical Isothermal Combustor Geometries," NASA CR-3442, 1982.

20. Kubo, I. and Gouldin, F.C., "Numerical Calculations of Turbulent Swirling Flow," J. Fluids Engr., 1975, pp. 310-315.

21. Leschziner, M.A., and Rodi, W., "Computation of Strongly Swirling Axisymmetric Free Jets," AIAA J., Vol. 22, No. 12, 1984, pp. 1742-1747.

22. Koosinlin, M.L. and Lockwood, F.C., "The Prediction of Axisymmetric Turbulent Swirling Boundary Layers," AIAA J., Vol. 12, No. 4, 1974, pp. 547-554.

23. Gibson, M.M., and Younis, B.A., "Calculation of Swirling Jets with a Reynolds Stress Closure," Phys. Fluids, Vol. 27, No. 1, 1986, pp. 38-48.

24. Lilley, D.G., "Swirl Flows in Combustion: A Review," AIAA J., Vol. 15, No. 8, 1977, pp. 1063-1078.

25. Syred, N. and Beer, J., "Combustion in Swirling Flows: A Review," Combustion and Flame, Vol. 23, 1974, pp. 143-201.

26. Chigier, N.A., "Gasdynamics of Swirling Flow in Combustion Systems," ACTA Astronautica, Vol. 17, 1972, pp. 387-395.

27. Soo, S.L., Fluid Dynamics of Multiphase Systems, Blaisdell Publishing Co., Waltham, 1967.

28. Hetsroni, G., Handbook of Multiphase Systems, Hemisphere Publishing Co., Washington, 1982.

29. Rudinger, G., Fundamentals of Gas-Particle Flow, Elsevier Scientific Publishing Co., New York, 1980.

30. Clift, R., Grace, J.R., and Weber, M.E., Bubbles, Drops, and Particles. Academic Press, New York, 1978.

31. Yuu, S., Yasukouchi, N., Hirosawa, Y., and Jotaki, T., "Particle Turbulent Diffusion in a Dust Laden Round Jet," AIChE J., Vol. 24, No. 3, 1978, pp. 509-519.

32. McComb, W.D., and Salih, S.M., "Comparison of Some Theoretical Concentration Profiles for Solid Particles in a Turbulent Jet With the Results of Measurements Using a Laser-Doppler Anemometer," J. Aerosol Sci., Vol. 9, 1978, pp. 299-313.

33. McComb, W.D., and Salih, S.M., "Measurement of Normalized Concentration Profiles in a Turbulent Aerosol Jet, Using a Laser-Doppler Anemometer," J. Aerosol Sci., Vol. 8. 1977, pp. 171-181.

34. Popper, J., Abuaf, N. and Hetsroni, G., "Velocity Measurements in a Two-Phase Turbulent Jet," Intl. J. Multiphase Flow, Vol. 1, 1974, pp. 715-726.

35. Levy Y., and Lockwood, F.C., "Velocity Measurements in a Particle Laden Turbulent Free Jet," Combustion and Flame, Vol. 40, 1981, pp. 333-339.

36. Modarress, D. Wuerer, J. and Elghobashi, S., "An Experimental Study of a Turbulent Round Two-Phase Jet," AIAA Paper No. 82-0964, 1982.

37. Modarress, D., Tan, H. and Elghobashi, S., "Two-Component LDA Measurements in a Two-Phase Turbulent Jet," AIAA J., Vol. 22, No. 5, May 1984, pp. 624-630.

38. Shuen, J.-S., Chen, L.-D., and Faeth, G.M., "Evaluation of a Stochastic Model of Particle Dispersion in a Turbulent Round Jet," AIChE J., Vol. 29, No. 1, 1983, pp. 167-170.

39. Shuen, J.-S., Chen, L.-D., and Faeth, G.M., "Prediction of the Structure of Turbulent, Particle-Laden Round Jets," AIAA J., Vol. 21, No. 11, 1983, pp. 1483-1484.

40. Shuen, J.-S., Solomon, A.S.P., Zhang, Q.-F., and Faeth, G.M.," Structure of Particle-Laden Jets: Measurements and Predictions," AIAA J., Vol. 23, No. 3, 1985, pp. 396-404.

41. Shuen, J.-S., "A Theoretical and Experimental Investigation of Dilute Particle-Laden Turbulent Gas Jets," Ph.D. Thesis, The Pennsylvania State University, University Park, PA., 1984.

42. Zhang, Q.-F., Shuen, J.-S., Solomon, A.S.P., and Faeth, G.M., "Structure of Ducted Particle-Laden Jets," AIAA J., Vol. 23, No. 7, 1985, pp. 1123-1125.

43. Solomon, A.S.P., Shuen J.-S., Zhang, Q.-F., and Faeth, G.M., "Structure of Nonevaporating Sprays: I. Near-Injector Conditions and Mean Properties," AIAA J., Vol. 23, No. 10, 1985, pp. 1548-1558.

44. Solomon, A.S.P., Shuen, J.-S., Zhang, Q.-F., and Faeth, G.M., "Structure of Nonevaporating Sprays: II. Drop and Turbulence Properties," AIAA J., Vol. 23, No. 11, 1985, pp. 1724-1730.

45. Solomon, A.S.P., Shuen, J.-S., Zhang, Q.-F., and Faeth, G.M., "Measurements and Predictions of the Structure of Evaporating Sprays," J. Heat Trans., Vol. 102, No. 3, 1985, pp. 679-686.

46. Shuen, S.-S., Solomon, A.S.P., and Faeth, G.M., "The Structure of Dilute Combusting Sprays," NASA CR-174838, 1985.

47. Shuen, J.-S., Solomon, A.S.P., and Faeth, G.M., "Drop-Turbulence Interactions in a Diffusion Flame," AIAA J., Vol. 24, No. 1, 1986, pp. 101-108.

48. During, R.P., and Suo M., "Particle Trajectories in Swirling Flows," J. Energy, Vol. 2, No. 4, 1978, pp. 232-287.

49. Domingos, J.J.D., and Roriz, L.F.C., "The Prediction of Trajectories of Evaporating or Burning Droplets," Proceedings of Fifth International Conference on Heat Transfer, Tokyo, Japan, Vol. 5, 1975, pp. 5-9.

50. Seleznev, L.I., and Tsvigan, S.T., "Investigation of the Influence of The Conditions of Swirling on the Structure of A Two-Phase Flow In an Expanding Channel," Translated from Izvestiya Akademii Nauk SSSR, Mekhanika Zhidkosti i Gaza, No. 5, 1983, pp. 85-90.

51. Hamed, A., "Particle Dynamics of Inlet Flow Fields With Swirling Vanes," AIAA Paper No. 81-0001, 1981.

52. Faeth, G.M., "Current Status of Droplet and Liquid Combustion," Prog. Energy Comb. Sci., Vol. 3, 1977, pp. 191-224.

53. Faeth, G.M., "Recent Advances in Modeling Particle Transport Properties and Dispersion in Turbulent Flows," Proceedings of the ASME-JSME Thermal Engineering Conference, Vol. 2, ASME, New York City, 1983, pp. 517-534.

54. Faeth, G.M., "Evaporation and Combustion of Sprays," Prog. Energy Comb. Sci., Vol. 9, 1983, pp. 1-76.

55. Shearer, A.J., and Faeth, G.M., "Evaluation of a Locally Homogeneous Model of Spray Evaporation," J. Energy, Vol. 3, No. 5, 1979, pp. 271-278.

56. Chen, L-D., and Faeth, G.M., "Structure of Turbulent Reacting Gas Jets Submerged in Liquid Metals," Comb. Sci. and Tech., Vol. 31, 1983, pp. 277-296.

57. Crowe, C.T., "Numerical Models for Dilute Gas-Particle Flows," J. Fluids Engr., Vol. 104, 1982, pp. 297-303.

58. Melville, W.K. and Bray, K.N., "A Model of the Two-Phase Turbulent Jet," Intl. J. Heat Mass Transfer, Vol. 22, 1979, pp. 647-656.

59. Sharma, M.P. and Crowe, C.T., "A Novel Physico-Computational Model for Quasi One-Dimensional Gas-Particle Flows," ASME Paper No. 76-WA/FE-36, 1976.

60. Jurewicz, J.T. and Stock, D.E., "A Numerical Model for Turbulent Diffusion in Gas-Particle Flows," ASME Paper No. 76-WA/FE-33, 1976.

61. Hutchinson, P., Hewitt, G.F., and Dukler, A.E., "Deposition of Liquid or Solid Dispersions from Turbulent Gas Streams: A Stochastic Model," Chem. Engr. Sci., Vol. 26, 1971, pp. 419-439.

62. Lee, N. and Dukler, A.E., "A Stochastic Model for Turbulent Diffusion of Particles or Drops," AIChE J., Vol. 27, No. 4, 1981, pp. 552-557.

63. Brown, D.J., and Hutchinson, P., "The Interaction of Solid or Liquid Particles and Turbulent Flow Fields--A Numerical Simulation," J. Fluids Engr., Vol. 101, 1979, pp. 265-269.

64. Peskin, R.L., and Kau, C.J., "Numerical Simulation of Particulate Motion in Turbulent Gas-Solid Channel Flow," J. Fluids Engr., Vol. 101, 1979, pp. 319-325.

65. Abbas, A.S., Koussa, S.S., and Lockwood, F.C., "The Prediction of the Particle Laden Gas Flows," Eighteenth Symposium (International) on Combustion, The Combustion Institute, Pittsburgh, 1981, pp. 1427-1438.

66. Gosman, A.D., and Ioannides, E., "Aspects of Computer Simulation of Liquid-Fueled Combustors," AIAA paper No. 81-0323, 1981.

67. Mostafa, A.A., and Mongia, H.C., "Eulerian and Lagrangian Predictions of Turbulent Evaporating Sprays," AIAA Paper No. 86-0452, 1986.

68. Dukowicz, J.K., "A Particle-Fluid Numerical Model for Liquid Sprays," J. Comp. Phys., Vol. 35, 1980, pp. 229-253.

69. Crowe, C.T., and Stock, D.E., "A Computer Solution for Two-Dimensional Fluid-Particle Flows," Intl. J. Num. Meth. Engr., Vol. 10, 1976, pp. 185-196.

70. Hutchinson, P. Khalil, E.E., and Whitelaw, J.H., "Measurement and Calculation of Furnace-Flow Properties," J. Energy, Vol. 1, No. 4, 1977, pp. 212-219.

71. Crowe, C.T., Sharma, M.P., and Stock, D.E., "The Particle-Source-in-Cell (PSI-Cell) Model for Gas-Droplet Flows," J. Fluids Engr., Vol. 99, 1977, pp. 325-332.

72. Weber, R., Boysan, F., Ayers, W.H., and Swithenbank, J., "Simulation of Dispersion of Heavy Particles in Confined Turbulent Flows," AIChE J., Vol. 30, No. 3, 1984, pp. 490-492.

73. ElBanhawy, Y. and Whitelaw, J.H., "Calculation of the Flow Properties of a Confined Kerosene-Spray Flame," AIAA J., Vol. 18, No. 12, 1980, pp. 1503-1510.

74. Launder, B.E., and Spalding, D.B., Lectures in Mathematical Models of Turbulence, Academic Press, London, 1972.

75. Kennedy, I.M., and Glass, M., "An Improved Seeding Method for High Temperature Laser Doppler Velocimetry," Combustion and Flame, Vol. 29, 1977, pp. 333-335.

76. Bachalo, W.D., and Houser, M.J., "Phase/Doppler Spray Analyzer for Simultaneous Measurements of Drop Size and Velocity Distributions," Optical Engr., Vol. 23, No. 5, 1984, pp. 583-590.

77. Houser, M.J., and Bachalo, W.D., "Extension of the Phase/Doppler Particle Analyzer to Submicron Particle Measurements," Proceedings of SPIE-International Society for Optical Engineering, Vol. 573, 1985, pp. 57-60.

78. Szekely, G.A., Jr., "Experimental Evaluation of a Carbon Slurry Droplet Combustion Model," Ph.D. Thesis, The Pennsylvania State University, University Park, PA, 1982.

79. Bilger, R.W., "Turbulent Flows with Nonpremixed Reactants," Turbulent Reacting Flows, Libby, P.A., and Williams, F.A., ed., Springer-Verlag, New York, 1980.

80. Bradshaw, P., Cebeci, T., and Whitelaw, J.H., Engineering Calculation Methods for Turbulent Flow, Academic Press, London 1981.

81. Jeng, S.-M., "An Investigation of Structure and Radiation Properties of Turbulent Buoyant Diffusion Flames," Ph.D. Thesis, The Pennsylvania State University, University Park, PA, 1983.

82. Bradshaw, P., "Effects of Streamline Curvature on Turbulent Flow," AGARDograph No. 169, 1973.

83. Sharma, B.I., "Computation of Flow Past a Rotating Cylinder with an Energy-Dissipation Model of Turbulence," AIAA J., Vol. 15, No. 2, 1977, pp. 271-274.

84. Leschziner, M.A., and Rodi, W., "Computation of Strongly Swirling Axisymmetric Free Jets," AIAA J., Vol. 22, No. 12, 1984, pp. 1742-1747.

85. Hah, C., and Lakshminarayana, B., "Prediction of Two- and Three-Dimensional Asymmetrical Turbulent Wakes, Including Curvature and Rotation Effects," AIAA J., Vol. 18, No. 10, 1980, pp. 1196-1204.

86. Leschziner, M.A., and Rodi, W., "Calculations of Annular and Twin Parallel Jets Using Various Discretization Schemes and Turbulence-Model Variations," J. Fluids Engr., Vol. 103, 1981, pp. 352-360.

87. Komori, S., and Ueda, H., "Turbulent Flow Structure in the Near Field of a Swirling Round Free Jet," Phys. Fluids, Vol. 28, No. 7, 1985, pp. 2075-2082.

88. Lakshminarayana, B., "Turbulence Modeling for Complex Shear Flows," AIAA J., Vol. 24, No. 12, 1986, pp. 1900-1917.

89. Spalding, D.B., GENMIX: A General Computer Program for Two-Dimensional Parabolic Phenomena, Pergamon Press, Oxford, 1978.

90. Al Taweel, A.M., and Landau, J., "Turbulence Modulation in Two-Phase Jets," Intl. J. Multiphase Flow, Vol. 3, 1977, pp. 341-351.

91. Mostafa, A.A., and Elghobashi, S.E., "Effect of Liquid Droplets on Turbulence in a Round Gaseous Jet," NASA CR-175063, 1986.

92. Mostafa, A.A., and Mongia, H.C., "On the Turbulence-Particles Interaction in Turbulent Two-Phase Flows," AIAA Paper No. 86-0215, 1986.

93. Durst, F., Melling, A., and Whitelaw, J.H., Principles and Practice of Laser-Doppler Anemometry, Academic Press, London, 1976.

94. McLaughlin, D.K., and Tiederman, W.G., "Biasing Correction for Individual Realization of Laser Anemometer Measurements in Turbulent Flows," Phys. Fluids, Vol. 16, No. 12, 1973, pp. 2082-2088.

95. Craig, R.R., Nejad, A.S., Hahn, E.Y., and Schwartzkopf, K.G., "Approach for Obtaining Unbiased Laser Doppler Velocimeter Data in Highly Turbulent Flows," J. Propulsion Power, Vol. 2, No. 6, 1986, pp. 541-545.

96. Buchave, P., George, W.K., Jr., and Lumley, J.L., "The Measurement of Turbulence with the Laser-Doppler Anemometer," Ann. Rev. Fluid Mech., Vol. 11, 1979, pp. 443-503.

97. Stevenson, W.H., Thompson, H.D., and Roessler, T.C., "Direct Measurement of Laser Velocimeter Bias Errors in a Turbulent Flow," AIAA J., Vol. 20, No. 12, 1982, pp. 1720-1723.

98. Kreid, D.K., "Laser-Doppler Velocimeter Measurements in Nonuniform Flow: Error Estimates," J. Appl. Optics, Vol. 13, No. 8, 1974, pp. 1872-1881.

99. Kline, S.J., and McClintock, F.A., "Describing Uncertainties in Single-Sample Experiments," Mech. Energy., Vol. 75, 1953, pp. 3-8.

100. Moffat, R.J., "Contributions to the Theory of Single-Sample Uncertainty Analysis," J. Fluids Engr., Vol. 104, 1982, pp. 250-258.

APPENDIX A

EXPERIMENTAL UNCERTAINTIES

A.1 Bias Errors

A.1.1 Single-Phase Jet Velocities

Bias errors in velocity determinations using LV arise from several sources, as follows (93): (1) directional ambiguity, due to the inability of a stationary or slowly translating fringe pattern to provide an indication of the direction in which particles are crossing the fringes; (2) directional bias, due to particles crossing the measuring volume at a small angle with respect to the plane of the fringes so that an insufficient number of fringes are crossed to be processed; (3) concentration bias, due to varying particle concentrations in the flowfield; (4) velocity bias, due to the fact that for a uniformly seeded flowfield, more particles having a higher velocity are measured than those having a lower velocity; and (5) gradient bias, due to variations in flow velocity in the measuring volume. Each of these possible sources of biasing are discussed in the following.

The present measurements in single-phase jets employed frequency shifting for both channels to eliminate errors due to directional ambiguity. Effective shifting levels were set at each location so that maximum negative velocities could be detected. For axial velocity measurements, effective shifting levels, of 0.5 and 1 MHz were used. For radial and angular velocity measurements, effective

frequency shifting levels of 2 and 5 MHz were used. Use of frequency shifting also minimized directional biasing.

Concentration bias was not a factor during the present experiments since both the jet and ambient surroundings were seeded.

Velocity bias can be a factor in highly turbulent flows when particle averages are used. Various techniques have been suggested (93 to 97) to minimize this effect. The approach taken during the present measurements was to operate the counters in the total burst mode and apply a weighing factor to the measurement based upon the measured time of the doppler burst. This approach was suggested by Buchave and George (93) and found to give reasonably good results. For the present measurements, time averaged values were calculated as follows:

$$\bar{u} = \frac{\sum_i u_i \tau_{ui}}{\sum_i \tau_{ui}} \tag{A.1}$$

$$(\bar{u}_i^2)^{1/2} = \left[\frac{\sum_i u_i^2 \tau_{ui}}{\sum_i \tau_{ui}} - \bar{u}^2 \right]^{1/2} \tag{A.2}$$

where τ_{ui} is the measured time of the ith doppler burst. Time averaged values of mean and fluctuating, radial and angular velocities are calculated in a similar manner. For Reynolds stress, time averaged values were calculated as follows:

$$\overline{u'v'} = \frac{\sum_i u_i v_i \tau_{uvi}}{\sum_i \tau_{uvi}} - \bar{u} \frac{\sum_i v_i \tau_{uvi}}{\sum_i \tau_{uvi}} - \bar{v} \frac{\sum_i u_i \tau_{uvi}}{\sum_i \tau_{uvi}} + (\bar{u}\bar{v}) \qquad (A.3)$$

where τ_{uvi} is the smaller of the two measured doppler burst times from the two counters measuring u and v.

The final source of biasing considered is gradient biasing. This bias can be estimated using the analysis reported by Kreid (98). For this analysis, only velocity gradients in the radial direction are considered and all seeding particles crossing the measuring volume are assumed to be recorded, so that higher-order terms in the Taylor series expansion of mean velocity (expanded from the center of the measuring volume) can be ignored. The difference between the actual velocities, $\bar{u}$ and $\bar{u}'$, and the measured values, $\bar{u}_t$ and $\bar{u}_t'$, can then be estimated as follows:

$$|\bar{u}_t - \bar{u}| \approx \frac{\ell^2}{6} \frac{\partial^2 \bar{u}}{\partial r^2} \qquad (A.4)$$

$$|\bar{u}_t'^2 - \bar{u}'^2| \approx \frac{\ell^2}{3} \left(\frac{\partial \bar{u}}{\partial r}\right)^2 \qquad (A.5)$$

where ℓ is the half-width of the measuring volume in the radial direction.

Maximum gradient biasing occurred at $x/d = 0.5$ for the flows considered here. Using the depth of field limit for measuring volume length, the estimated gradient biasing error was less than 0.1 percent for mean values and approximately 0.5 percent for fluctuating values. If the depth of field limit for probe volume length is not applied,

gradient bias errors are larger, however, and at the same location, they are estimated to be less than 1 percent for mean values and approximately 30 percent for fluctuating values. These are maximum values, and are only found in a small radial region at $x/d = 0.5$: the majority of errors are considerably smaller at other locations in the flow.

A.1.2 Particle-Laden Jet Velocities

A.1.2.1 Dispersed-phase velocities - Biasing errors for LV measurements of particle velocities are similar to single-phase velocity measurements.

Frequency shifting was used to eliminate errors due to directional ambiguity and to minimize errors due to directional bias.

Velocity bias was not a factor in these measurements because number-averaged velocities are desired for comparison with theory. For particle velocity measurements, the counters were operated in the total burst mode but no residence time weighting factor was included so that number averages were obtained.

Gradient biasing was the greatest potential source of bias error for particle velocity measurements. For these measurements, grazing encounters with the measuring volume are recorded as valid measurements so that the dimensions of the measuring volume were increased by the diameter of the largest particles in the flow. Equations (A.4) and (A.5) were used to estimate gradient bias errors. Maximum bias errors are found at $x/d = 0.5$. For the worst case

considered, particle velocities are biased less than 0.1 percent for mean values and less than 2 percent for fluctuating values. At other positions in the flow, biasing errors for fluctuating values are reduced to less than 1 percent. Therefore, gradient biasing errors are small in comparison to other uncertainties of the particle velocity measurements.

A.1.2.2 Continuous-phase velocities - Biasing errors for LV measurements of continuous phase velocity are similar to those previously discussed. The instrument used to measure continuous phase velocities simultaneously measured both particle size and velocity. Because frequency shifting was not available for this instrument, only mean and fluctuating axial velocities were measured in order to minimize directional bias. To further minimize directional bias, axial velocity measurements were not attempted in regions of the flow near the edge of the jet where negative velocities may be found due to the low mean values of axial velocity.

Velocity bias may influence measurements of continuous-phase velocity, especially in highly turbulent regions. The processor considered the entire Doppler burst and mean and fluctuating axial velocities were calculated from number-averaged velocities for each particle size group. As discussed in (93, 94, 96), for flows with turbulence intensities above approximately 30 percent, velocity bias can be an important source of error in measurements. For the present

measurements, regions near the edge of the jet where turbulence intensities are quite high were avoided in order to minimize velocity bias effects.

Gradient biasing errors for continuous-phase measurements are similar to those previously discussed and were estimated using equations (A.4) and (A.5). Maximum biasing occurred at $x/d = 0.5$ where gradient bias errors were estimated to be on the order of 0.1 percent for mean values and 1 percent for fluctuating values. It can be concluded that gradient bias was negligible for the present measurements.

A.1.3. Particle Mass Flux Measurements

Particle mass flux measurements were obtained by collecting particles using an isokinetic sampling probe for a timed interval and weighing. In order to insure reasonable sampling times and adequate resolution, probes with inside diameters of 2 and 5 mm were used. Because of the relatively large diameter of the probe, errors due to particle gradients in the radial direction are the major sources of bias errors. Similar to the analysis for gradient bias in velocity measurements, the gradient bias error in particle mass flux measurements can be estimated as follows:

$$|\bar{G}_t - \bar{G}| \approx \frac{\left(\frac{d}{2}\right)^2}{6} \frac{\partial^2 \bar{G}}{\partial r^2} \qquad (A.6)$$

where d is the inside diameter of the probe. Gradients are highest at $x/d = 0.5$ where the maximum gradient bias was estimated to be on the order of 2 percent.

A.2 Uncertainty Estimates

A.2.1 General Formulation

The uncertainty analysis described by Kline and McClintock (99) and Moffat (100) was adopted to estimate experimental uncertainties for the present measurements. An output variable, R, is considered, which is a function of n measured variables, X_i, as follows:

$$R = R(X_1, X_2, X_3, \ldots X_n) \tag{A.7}$$

The X_i are subject to uncertainties, δx_i, and the resulting uncertainty in R, e.g., δR, is to be determined. The δX_i and δR can be defined as the expected standard deviation of these quantities as some percentage of the confidence interval of these quantities, e.g., the 95 percent confidence interval is most frequently chosen (100) and is used here as well. The relative uncertainty can be expressed as follows:

$$\frac{\delta R}{R} = \left[\frac{\partial R}{\partial X_1}\left(\frac{\partial X_1}{R}\right)^2 + \frac{\partial R}{\partial X_2}\left(\frac{\partial X_2}{R}\right)^2 + \cdots \frac{\partial R}{\partial X_n}\left(\frac{\partial X_n}{R}\right)^2 \right]^{1/2} \tag{A.8}$$

Equation (A.8) will be used to estimate relative uncertainties in the following.

A.2.2 Mean and Turbulent Continuous-Phase Velocities

A.2.2.1 Single-phase jet measurements - In considering uncertainties in continuous-phase velocity measurements, positioning

errors are ignored since this only influences the position at which data points are located and this accuracy has been given previously. The mean velocity measurement then depends on the overall calibration factor, K, between the averaged electrical signal, E, from the counter and velocity. The electrical signal, E, is averaged over all Doppler bursts considered. This can be expressed as follows:

$$\tilde{u} = \tilde{K}\tilde{E}_x \tag{A.9}$$

Applying equations (A.8) to (A.9) yields:

$$\frac{\partial \tilde{u}}{\tilde{u}} = \left[\left(\frac{\delta K}{K} \right)^2 + \left(\frac{\delta \tilde{E}_x}{\tilde{E}_x} \right)^2 \right]^{1/2} \tag{A.10}$$

The overall calibration factor, K, was verified using a rotating disc. The uncertainty of E was estimated from actual measurements at various locations in the flowfield using standard operating procedures. The uncertainty is estimated as two times the standard deviation found in these measurements (~95 percent confidence interval). Substituting the appropriate estimates into equation (A.10) then yields an uncertainty for mean axial velocities of 5 percent. Uncertainties of mean angular velocity measurements can be quite high since values of $\tilde{w}$ decrease to zero at the centerline and near the edge of the jet. In addition, peak values of $\tilde{w}$ are smaller than $\tilde{u}$ and $\tilde{w}$ decays rapidly with axial distance. Using equation (A.10) for $\tilde{w}$ at $x/d = 10$ yields an uncertainty for mean angular velocity of 20 percent. Uncertainties in $\tilde{w}$ are smaller closer to

the injector exit, since $\tilde{w}$ is larger while uncertainties farther downstream are larger because $\tilde{w}$ is smaller.

The uncertainties in velocity fluctuations were also estimated for the single-phase flows. For this case $\tilde{e}_i$ represents the fluctuating electrical signal from the doppler bursts and fluctuating axial velocity can be expressed as follows:

$$\tilde{u}' = K\tilde{e}_x \tag{A.11}$$

Applying equation (A.8) yields

$$\frac{\delta\tilde{u}'}{\tilde{u}'} = \left[\left(\frac{\delta K}{K}\right)^2 + \left(\frac{\delta\tilde{e}_x}{\tilde{e}_x}\right)^2\right]^{1/2} \tag{A.12}$$

Equations for $\tilde{v}'$ and $\tilde{w}'$ are similar. Using representative standard deviations in measurements of fluctuating quantities throughout the flowfield yields uncertainties for $\tilde{u}$, $\tilde{v}'$, and $\tilde{w}'$ of less than 5 percent.

Uncertainties in quadratic quantities, such as k and $u'v'$, are larger. For k, we have:

$$k = \frac{1}{2} K^2 (\tilde{e}_x^2 + \tilde{e}_r^2 + \tilde{e}_\theta^2) \tag{A.13}$$

Assuming $\tilde{e}_x \simeq \tilde{e}_r \simeq \tilde{e}_\theta$, and applying equation (A.8) yields:

$$\frac{\delta k}{k} = \left[2\left(\frac{\delta K}{K}\right)^2 + 2\left(\frac{\delta\tilde{e}}{\tilde{e}}\right)^2\right]^{1/2} \tag{A.14}$$

Substituting appropriate estimates into equation (A.14) yields an uncertainty estimate of 12 percent for k.

For Reynolds stress, we have:

$$\widetilde{u}'\widetilde{v}' = K^2 \tilde{e}_x \tilde{e}_r$$

Applying equation (A.8) yields

$$\frac{\delta \widetilde{u}'\widetilde{v}'}{\widetilde{u}'\widetilde{v}'} = \left[\left(\frac{2\delta K}{K} \right)^2 + \left(\frac{\delta \tilde{e}_x \tilde{e}_r}{\tilde{e}_x \tilde{e}_r} \right)^2 \right]^{1/2} \qquad \text{(A.15)}$$

Obviously, similar to $\widetilde{w}$, in regions where $\widetilde{u}'\widetilde{v}'$ is small, (near the axis and edge of the jet) the uncertainty can be very large. A more representative condition is the region near the peak of maximum Reynolds stress. Substituting these values into equation (A.15) yields an uncertainty of 14 percent for peak values of $\widetilde{u}'\widetilde{v}'$.

A.2.2.2 Particle-Laden Jet Measurements - Uncertainties of mean and fluctuating axial velocities of the continuous phase for the particle-laden flows were calculated from equations (A.10) and (A.12). Uncertainties are estimated to be less than 4 percent for $\widetilde{u}$ and less than 5 percent for $\widetilde{u}'$. These are identical to the estimated uncertainties for the single-phase flows.

A.2.3. Dispersed-Phase Velocities

Uncertainties of measured mean and fluctuating particle velocities were calculated from equations (A.10) and (A.12). The estimated uncertainty of $\widetilde{u}_p$ was less than 5 percent. The estimated uncertainty in $\widetilde{v}_p$ was 10 percent at $x/d = 0.5$, which is larger than $\widetilde{u}_p$ because $\widetilde{v}_p$ is smaller. The estimated uncertainty in $\widetilde{w}_p$ at $x/d = 0.5$ is 6 percent near the maximum value of $\widetilde{w}_p$, however, for the same reasons as previously discussed

for other measurements of angular velocity, uncertainties in $\tilde{w}_p$ can be nearly 20 percent since $\tilde{w}_p$ varies considerably throughout the flowfield. For fluctuating particle velocities, uncertainties are estimated to be less than 5 percent.

A.2.4. Particle Mass Flux Measurements

Particle mass flux was determined from the following equation:

$$G = \frac{4}{\pi} \frac{\dot{m}_p}{d^2} \tag{A.16}$$

Applying equation (A.8) to equation (A.16) yields:

$$\frac{\delta G}{G} = \left[\left(\frac{\delta \dot{m}_p}{\dot{m}_p} \right)^2 + \left(\frac{2\delta d}{d} \right)^2 \right]^{1/2} \tag{A.17}$$

Substituting estimated uncertainties of probe diameter and mass flowrate into equation (A.17) yields an uncertainty estimate of less than 8 percent for particle mass-flux measurements.

APPENDIX B

DESCRIPTION OF THE GENMIX ALGORITHM

A general purpose computer code, GENMIX, described by Spalding (89) for boundary-layer flows, was used to solve the governing equations. This code is very convenient for the calculation of free jets since it utilizes a dimensionless stream function formulation that automatically expands the cross-stream grid width as the calculation proceeds downstream. The dimensionless stream condition is defined as follows:

$$\omega = \frac{\left(\psi - \psi_I\right)}{\left(\psi_E - \psi_I\right)} \tag{B.1}$$

where ψ_I and ψ_E are the values of the stream function at the inner and external boundaries of the flow.

The stream function is defind as:

$$\frac{\partial \psi}{\partial x} = - r\bar{\rho}\tilde{v} \tag{B.2}$$

and

$$\frac{\partial \psi}{\partial r} = + r\bar{\rho}\tilde{u} \tag{B.3}$$

The use of the stream function automatically satisfies the conservation of mass equation. At the inner and external boundaries the stream function can be expressed as:

$$\frac{\partial \psi_I}{\partial x} = - r_I \dot{m}_I'' \tag{B.4}$$

$$\frac{\partial \psi_E}{\partial x} = - r_E \dot{m}_E'' \tag{B.5}$$

where $\dot{m}_I''$ and $\dot{m}_E''$ are the mass transfer rates across the inner and external boundaries.

Using these transformations, equation (3.2) can be transformed to the following general form:

$$\frac{\partial \varphi}{\partial x} + (A_1 + A_2 \omega) \frac{\partial \varphi}{\partial \omega} = \frac{\partial}{\partial \omega} \left(A_3 \frac{\partial \varphi}{\partial \omega} + A_4 \right) \tag{B.6}$$

where φ represents $\tilde{u}$, $\tilde{f}$, k and ε. The other terms in equation (B.6) are defined in table B.1. For $\varphi = r\tilde{w}$, equation (B.1) can be rearranged to eliminate the source term and can be written as follows:

$$\frac{\partial (r\tilde{w})}{\partial x} + (A_1 + A_2 \omega) \frac{\partial (r\tilde{w})}{\partial \omega} = \frac{\partial}{\partial \omega} \; A_3 r^2 \left(\frac{\partial \frac{\tilde{w}}{r}}{\partial \omega} \right) \tag{B.7}$$

where A_1, A_2 and A_3 are also defined in table B.1. This set of equations was integrated from an upstream initial condition to a value of x equal to 30 diameters, for values of ω ranging from zero to one.

The present calculations were performed using 33 cross-stream nodes. The cross stream grid spacing included the entire flow width. The forward marching step was limited so that the quantity of fluid entrainment during the mixing step is a certain fraction of the total fluid in the flow to that position in the flow.

$$x = \frac{\left(\psi_E - \psi_I \right)}{r_I \dot{m}_I'' - r_E \dot{m}_E''} \tag{B.8}$$

Table B.1. - Definition of Terms in the Generalized GENMIX Program

$$A_1 = r_I \dot{m}_I'' / (\psi_E - \psi_I)$$

$$A_2 = (r_E \dot{m}_E'' - r_I \dot{m}_I'') / (\psi_E - \psi_I)$$

$$A_3 = r^2 \tilde{\bar{\rho}}\tilde{u}\mu_t / (\psi_E - \psi_I)^2 \sigma_\phi$$

ϕ	A_4
$\tilde{u}$	$-\frac{1}{\tilde{\bar{\rho}}\tilde{u}} \frac{\partial \bar{p}}{\partial x}$
$\tilde{f}$	0
k	$\frac{1}{\tilde{\bar{\rho}}\tilde{u}} \left\{ \mu_t \left(\frac{\partial \tilde{u}}{\partial r} \right)^2 + \left[r \frac{\partial}{\partial r} \left(\frac{\tilde{w}}{r} \right) \right]^2 - \bar{\rho}\varepsilon \right\}$
ε	$\frac{1}{\tilde{\bar{\rho}}\tilde{u}} \left\{ C_{\varepsilon_1} \mu_t \frac{\varepsilon}{k} \left(\frac{\partial \tilde{u}}{\partial r} \right)^2 + \left[r \frac{\partial}{\partial r} \left(\frac{\tilde{w}}{r} \right) \right]^2 - C_{\varepsilon_2} \bar{\rho} \frac{\varepsilon^2}{k} \right\}$

In the present calculations, the forward step size was limited so that the ratio of entrainment to the total fluid in the flow was 0.05 for the nonswirling flows and 0.02 for the swirling flows. The ratio was set as low as 0.005 without significant difference in the results. Forward step size was also constrained to be less than 5 percent of the current flow width for the nonswirling flows and 2 percent for the flows with swirl.

APPENDIX C

SUMMARY OF DATA

C.1 Single-Phase Jets

C.1.1 Single-Phase Jet, S = 0

Table C.1 - Single-Phase Jet at x/d = 0.5, S = 0[a]

$\frac{r}{x}$	$\frac{\bar{u}}{\bar{u}_c}$	$\frac{(\overline{u'^2})^{1/2}}{\bar{u}_c}$	$\frac{(\overline{v'^2})^{1/2}}{\bar{u}_c}$	$\frac{k}{\bar{u}_c^2} \times 10^1$	$\frac{\overline{u'v'}}{\bar{u}_c^2} \times 10^2$
0	1.0	0.053	0.039	0.029	0.008
.121	.997	.045	.039	.026	.022
.279	.972	.056	.049	.040	.039
.321	.962	.058	.040	.033	.084
.479	.917	.069	.043	.042	.097
.521	.905	.074	.045	.048	.120
.679	.848	.077	.048	.052	.160
.721	.827	.078	.052	.058	.170
.879	.721	.116	.067	.112	.337
.923	.663	.127	.080	.144	.480
1.017	.464	.159	.100	.227	.874
1.079	.256	.141	.118	.239	1.027
1.120	.193	.115	.113	.193	.700
1.175	.106	.086	.103	.144	.468
1.180	.099	.085	.101	.137	.478

[a] $\bar{u}_c$ = 14.86 m/s.

Table C.2 - Single-Phase Jet at x/d = 15, S = 0[a]

$\frac{r}{x}$	$\frac{\bar{u}}{\bar{u}_c}$	$\frac{(\overline{u'^2})^{1/2}}{\bar{u}_c}$	$\frac{(\overline{v'^2})^{1/2}}{\bar{u}_c}$	$\frac{(\overline{w'^2})^{1/2}}{\bar{u}_c}$	$\frac{k}{\bar{u}_c^2} \times 10^1$	$\frac{\overline{u'v'}}{\bar{u}_c^2} \times 10^2$
0	1.0	0.209	0.165	0.165	0.489	0.021
.02	.964	.212	.166	.169	.504	.523
.04	.843	.214	.165	.177	.521	1.068
.06	.684	.212	.162	.177	.513	1.283
.08	.529	.197	.169	.182	.501	1.310
.10	.374	.164	.148	.159	.370	.971
.12	.257	.142	.130	.134	.276	.676
.14	.172	.112	.120	.137	.229	.515
.16	.106	.086	.108	.093	.138	.338
.18	.061	.059	.093	.067	.083	.238

[a] $\bar{u}_c$ = 6.77 m/s.

Table C.3 - Single-Phase Jet at x/d = 30, S = 0[a]

$\frac{r}{x}$	$\frac{\bar{u}}{\bar{u}_c}$	$\frac{(\overline{u'^2})^{1/2}}{\bar{u}_c}$	$\frac{(\overline{v'^2})^{1/2}}{\bar{u}_c}$	$\frac{(\overline{w'^2})^{1/2}}{\bar{u}_c}$	$\frac{k}{\bar{u}_c^2} \times 10^1$	$\frac{\overline{u'v'}}{\bar{u}_c^2} \times 10^2$
0	1.0	0.244	0.210	0.210	0.737	0.012
.02	.964	.254	.232	.224	.841	.937
.04	.863	.247	.217	.224	.790	1.004
.06	.741	.241	.228	.221	.795	1.380
.08	.582	.231	.223	.243	.813	1.695
.10	.439	.204	.206	.206	.633	1.520
.12	.314	.179	.188	.168	.478	1.340
.14	.222	.141	.168	.147	.348	.941
.16	.120	.107	.146	.122	.239	.448

[a] $\bar{u}_c$ = 3.03 m/s.

C.1.2 Single-Phase Jet, S = 0.19

Table C.4 - Single-Phase Jet at x/d = 0.5, S = 0.19[a]

$\frac{r}{x}$	$\frac{\bar{u}}{\bar{u}_c}$	$\frac{(\overline{u'^2})^{1/2}}{\bar{u}_c}$	$\frac{(\overline{v'^2})^{1/2}}{\bar{u}_c}$	$\frac{(\overline{w'^2})^{1/2}}{\bar{u}_c}$	$\frac{\bar{w}}{\bar{w}_m}$	$\frac{k}{\bar{u}_c^2} \times 10^1$	$\frac{\overline{u'v'}}{\bar{u}_c^2} \times 10^2$
0	1.0	0.082	0.149	0.149	0.046	0.257	0.018
.1	.991	.088	.146	.143	.237	.247	.029
.2	.983	.087	.153	.124	.500	.232	.056
.3	.976	.087	.148	.109	.632	.208	.087
.4	.965	.087	.139	.092	.742	.176	.121
.5	.951	.087	.137	.088	.814	.171	.139
.6	.937	.088	.114	.091	.856	.145	.177
.7	.911	.096	.109	.097	.907	.152	.335
.8	.878	.119	.107	.100	.948	.178	.500
.9	.811	.158	.117	.108	1.0	.253	.875
1.0	.672	.207	.139	.135	.876	.401	1.430
1.1	.476	.221	.171	.148	.638	.499	1.850
1.2	.234	.167	.154	.136	.393	.351	1.230
1.3	.109	.102	.125	.092	.136	.172	.500

[a] $\bar{u}_c$ = 12.94 m/s, $\bar{w}_m$ = 3.158 m/s.

Table C.5 - Single-Phase Jet at x/d = 2, S = 0.19[a]

$\frac{r}{x}$	$\frac{\bar{u}}{\bar{u}_c}$	$\frac{(\overline{u'^2})^{1/2}}{\bar{u}_c}$	$\frac{(\overline{v'^2})^{1/2}}{\bar{u}_c}$	$\frac{(\overline{w'^2})^{1/2}}{\bar{u}_c}$	$\frac{\bar{w}}{\bar{w}_m}$	$\frac{k}{\bar{u}_c^2} \times 10^1$	$\frac{\overline{u'v'}}{\bar{u}_c^2} \times 10^2$
0	1.0	0.126	0.155	0.155	0.062	0.319	0.034
.033	.989	.138	.157	.155	.476	.337	.173
.067	.968	.156	.172	.153	.756	.387	.555
.100	.935	.171	.183	.149	1.00	.423	.785
.134	.897	.187	.169	.155	.990	.438	.795
.184	.815	.211	.170	.173	.938	.516	1.370
.234	.729	.219	.167	.179	.816	.541	1.680
.284	.595	.223	.177	.179	.720	.565	1.780
.334	.457	.207	.194	.176	.707	.557	1.980
.384	.319	.186	.187	.161	.623	.477	1.660
.434	.215	.157	.174	.147	.539	.382	1.290
.485	.131	.118	.163	.115	.272	.268	.910
.535	.089	.091	.138	.077	.110	.166	.680

[a] $\bar{u}_c$ = 11.729 m/s, $\bar{w}_m$ = 1.920 m/s.

Table C.6 - Single-Phase Jet at x/d = 5, S = 0.19[a]

$\frac{r}{x}$	$\frac{\bar{u}}{\bar{u}_c}$	$\frac{(\overline{u'^2})^{1/2}}{\bar{u}_c}$	$\frac{(\overline{v'^2})^{1/2}}{\bar{u}_c}$	$\frac{(\overline{w'^2})^{1/2}}{\bar{u}_c}$	$\frac{\bar{w}}{\bar{w}_m}$	$\frac{k}{\bar{u}_c^2} \times 10^1$	$\frac{\overline{u'v'}}{\bar{u}_c^2} \times 10^2$
0	1.0	0.251	0.219	0.219	0.045	0.793	0.160
.027	.974	.254	.220	.220	.078	.807	.375
.053	.940	.263	.221	.220	.156	.832	1.02
.080	.883	.270	.225	.226	.204	.872	1.76
.107	.819	.276	.225	.236	.205	.913	1.85
.134	.717	.273	.235	.222	.368	.894	2.70
.160	.626	.271	.223	.221	.660	.860	2.08
.187	.531	.253	.235	.217	.663	.830	2.10
.214	.428	.235	.227	.210	.810	.754	1.96
.241	.336	.217	.209	.184	1.0	.622	1.77
.267	.259	.192	.203	.197	.761	.585	1.55
.294	.189	.168	.210	.174	.562	.514	1.77
.321	.138	.148	.200	.158	.537	.434	1.48

[a] $\bar{u}_c$ = 7.881 m/s, $\bar{w}_m$ = 0.866 m/s.

Table C.7 - Single-Phase Jet at x/d = 10, S = 0.19[a]

$\frac{r}{x}$	$\frac{\bar{u}}{\bar{u}_c}$	$\frac{(\overline{u'^2})^{1/2}}{\bar{u}_c}$	$\frac{(\overline{v'^2})^{1/2}}{\bar{u}_c}$	$\frac{(\overline{w'^2})^{1/2}}{\bar{u}_c}$	$\frac{\bar{w}}{\bar{w}_m}$	$\frac{k}{\bar{u}_c^2} \times 10^1$	$\frac{\overline{u'v'}}{\bar{u}_c^2} \times 10^2$
0	1.0	0.263	0.240	0.240	0.090	0.921	0.160
.027	.982	.276	.249	.242	.092	.984	.81
.053	.926	.284	.243	.241	.249	.990	1.12
.080	.818	.274	.248	.257	.552	1.011	1.48
.107	.716	.268	.237	.247	.514	.947	1.73
.134	.609	.261	.221	.221	.730	.831	2.21
.160	.489	.240	.212	.218	.735	.752	1.94
.187	.382	.211	.199	.191	1.00	.604	1.50
.214	.289	.183	.184	.170	.849	.482	1.32
.241	.210	.161	.155	.160	.415	.377	1.03
.267	.155	.138	.149	.120	.121	.279	.07

[a] $\bar{u}_c$ = 4.751 m/s, $\bar{w}_m$ = 0.422 m/s.

Table C.8 - Single-Phase Jet at x/d = 20, S = 0.19[a]

$\frac{r}{x}$	$\frac{\bar{u}}{\bar{u}_c}$	$\frac{(\overline{u'^2})^{1/2}}{\bar{u}_c}$	$\frac{(\overline{v'^2})^{1/2}}{\bar{u}_c}$	$\frac{(\overline{w'^2})^{1/2}}{\bar{u}_c}$	$\frac{k}{\bar{u}_c^2} \times 10^1$	$\frac{\overline{u'v'}}{\bar{u}_c^2} \times 10^2$
0	1.0	0.274	0.219	0.219	0.866	0.52
.02	.969	.279	.226	.222	.890	1.00
.04	.926	.277	.220	.227	.883	1.51
.06	.841	.270	.213	.232	.860	2.24
.08	.761	.269	.229	.229	.887	2.05
.10	.664	.278	.218	.215	.853	2.14
.12	.540	.244	.199	.193	.681	1.74
.14	.449	.212	.211	.213	.672	1.34
.16	.435	.200	.175	.182	.518	1.62
.18	.311	.191	.178	.155	.459	1.25
.20	.197	.158	.155	-----	-----	.99

[a] $\bar{u}_c$ = 2.72 m/s.

C.1.3 Single-Phase Jet, S = 0.33

Table C.9 - Single-Phase Jet at x/d = 0.5, S = 0.33[a]

$\frac{r}{x}$	$\frac{\bar{u}}{\bar{u}_c}$	$\frac{(\overline{u'^2})^{1/2}}{\bar{u}_c}$	$\frac{(\overline{v'^2})^{1/2}}{\bar{u}_c}$	$\frac{(\overline{w'^2})^{1/2}}{\bar{u}_c}$	$\frac{\bar{w}}{\bar{w}_m}$	$\frac{k}{\bar{u}_c^2} \times 10^1$	$\frac{\overline{u'v'}}{\bar{u}_c^2} \times 10^1$
0	1.0	0.157	0.281	0.281	-0.02	0.910	0.268
.067	1.0	.147	.279	.253	.245	.816	.352
.133	.983	.137	.240	.216	.522	.617	.195
.201	.971	.124	.222	.178	.754	.480	.066
.267	.953	.116	.196	.144	.908	.365	.054
.334	.933	.109	.158	.126	.974	.263	.029
.401	.923	.102	.157	.122	1.00	.250	.022
.501	.907	.103	.136	.110	.998	.206	.049
.601	.900	.101	.120	.105	.972	.178	.129
.701	.879	.117	.107	.097	.923	.173	.338
.801	.834	.147	.114	.114	.846	.238	.650
.901	.713	.201	.132	.152	.690	.404	1.283
1.00	.564	.218	.153	.169	.567	.497	1.771
1.069	.429	.209	.165	.172	.457	.502	1.930
1.136	.300	.185	.174	.170	.367	.468	1.761
1.20	.191	.154	.169	.161	.312	.391	1.310
1.27	.114	.121	.162	.137	.203	.299	.777
1.338	.065	.083	.117	.120	.145	.175	.148

[a] $\bar{u}_c$ = 13.34 m/s, $\bar{w}_m$ = 5.917 m/s.

C.1.3 Single-Phase Jet, S = 0.33

Table C.10 - Single-Phase Jet at x/d = 5, S = 0.33[a]

$\frac{r}{x}$	$\frac{\bar{u}}{\bar{u}_c}$	$\frac{(\overline{u'^2})^{1/2}}{\bar{u}_c}$	$\frac{(\overline{v'^2})^{1/2}}{\bar{u}_c}$	$\frac{(\overline{w'^2})^{1/2}}{\bar{u}_c}$	$\frac{\bar{w}}{\bar{w}_m}$	$\frac{k}{\bar{u}_c^2} \times 10^1$	$\frac{\overline{u'v'}}{\bar{u}_c^2} \times 10^2$
0	1.00	0.274	0.277	0.277	0.280	1.140	0.30
.040	.988	.276	.259	.264	.374	1.067	.49
.080	.939	.289	.264	.257	.550	1.096	1.48
.120	.858	.292	.272	.274	.636	1.172	2.39
.160	.752	.290	.268	.282	.750	1.175	2.15
.20	.623	.285	.266	.272	.931	1.131	2.69
.24	.499	.265	.258	.264	1.00	1.032	2.74
.28	.358	.232	.247	.244	.935	.870	2.48
.32	.268	.205	.243	.223	.786	.752	2.32
.36	.185	.169	.207	.207	.520	.570	1.51
.40	.121	.128	.170	.168	.436	.368	.746
.44	.091	.105	.138	.153	.117	.268	.243

[a] $\bar{u}_c$ = 6.009 m/s, $\bar{w}_m$ = 1.07 m/s.

C-3

Table C.11 - Single-Phase Jet at x/d = 10, S = 0.33[a]

$\frac{r}{x}$	$\frac{\bar{u}}{\bar{u}_c}$	$\frac{(\overline{u'^2})^{1/2}}{\bar{u}_c}$	$\frac{(\overline{v'^2})^{1/2}}{\bar{u}_c}$	$\frac{(\overline{w'^2})^{1/2}}{\bar{u}_c}$	$\frac{\bar{w}}{\bar{w}_m}$	$\frac{k}{\bar{u}_c^2} \times 10^1$	$\frac{\overline{u'v'}}{\bar{u}_c^2} \times 10^2$
0	1.0	0.256	0.265	0.265	0.074	1.028	0.308
.033	.975	.260	.251	.250	.343	.965	.766
.067	.908	.271	.266	.283	.364	1.120	1.70
.100	.786	.264	.246	.315	.522	1.145	1.87
.134	.664	.260	.272	.247	.872	1.014	2.54
.167	.549	.246	.246	.254	.925	.926	2.25
.200	.417	.226	.251	.237	1.00	.849	2.15
.234	.322	.207	.232	.219	.799	.723	1.16
.267	.237	.184	.232	.205	.626	.645	.48
.300	.178	.166	.227	.203	.373	.601	-----
.334	.130	.148	.215	-----	-----	-----	1.11

$a_{\bar{u}_c}$ = 4.191 m/s.

C.2 Particle-Laden Jets: LV Particle Velocities

C.2.1 Particle-Laden Jet, S = 0

Table C.12 - LV Particle Velocities at x/d = 0.5, S = 0[a]

$\frac{r}{x}$	$\frac{\bar{u}_p}{\bar{u}_{pc}}$	$\frac{(\overline{u'^2_p})^{1/2}}{\bar{u}_{pc}}$	$\frac{(\overline{v'^2_p})^{1/2}}{\bar{u}_{pc}}$	$\frac{(\overline{w'^2_p})^{1/2}}{\bar{u}_{pc}}$	$\frac{\bar{v}_p}{\bar{u}_{pc}}$	$\frac{G}{G_m}$
0	1.0	0.083	0.037	0.037	0.005	1.00
.201	.998	.081	.039	.031	.004	.914
.401	.982	.083	.037	.024	.003	.744
.602	.938	.089	.039	.026	.002	.615
.802	.875	.097	.036	.022	.001	.403
.936	.806	.115	.031	.022	.008	-----
1.003	.786	.113	.025	-----	.013	-----
1.070	.668	.161	.022	.024	.019	.129
1.136	.529	.245	.040	.037	.045	-----
1.203	.409	.301	.070	-----	.080	.011

$a_{\bar{u}_{pc}}$ = 13.83 m/s, G_m = 4.664 kg/m^2 s.

Table C.13 - LV Particle Velocities at x/d = 5, S = 0[a]

$\frac{r}{x}$	$\frac{\bar{u}_p}{\bar{u}_{pc}}$	$\frac{(\overline{u'^2})^{1/2}_p}{\bar{u}_{pc}}$	$\frac{(\overline{v'^2})^{1/2}_p}{\bar{u}_{pc}}$	$\frac{(\overline{w'^2})^{1/2}_p}{\bar{u}_{pc}}$	$\frac{\bar{v}_p}{\bar{u}_{pc}}$	$\frac{G}{G_m}$
0	1.0	0.056	0.024	0.024	0.005	1.00
.027	.990	.062	.019	.023	.002	.943
.053	.937	.085	.025	.027	.001	.709
.080	.823	.111	.030	.032	.007	.426
.094	.752	.118	.028	.036	.013	-----
.107	.670	.121	.029	.036	.017	.247
.120	.593	.123	.030	.036	.022	.189
.134	.529	.126	.031	.037	.029	.129
.147	.465	.125	.032	.038	.034	-----
.160	.394	.129	.035	.036	.035	.054
.174	.335	.127	.034	.036	.037	-----
.187	.287	.126	.035	.035	.037	.025

[a] $\bar{u}_{pc}$ = 14.005 m/s, G_m = 3.689 kg/m^2 s.

Table C.14 - LV Particle Velocities at x/d = 15, S = 0[a]

$\frac{r}{x}$	$\frac{\bar{u}_p}{\bar{u}_{pc}}$	$\frac{(\overline{u'^2})^{1/2}_p}{\bar{u}_{pc}}$	$\frac{(\overline{v'^2})^{1/2}_p}{\bar{u}_{pc}}$	$\frac{(\overline{w'^2})^{1/2}_p}{\bar{u}_{pc}}$	$\frac{\bar{v}_p}{\bar{u}_{pc}}$	$\frac{G}{G_m}$
0	1.00	0.157	0.049	0.049	0.007	1.00
.018	.953	.162	.052	.055	.011	.712
.036	.828	.167	.056	.062	.026	.388
.053	.676	.174	.063	.069	.047	.182
.071	.515	.163	.065	.073	.052	.099
.089	.393	.148	.065	.070	.054	.052
.107	.275	.124	.062	.062	.053	.031
.116	.234	.115	.061	.059	.052	-----
.125	.197	.102	.057	.058	.051	.020
.134	.178	.095	.055	.055	.049	-----

[a] $\bar{u}_{pc}$ = 8.881 m/s, G_m = 1.774 kg/m^2 s.

Table C.15 - LV Particle Velocities at x/d = 30, S = 0[a]

$\frac{r}{x}$	$\frac{\bar{u}_p}{\bar{u}_{pc}}$	$\frac{(\overline{u'^2})^{1/2}_p}{\bar{u}_{pc}}$	$\frac{(\overline{v'^2})^{1/2}_p}{\bar{u}_{pc}}$	$\frac{(\overline{w'^2})^{1/2}_p}{\bar{u}_{pc}}$	$\frac{\bar{v}_p}{\bar{u}_{pc}}$	$\frac{G}{G_m}$
0	1.0	0.216	0.118	0.118	0.005	1.00
.018	.987	.213	.114	.118	.028	.796
.036	.921	.215	.120	.121	.060	.445
.053	.772	.215	.127	.134	.083	.337
.071	.629	.199	.125	.139	.098	.226
.089	.493	.187	.120	.133	.103	.137
.107	.412	.163	.115	.124	.106	.104
.125	.299	.149	.108	.110	.101	-----

$a\ \bar{u}_{pc} = 4.102$ m/s, $G_m = 0.264$ kg/m^2 s.

C.2.2 Particle-Laden Jet, S = 0.16

Table C.16 - LV Particle Velocities at x/d = 0.5, S = 0.16[a]

$\frac{r}{x}$	$\frac{\bar{u}_p}{\bar{u}_{pc}}$	$\frac{(\overline{u'^2})^{1/2}_p}{\bar{u}_{pc}}$	$\frac{(\overline{v'^2})^{1/2}_p}{\bar{u}_{pc}}$	$\frac{(\overline{w'^2})^{1/2}_p}{\bar{u}_{pc}}$	$\frac{\bar{v}_p}{\bar{u}_{pc}}$	$\frac{\bar{w}_p}{\bar{w}_{pm}}$	$\frac{G}{G_m}$
0	1.0	0.143	0.142	0.134	0	-0.044	0.148
.201	.986	.134	.132	.117	.005	.705	.304
.401	.965	.117	.117	.085	.002	1.0	.520
.602	.940	.112	.097	.063	.004	.949	.892
.802	.922	.117	.075	.049	.042	.907	1.00
1.003	.857	.190	.055	.047	.102	.779	.720
1.136	.712	.238	.058	.046	.148	.600	.112
1.270	.515	.326	.123	.058	.167	.454	.040
1.404	.195	.294	.130	.061	.046	.119	-----

$a\ \bar{u}_{pc} = 10.393$ m/s, $\bar{w}_{pm} = 1.627$ m/s, $G_m = 3.125$ kg/m^2 s.

Table C.17 - LV Particle Velocities at x/d = 2, S = 0.16[a]

$\frac{r}{x}$	$\frac{\bar{u}_p}{\bar{u}_{pc}}$	$\frac{(\overline{u'^2})^{1/2}_p}{\bar{u}_{pc}}$	$\frac{(\overline{v'^2})^{1/2}_p}{\bar{u}_{pc}}$	$\frac{(\overline{w'^2})^{1/2}_p}{\bar{u}_{pc}}$	$\frac{\bar{v}_p}{\bar{u}_{pc}}$	$\frac{\bar{w}_p}{\bar{w}_{pm}}$	$\frac{G}{G_m}$
0	1.0	0.103	0.072	0.070	0.010	-0.036	0.205
.067	.994	.098	.066	.057	.044	.610	.277
.134	.964	.097	.061	.043	.064	.980	.498
.201	.913	.129	.056	.040	.077	1.00	.951
.267	.806	.158	.052	.034	.090	.874	1.00
.334	.573	.209	.050	.035	.079	.681	.566
.401	.398	.226	.055	.032	.081	.421	.152
.468	.275	.219	.065	.031	.071	.180	.037
.535	.202	.204	.073	.027	.058	.181	-----
.602	.120	.163	.071	.025	.033	.043	-----

$a\ \bar{u}_{pc}$ = 10.775 m/s, $\bar{w}_{pm}$ = 1.075 m/s, G_m = 1.640 kg/m^2 s.

Table C.18 - LV Particle Velocities at x/d = 5, S = 0.16[a]

$\frac{r}{x}$	$\frac{\bar{u}_p}{\bar{u}_{pc}}$	$\frac{(\overline{u'^2})^{1/2}_p}{\bar{u}_{pc}}$	$\frac{(\overline{v'^2})^{1/2}_p}{\bar{u}_{pc}}$	$\frac{(\overline{w'^2})^{1/2}_p}{\bar{u}_{pc}}$	$\frac{\bar{v}_p}{\bar{u}_{pc}}$	$\frac{\bar{w}_p}{\bar{w}_{pm}}$	$\frac{G}{G_m}$
0	1.0	0.163	0.067	0.057	0.031	-0.620	0.294
.053	.969	.182	.074	.065	.031	.340	.432
.107	.819	.206	.069	.063	.052	.636	.937
.134	.711	.219	.061	.058	.060	.824	1.00
.160	.612	.216	.060	.056	.069	1.0	.846
.187	.501	.217	.055	.053	.069	.836	.698
.214	.357	.201	.053	.042	.058	.848	.449
.241	.275	.176	.051	.042	.048	.585	.307
.267	.199	.154	.049	.035	.050	.342	-----
.294	.137	.127	.040	.029	.039	.150	-----

$a\ \bar{u}_{pc}$ = 9.239 m/s, $\bar{w}_{pm}$ = 0.494 m/s, G_m = 0.681 kg/m^2 s.

Table C.19 - LV Particle Velocities at x/d = 10, S = 0.16[a]

$\frac{r}{x}$	$\frac{\bar{u}_p}{\bar{u}_{pc}}$	$\frac{(\overline{u'^2})^{1/2}_p}{\bar{u}_{pc}}$	$\frac{(\overline{v'^2})^{1/2}_p}{\bar{u}_{pc}}$	$\frac{(\overline{w'^2})^{1/2}_p}{\bar{u}_{pc}}$	$\frac{\bar{v}_p}{\bar{u}_{pc}}$	$\frac{G}{G_m}$
0	1.0	0.227	0.108	0.104	0.009	1.00
.027	.960	.236	.107	.112	.022	.951
.053	.879	.238	.098	.117	.024	.931
.080	.757	.242	.097	.107	.045	.815
.107	.604	.231	.089	.094	.060	.693
.134	.465	.199	.081	.085	.068	.522
.160	.336	.188	.080	.073	.066	.358
.187	.224	.148	.067	.062	.063	.244
.214	.153	.114	.063	.058	.057	-----

$a\bar{u}_{pc}$ = 6.447 m/s, $\bar{w}_{pm}$ = 0.318 m/s, G_m = 0.307 kg/m^2 s.

Table C.20 - LV Particle Velocities at x/d = 20, S = 0.16[a]

$\frac{r}{x}$	$\frac{\bar{u}_p}{\bar{u}_{pc}}$	$\frac{(\overline{u'^2})^{1/2}_p}{\bar{u}_{pc}}$	$\frac{(\overline{v'^2})^{1/2}_p}{\bar{u}_{pc}}$	$\frac{(\overline{w'^2})^{1/2}_p}{\bar{u}_{pc}}$	$\frac{\bar{v}_p}{\bar{u}_{pc}}$	$\frac{G}{G_m}$
0	1.0	0.241	0.136	0.130	0.005	1.00
.020	1.03	.243	.162	.128	.027	.954
.040	.950	.242	.168	.127	.058	.820
.060	.825	.249	.163	.124	.067	.658
.080	.718	.232	.130	.121	.089	.579
.100	.595	.219	.160	.116	.098	.456
.120	.499	.199	.122	.106	.100	.368
.140	.415	.183	.113	.101	.109	.294
.160	.330	.161	.104	.108	.095	.210
.180	.259	.132	.095	.093	.098	.171

$a\bar{u}_{pc}$ = 3.693 m/s, $\bar{w}_{pm}$ = 0.106 m/s, G_m = 0.144 k/m^2 s.

C.2.3 Particle-Laden Jet, S = 0.3

Table C.21 - LV Particle Velocities at x/d = 0.5, S = 0.3[a]

$\frac{r}{x}$	$\frac{\bar{u}_p}{\bar{u}_{pc}}$	$\frac{(\overline{u'^2})^{1/2}_p}{\bar{u}_{pc}}$	$\frac{(\overline{v'^2})^{1/2}_p}{\bar{u}_{pc}}$	$\frac{(\overline{w'^2})^{1/2}_p}{\bar{u}_{pc}}$	$\frac{\bar{v}_p}{\bar{u}_{pc}}$	$\frac{\bar{w}_p}{\bar{w}_{pm}}$	$\frac{G}{G_m}$
0	1.0	0.165	0.113	0.119	0.101	-0.242	0.105
.134	1.017	.159	.109	.130	.116	.069	.136
.267	1.004	.154	.115	.137	.113	.441	.204
.401	.993	.142	.112	.124	.105	.745	.320
.535	.988	.130	.110	.099	.086	.934	.513
.668	.982	.123	.109	.082	.076	1.00	.835
.802	.973	.128	.097	.087	.078	.980	1.00
.936	.926	.162	.080	.065	.094	.902	.927
1.069	.809	.230	.068	.064	.123	.731	.750
1.203	.700	.269	.075	.072	.163	.614	.265
1.337	.382	.370	.148	.092	.127	.308	-----
1.471	.063	.233	.134	.066	.032	.054	-----

[a] $\bar{u}_{pc}$ = 10.26 m/s, $\bar{w}_{pm}$ = 2.258 m/s, G_m = 2.595 kg/m^2 s.

Table C.22 - LV Particle Velocities at x/d = 2, S = 0.3[a]

$\frac{r}{x}$	$\frac{\bar{u}_p}{\bar{u}_{pc}}$	$\frac{(\overline{u'^2})^{1/2}_p}{\bar{u}_{pc}}$	$\frac{(\overline{v'^2})^{1/2}_p}{\bar{u}_{pc}}$	$\frac{(\overline{w'^2})^{1/2}_p}{\bar{u}_{pc}}$	$\frac{\bar{v}_p}{\bar{u}_{pc}}$	$\frac{\bar{w}_p}{\bar{w}_{pm}}$	$\frac{G}{G_m}$
0	1.0	0.107	0.060	0.062	0.022	0.049	0.091
.067	1.005	.104	.063	.069	.043	.445	.131
.134	.979	.103	.060	.054	.065	.922	.415
.20	.934	.121	.059	.046	.075	1.00	.734
.267	.828	.164	.061	.048	.095	.874	1.00
.334	.620	.202	.060	.052	.096	.648	.833
.401	.445	.200	.059	.046	.092	.438	.468
.468	.337	.183	.062	.035	.084	.297	.191
.535	.229	.184	.074	.039	.068	.188	-----
.602	.130	.160	.076	.031	.045	.103	-----
.668	.070	.123	.062	.027	.026	.024	-----

[a] $\bar{u}_{pc}$ = 11.133 m/s, $\bar{w}_{pm}$ = 1.613 m/s, G_m = 1.020 kg/m^2 s.

Table C.23 - LV Particle Velocities at x/d = 5, S = 0.3[a]

$\frac{r}{x}$	$\frac{\bar{u}_p}{\bar{u}_{pc}}$	$\frac{(\overline{u'^2})^{1/2}_p}{\bar{u}_{pc}}$	$\frac{(\overline{v'^2})^{1/2}_p}{\bar{u}_{pc}}$	$\frac{(\overline{w'^2})^{1/2}_p}{\bar{u}_{pc}}$	$\frac{\bar{v}_p}{\bar{u}_{pc}}$	$\frac{\bar{w}_p}{\bar{w}_{pm}}$	$\frac{G}{G_m}$
0	1.00	0.184	0.095	0.107	-0.023	0.332	0.202
.040	.960	.200	.086	.110	-.032	.752	-----
.054	-----	-----	-----	-----	------	-----	.252
.080	.868	.211	.081	.087	-.008	.944	-----
.107	-----	-----	-----	-----	------	-----	.690
.120	.781	.220	.076	.079	.021	1.00	-----
.160	.636	.219	.082	.070	.043	.950	1.00
.201	.466	.201	.065	.062	.058	.856	-----
.214	-----	-----	-----	-----	-----	-----	.876
.241	.333	.178	.073	.073	.059	.547	-----
.267	-----	-----	-----	-----	-----	-----	.507
.281	.231	.139	.067	.035	.060	.273	-----
.321	.167	.110	.057	.026	.059	.163	.289
.361	.116	.090	.054	.020	.051	.070	-----
.401	.079	.077	.048	-----	.043	-----	-----

$a_{\bar{u}_{pc}}$ = 9.297 m/s, $\bar{w}_{pm}$ = 0.674 m/s, G_m = 0.436 kg/m^2 s.

Table C.24 - LV Particle Velocities at x/d = 10, S = 0.3[a]

$\frac{r}{x}$	$\frac{\bar{u}_p}{\bar{u}_{pc}}$	$\frac{(\overline{u'^2})^{1/2}_p}{\bar{u}_{pc}}$	$\frac{(\overline{v'^2})^{1/2}_p}{\bar{u}_{pc}}$	$\frac{(\overline{w'^2})^{1/2}_p}{\bar{u}_{pc}}$	$\frac{\bar{v}_p}{\bar{u}_{pc}}$	$\frac{\bar{w}_p}{\bar{w}_{pm}}$	$\frac{G}{G_m}$
0	1.0	0.218	0.120	0.114	-0.038	0.949	0.922
.027	.969	.283	.113	.117	-.021	.854	.936
.053	.877	.239	.104	.120	.003	.792	.954
.080	.778	.238	.097	.111	.022	.830	.995
.107	.655	.228	.096	.110	.041	.892	1.00
.134	.528	.215	.090	.105	.053	1.0	.885
.160	.416	.188	.088	.098	.061	.774	.601
.187	.330	.167	.087	.087	.070	.518	.472
.214	.260	.139	.081	.078	.073	.650	.312
.241	.198	.115	.078	.066	.074	.439	-----
.267	.148	.095	.070	.062	.071	.423	-----
.294	.117	.079	.067	.051	.070	.124	-----

$a_{\bar{u}_{pc}}$ = 6.317 m/s, $\bar{w}_{pm}$ = 0.371 m/s, G_m = 0.218 kg/m^2 s.

Table C.25 - LV Particle Velocities at x/d = 20, S = 0.3[a]

$\frac{r}{x}$	$\frac{\bar{u}_p}{\bar{u}_{pc}}$	$\frac{(\overline{u'^2})^{1/2}_p}{\bar{u}_{pc}}$	$\frac{(\overline{v'^2})^{1/2}_p}{\bar{u}_{pc}}$	$\frac{(\overline{w'^2})^{1/2}_p}{\bar{u}_{pc}}$	$\frac{\bar{v}_p}{\bar{u}_{pc}}$	$\frac{G}{G_m}$
0	1.0	0.235	0.150	0.145	-0.030	1.00
.020	1.001	.232	.145	.148	.004	.966
.040	.940	.237	.145	.150	.014	.914
.060	.824	.223	.145	.145	.047	.864
.080	.745	.231	.140	.148	.058	.738
.100	.646	.230	.134	.144	.077	.611
.120	.542	.201	.127	.138	.074	.504
.140	.463	.183	.123	.126	.075	.445
.160	.378	.160	.119	.117	.077	.344
.180	.326	.143	.109	.112	.085	.250
.201	.280	.125	.101	.100	.086	-----
.221	.236	.112	.096	.094	.087	-----
.241	.214	.096	.084	-----	.082	-----

[a] $\bar{u}_{pc}$ = 3.867 m/s, $\bar{w}_{pm}$ = 0.075 m/s, G_m = 0.112 kg/m^2 s.

C.3 Particle-Laden Jets: Phase/Doppler Velocities

C.3.1 Particle-Laden Jet, Gas-Phase Velocities, S = 0

Table C.26 - Phase/Doppler Velocities at x/d = 0.5, S = 0[a]

$\frac{r}{x}$	$\frac{\bar{u}}{\bar{u}_c}$	$\frac{(\overline{u'^2})^{1/2}}{\bar{u}_c}$
0	1.01	0.041
.094	1.01	.050
.200	.982	.046
.294	.996	.042
.401	.931	.057
.495	.938	.054
.602	.866	.060
.695	.866	.065
.802	.778	.092
.829	.814	-----
.896	.749	.096
.936	.618	.111
.963	.669	.112
1.03	.567	.103
1.07	.386	.105
1.09	.473	.087
1.13	.306	.090
1.16	.327	.091
1.20	.196	.067
1.27	.109	.049

[a] $\bar{u}_c$ = 13.75 m/s.

Table C.27 - Phase/Doppler Gas-Phase Velocities at x/d = 5, S = 0[a]

$\frac{r}{x}$	$\frac{\bar{u}}{\bar{u}_c}$	$\frac{(\overline{u'^2})^{1/2}}{\bar{u}_c}$
0	1.0	0.069
.027	.977	.075
.053	.891	.081
.080	.707	.128
.107	.566	.122
.120	.488	.118
.134	.430	.112
.147	.328	.102
.160	.293	.098
.174	.238	.088
.187	.219	.082

$a_{\bar{u}_c}$ = 12.80 m/s.

Table C.28 - Phase/Doppler Gas-Phase Velocities at x/d = 15, S = 0[a]

$\frac{r}{x}$	$\frac{\bar{u}}{\bar{u}_c}$	$\frac{(\overline{u'^2})^{1/2}}{\bar{u}_c}$
0	1.0	0.132
.018	.981	.137
.036	.827	.143
.054	.640	.167
.071	.453	.154
.089	.367	.127
.107	.260	.105
.125	.187	.085
.143	.127	.063

$a_{\bar{u}_c}$ = 7.50 m/s.

Table C.29 - Phase/Doppler
Gas-Phase Velocities at
$x/d = 30$, $S = 0^a$

$\frac{r}{x}$	$\frac{\bar{u}}{\bar{u}_c}$	$\frac{(\overline{u'^2})^{1/2}}{\bar{u}_c}$
0	1.0	0.197
.009	1.0	.201
.018	.973	.218
.027	.892	.215
.036	.824	.214
.045	.770	.207
.054	.608	.181
.063	.577	.185
.071	.541	.184
.080	.460	.153
.089	.378	.142
.098	.338	.134
.107	.324	.119

$a_{\bar{u}_c} = 3.7$ m/s.

C.3.2 Particle-Laden Jet, Particle Velocities, S = 0

Table C.30 - Phase/Doppler Particle Velocities at x/d = 0.5, S = 0

$\frac{r}{x}$	Average particle size μm	$\bar{u}_p$ m/s	$(\overline{u'^2_p})^{1/2}$ m/s
0	14.3	13.608	0.725
.201		13.443	.747
.401		12.626	.938
.602		11.789	.921
.802		9.937	1.365
.936		7.927	1.678
1.069		3.150	1.600
1.136		1.717	.960
0	23.7	13.278	0.712
.201		12.998	.807
.401		12.397	.905
.602		11.640	1.010
.802		10.084	1.378
.936		8.730	1.576
1.069		3.934	1.800
1.136		1.967	1.158
0	33.3	12.906	0.841
.201		12.710	.888
.401		12.285	.986
.602		11.685	1.071
.802		10.479	1.294
.936		9.540	1.421
1.069		5.811	1.809
1.136		2.858	1.691
0	42.7	12.596	0.972
.201		12.482	.983
.401		12.217	1.055
.602		11.740	1.078
.802		10.784	1.184
.936		9.986	1.306
1.069		7.423	1.569
1.136		3.837	2.110

Table C.30 - Cont.

$\frac{r}{x}$	Average particle size μm	$\bar{u}_p$ m/s	$\overline{(u'_p)^2}^{1/2}$ m/s
0	52.2	12.249	1.078
.201		12.259	1.039
.401		12.136	1.062
.602		11.741	1.044
.802		11.064	1.117
.936		10.359	1.230
1.069		8.419	1.434
1.136		4.521	1.897
0	61.7	12.394	0.989
.201		12.330	1.050
.401		12.221	.998
.602		11.950	.942
.802		11.497	1.112
.936		10.533	1.374
1.069		9.122	1.290
1.136		4.450	1.721
0	71.3	12.040	1.160
.201		12.092	1.083
.401		12.081	.976
.602		11.821	1.020
.802		11.281	1.142
.936		10.721	1.260
1.069		9.526	1.210
1.136		1.663	.076

Table C.31 - Phase/Doppler Particle

Velocities at x/d = 5,

S = 0

$\frac{r}{x}$	Average particle size μm	$\bar{u}_p$ m/s	$\overline{(u'^2_p)}^{1/2}$ m/s
0	14.3	13.081	0.750
.027		12.473	.984
.053		10.826	1.571
.080		8.807	1.731
.107		6.907	1.703
.134		5.063	1.641
.160		3.288	1.357
.187		1.901	.959
.214		.997	.604
0	23.7	12.293	0.740
.027		12.433	.911
.053		10.975	1.424
.080		9.090	1.610
.107		7.263	1.626
.134		5.468	1.615
.160		3.574	1.331
.187		2.143	.984
.214		1.166	.646
0	33.3	12.872	0.648
.027		12.457	.801
.053		11.215	1.270
.080		9.529	1.455
.107		7.705	1.561
.134		5.973	1.564
.160		4.135	1.389
.187		2.665	1.114
.214		1.579	.737
0	42.7	12.823	0.641
.027		12.513	.751
.053		11.457	1.126
.080		9.926	1.334
.107		8.178	1.451
.134		6.537	1.470
.160		4.761	1.314
.187		3.213	1.135
.214		1.921	.787

Table C.31 - Cont.

$\frac{r}{x}$	Average particle size μm	$\bar{u}_p$ m/s	$\overline{(u'^2_p)}^{1/2}$ m/s
0	52.2	12.687	0.727
.027		12.470	.744
.053		11.668	.957
.080		10.393	1.206
.107		8.661	1.339
.134		7.046	1.344
.160		5.370	1.267
.187		3.728	1.108
.214		2.218	.819
0	61.7	12.660	0.743
.027		12.460	.750
.053		11.849	.881
.080		10.608	1.392
.107		9.061	1.246
.134		7.696	1.216
.160		6.099	1.199
.187		4.286	1.145
.214		2.613	.709
0	71.3	12.613	0.713
.027		12.419	.755
.053		12.016	.777
.080		10.855	1.192
.107		9.296	1.202
.134		8.112	1.201
.160		6.738	1.088
.187		4.904	1.212
.214		2.637	.749

Table C.32 - Phase/Doppler Particle Velocities at x/d = 15, S = 0

$\frac{r}{x}$	Average particle size μm	$\bar{u}_p$ m/s	$(\overline{u'^2_p})^{1/2}$ m/s
0	14.2	7.658	1.145
.018		7.150	1.330
.036		6.016	1.358
.053		5.003	1.469
.071		3.511	1.242
.089		2.395	.988
.107		1.524	.695
.125		1.122	.600
.143		.609	.333
0	23.7	7.721	1.167
.018		7.213	1.253
.036		6.206	1.300
.053		5.074	1.379
.071		3.596	1.224
.089		2.397	1.003
.107		1.469	.697
.125		1.105	.613
.143		.600	.343
0	33.3	7.950	1.158
.018		7.445	1.223
.036		6.401	1.308
.053		5.356	1.323
.071		3.913	1.266
.089		2.729	1.059
.107		1.786	.754
.125		1.343	.682
.143		.728	.387
0	42.7	8.303	1.159
.018		7.724	1.223
.036		6.622	1.228
.053		5.504	1.324
.071		4.096	1.237
.089		2.997	1.064
.107		1.963	.765
.125		1.464	.704
.143		.825	.408

Table C.32 - Cont.

$\frac{r}{x}$	Average particle size μm	$\bar{u}_p$ m/s	$\overline{(u'^2_p)}^{1/2}$ m/s
0	52.2	8.852	1.099
.018		8.144	1.237
.036		6.923	1.243
.053		5.682	1.334
.071		4.267	1.203
.089		3.207	1.075
.107		2.133	.758
.125		1.655	.740
.143		.924	.423
0	61.7	9.265	1.116
.018		8.473	1.217
.036		7.129	1.333
.053		5.960	1.281
.071		4.471	1.222
.089		3.341	1.071
.107		2.269	.749
.125		1.819	.741
.143		.994	.422
0	71.3	9.572	1.179
.018		8.781	1.286
.036		7.494	1.345
.053		6.334	1.323
.071		4.720	1.201
.089		3.514	1.061
.107		2.310	.698
.125		1.926	.741
.143		1.112	.394

Table C.33 - Phase/Doppler Particle

Velocities at x/d = 30,

S = 0

$\frac{r}{x}$	Average particle size μm	$\bar{u}_p$ m/s	$\overline{(u'^2_p)}^{1/2}$ m/s
0	14.3	3.556	0.866
.009		3.584	.798
.018		3.499	.829
.027		3.086	.835
.036		2.905	.730
.045		2.710	.791
.053		2.471	.729
.062		2.121	.777
.071		1.652	.608
.080		1.515	.579
.089		1.349	.596
.098		1.335	.552
.107		1.081	.514
0	23.7	3.602	0.830
.009		3.612	.837
.018		3.516	.858
.027		3.082	.823
.036		2.974	.766
.045		2.770	.799
.053		2.464	.775
.062		2.129	.761
.071		1.596	.610
.080		1.465	.613
.089		1.334	.592
.098		1.224	.556
.107		1.080	.528
0	33.3	3.716	0.830
.009		3.729	.815
.018		3.631	.809
.027		3.262	.790
.036		3.074	.783
.045		2.873	.808
.053		2.590	.791
.062		2.262	.768
.071		1.810	.634
.080		1.619	.643
.089		1.491	.635
.098		1.360	.586
.107		1.131	.558

Table C.33 - Cont.

$\frac{r}{x}$	Average particle size μm	$\bar{u}_p$ m/s	$\overline{(u'^2_p)}^{1/2}$ m/s
0	42.7	3.715	0.788
.009		3.786	.786
.018		3.628	.783
.027		3.344	.772
.036		3.200	.769
.045		2.873	.808
.053		2.756	.788
.062		2.355	.791
.071		1.941	.653
.080		1.728	.656
.089		1.585	.654
.098		1.426	.615
.107		1.225	.574
0	52.2	3.843	0.772
.009		3.842	.767
.018		3.700	.764
.027		3.457	.764
.036		3.328	.768
.045		3.113	.790
.053		2.869	.771
.062		2.521	.783
.071		2.125	.650
.080		1.895	.686
.089		1.708	.670
.098		1.539	.628
.107		1.340	.605
0	61.7	3.966	0.793
.009		3.923	.784
.018		3.824	.768
.027		3.564	.768
.036		3.439	.720
.045		3.223	.768
.053		3.000	.745
.062		2.600	.773
.071		2.222	.655
.080		1.989	.656
.089		1.823	.678
.098		1.656	.617
.107		1.408	.604
0	71.3	4.156	0.806
.009		4.156	.786
.018		4.020	.763
.027		3.752	.742
.036		3.570	.764
.045		3.402	.775
.053		3.127	.741
.062		2.713	.755
.071		2.290	.623
.080		2.052	.662
.089		1.906	.641
.098		1.789	.590
.107		1.500	.595

C.3.3 Particle-Laden Jet, Gas-Phase Velocities, S = 0.16

Table C.34 - Phase/Doppler
Gas-Phase Velocities at
$x/d = 0.5$, $S = 0.16$[a]

$\frac{r}{x}$	$\frac{\bar{u}}{\bar{u}_c}$	$\frac{(\overline{u'^2})^{1/2}}{\bar{u}_c}$
0	1.0	0.063
.080	1.0	.061
.174	.966	.082
.281	.966	.079
.374	1.03	.058
.481	1.02	.069
.575	1.02	.081
.602	.992	.102
.775	.992	.095
.882	.924	.120
.909	.857	.154
.976	.630	.166
1.016	.546	.151
1.043	.336	.131
1.083	.311	.116
1.11	.176	.084
1.15	.160	.084
1.18	.067	.032
1.22	.067	.034
1.24	.042	.015
1.30	.042	.019

[a] $\bar{u}_c$ = 11.90 m/s.

Table C.35 - Phase/Doppler Gas-Phase Velocities at x/d = 2, S = 0.16[a]

$\frac{r}{x}$	$\frac{\bar{u}}{u_c}$	$\frac{(\overline{u'^2})^{1/2}}{u_c}$
0	1.0	0.075
.067	.974	.083
.134	.974	.124
.201	.814	.171
.267	.580	.133
.334	.303	.117
.401	.069	.039
.468	.030	.012

$a_{\bar{u}_c}$ = 11.55 m/s.

Table C.36 - Phase/Doppler Gas-Phase Velocities at x/d = 5, S = 0.16[a]

$\frac{r}{x}$	$\frac{\bar{u}}{u_c}$	$\frac{(\overline{u'^2})^{1/2}}{u_c}$
0	1.0	0.154
.054	.877	.157
.107	.605	.185
.134	.451	.150
.160	.328	.125
.187	.226	.098
.214	.123	.065
.241	.061	.032

$a_{\bar{u}_c}$ = 9.75 m/s.

Table C.37 - Phase/Doppler Gas-Phase Velocities at x/d = 10, S = 0.16[a]

$\frac{r}{x}$	$\frac{\bar{u}}{\bar{u}_c}$	$\frac{(\overline{u'^2})^{1/2}}{\bar{u}_c}$
0	1.0	0.223
.027	.928	.226
.054	.808	.224
.080	.640	.202
.107	.432	.163
.134	.336	.140
.160	.176	.098
.187	.096	.053

[a] $\bar{u}_c$ = 6.25 m/s.

Table C.38 - Phase/Doppler Gas-Phase Velocities at x/d = 20, S = 0.16[a]

$\frac{r}{x}$	$\frac{\bar{u}}{\bar{u}_c}$	$\frac{(\overline{u'^2})^{1/2}}{\bar{u}_c}$
0	1.0	0.271
.020	.934	.266
.040	.853	.262
.060	.738	.254
.080	.590	.231
.100	.459	.211
.120	.328	.171
.140	.197	.107
.160	.164	.089
.180	.098	.048

[a] $\bar{u}_c$ = 3.05 m/s.

C.3.4 Particle-Laden Jet, Particle Velocities, S = 0.16

Table C.39 - Phase/Doppler Particle Velocities at x/d = 0.5, S = 0.16

$\frac{r}{x}$	Average particle size μm	$\bar{u}_p$ m/s	$\overline{(u'^2_p)}^{1/2}$ m/s
0	14.3	11.193	1.131
.201		10.786	1.146
.401		10.555	1.250
.602		10.607	1.403
.802		8.851	1.513
.936		7.699	1.772
1.00		5.676	1.878
1.069		3.870	1.695
1.136		2.688	1.265
1.203		1.600	.843
1.270		1.242	.597
1.337		1.030	.548
0	23.7	10.307	1.105
.201		10.123	1.153
.401		9.844	1.221
.602		9.837	1.299
.802		8.576	1.384
.936		7.748	1.699
1.0		6.201	1.867
1.069		4.539	1.703
1.176		3.190	1.368
1.203		1.918	.931
1.270		1.324	.742
1.337		1.165	.735
0	33.3	9.694	1.227
.201		9.525	1.197
.401		9.390	1.110
.602		9.475	1.160
.802		8.587	1.231
.936		8.306	1.488
1.00		7.275	1.592
1.069		5.850	1.655
1.136		4.556	1.426
1.203		2.712	1.014
1.270		1.774	.840
1.337		1.553	.883

Table C.39 - Cont.

$\frac{r}{x}$	Average particle size, μm	$\bar{u}_p$, m/s	$(\overline{u'^2_p})^{1/2}$, m/s
0	42.7	9.228	1.299
.201		9.085	1.221
.401		9.047	1.072
.602		9.158	1.050
.802		8.624	1.107
.936		8.598	1.249
1.0		7.968	1.368
1.069		6.929	1.460
1.136		5.808	1.322
1.203		3.536	1.045
1.270		2.099	.957
1.337		1.354	1.007
0	52.2	8.929	1.394
.201		8.775	1.288
.401		8.769	1.088
.602		8.878	1.006
.802		8.523	1.010
.936		8.654	1.132
1.00		8.243	1.213
1.069		7.596	1.326
1.136		6.641	1.181
1.203		4.025	.953
1.270		2.309	.954
1.337		1.973	1.015
0	61.7	8.228	1.411
.201		8.338	1.468
.401		8.171	1.114
.602		8.326	1.023
.802		8.094	.952
.936		8.532	1.116
1.00		8.347	1.112
1.069		7.803	1.182
1.136		6.927	1.019
1.203		4.088	.942
1.270		2.117	.882
1.337		1.575	.714
0	71.3	8.319	1.535
.201		8.191	1.300
.401		8.185	1.054
.602		8.286	.975
.802		8.056	.881
.936		8.312	1.013
1.0		8.279	1.109
1.069		7.562	1.295
1.136		6.990	1.096
1.203		3.527	.796
1.270		1.572	.882
1.337		1.314	.078

Table C.40 - Phase/Doppler Particle

Velocities at x/d = 2,

S = 0.16

$\frac{r}{x}$	Average particle size μm	$\bar{u}_p$ m/s	$\overline{(u'^2_p)}^{1/2}$ m/s
0	14.3	10.980	0.907
.067		11.080	.955
.134		10.307	1.321
.201		8.900	1.626
.267		6.652	1.523
.334		3.668	1.497
.368		1.441	.756
.401		.867	.483
0	23.7	10.650	0.878
.067		10.673	.931
.134		9.918	1.145
.201		8.814	1.455
.267		6.957	1.441
.334		3.957	1.489
.368		1.535	.828
.401		.791	.454
0	33.3	10.272	0.890
.067		10.281	.915
.134		9.794	.895
.201		9.151	1.170
.267		7.448	1.378
.334		4.634	1.528
.368		1.917	.941
.401		.933	.588
0	42.7	9.755	1.114
.067		9.858	.980
.134		9.662	.910
.201		9.181	.985
.267		8.056	1.20
.334		6.043	1.344
.368		2.807	.927
.401		1.662	.762

Table C.40 - Cont.

$\frac{r}{x}$	Average particle size, μm	$\bar{u}_p$, m/s	$\overline{(u'^2_p)}^{1/2}$, m/s
0	52.2	9.755	1.114
.067		9.811	1.023
.134		9.533	.921
.201		9.128	.939
.267		8.180	1.116
.334		6.441	1.245
.368		3.318	.857
.401		2.041	.801
0	61.7	9.725	1.322
.067		9.732	1.238
.134		9.175	.951
.201		8.803	.910
.267		8.106	1.020
.334		6.936	1.127
.368		3.883	.785
.401		2.719	.678
0	71.3	9.472	1.347
.067		9.610	1.163
.134		9.181	.996
.201		8.780	.844
.267		8.138	.976
.334		6.949	1.105
.368		4.013	.801
.401		2.819	.715

Table C.41 - Phase/Doppler Particle Velocities at x/d = 5, S = 0.16

$\frac{r}{x}$	Average particle size μm	$\bar{u}_p$ m/s	$\overline{(u'^2_p)}^{1/2}$ m/s
0	14.3	9.936	1.164
.053		8.837	1.546
.107		6.788	1.639
.134		5.252	1.491
.160		3.981	1.471
.187		2.582	1.076
.214		1.843	.882
.241		1.070	.677
.267		.813	.544
0	23.7	9.700	1.143
.053		8.682	1.423
.107		6.785	1.580
.134		5.280	1.493
.160		4.070	1.437
.187		2.673	1.094
.214		2.002	1.120
.241		1.084	.644
.267		.790	.510
0	33.3	9.531	1.105
.053		8.632	1.368
.107		6.904	1.566
.134		5.510	1.478
.160		4.377	1.473
.187		3.038	1.141
.214		2.308	1.071
.241		1.798	.728
.267		.999	.592
0	42.7	9.592	1.088
.053		8.693	1.339
.107		7.178	1.539
.134		5.818	1.500
.160		4.692	1.474
.187		3.330	1.171
.214		2.585	1.104
.241		1.573	.923
.267		1.159	.657

Table C.41 - Cont.

$\frac{r}{x}$	Average particle size, μm	$\bar{u}_p$, m/s	$\overline{(u'^2_p)}^{1/2}$, m/s
0	52.2	9.823	1.192
.053		9.125	1.278
.107		7.583	1.401
.134		6.281	1.478
.160		5.238	1.523
.187		3.768	1.219
.214		2.961	1.166
.241		1.826	.769
.267		1.400	.690
0	61.7	9.974	1.274
.053		8.887	1.365
.107		7.964	1.218
.134		6.815	1.320
.160		5.957	1.412
.187		4.331	1.176
.214		3.603	1.174
.241		2.184	.747
.267		1.792	.697
0	71.3	10.668	1.236
.053		9.047	1.460
.107		7.979	1.257
.134		7.101	1.286
.160		6.371	1.356
.187		4.771	1.109
.214		4.168	1.162
.241		2.539	.662
.267		2.223	.656

Table C.42 - Phase/Doppler Particle Velocities at x/d = 10, S = 0.16

$\frac{r}{x}$	Average particle size μm	$\bar{u}_p$ m/s	$\overline{(u'^2_p)}^{1/2}$ m/s
0	14.3	7.161	1.377
.027		6.665	1.362
.053		5.882	1.456
.080		4.691	1.430
.107		3.090	1.167
.130		2.370	1.099
.160		1.441	.685
.187		1.127	.624
.214		.647	.342
0	23.7	6.992	1.344
.027		6.770	1.330
.053		5.880	1.451
.080		4.680	1.412
.107		3.017	1.154
.134		2.314	1.005
.160		1.368	.696
.187		1.026	.599
.214		.565	.326
0	33.3	6.959	1.321
.027		6.845	1.321
.053		5.899	1.411
.080		4.808	1.396
.107		3.318	1.147
.134		2.566	1.060
.160		1.601	.739
.187		1.184	.658
.214		.619	.352
0	42.7	6.773	1.348
.027		6.742	1.361
.053		5.874	1.426
.080		4.786	1.370
.107		3.476	1.167
.134		2.670	1.083
.160		1.728	.766
.187		1.293	.701
.214		.687	.371

Table C.42 - Cont.

$\frac{r}{x}$	Average particle size, μm	$\bar{u}_p$, m/s	$\overline{(u'^2_p)}^{1/2}$, m/s
0	52.2	6.614	1.441
.027		6.643	1.391
.053		5.796	1.415
.080		4.817	1.365
.107		3.612	1.183
.134		2.812	1.076
.160		1.877	.776
.187		1.435	.723
.214		.779	.398
0	61.7	6.576	1.625
.027		6.682	1.522
.053		5.882	1.460
.080		4.899	1.459
.107		3.748	1.192
.134		2.929	1.095
.160		1.982	.769
.187		1.532	.749
.214		.857	.403
0	71.3	7.060	1.810
.027		6.768	1.586
.053		6.100	1.492
.080		5.093	1.432
.107		3.963	1.241
.134		3.164	1.152
.160		2.133	.729
.187		1.701	.735
.214		.963	.392

Table C.43 - Phase/Doppler Particle Velocities at x/d = 20, S = 0.16

$\frac{r}{x}$	Average particle size μm	$\bar{u}_p$ m/s	$\overline{(u'^2_p)}^{1/2}$ m/s
0	14.3	3.559	0.845
.020		3.424	.793
.040		3.170	.806
.060		2.800	.832
.080		2.483	.784
.100		1.856	.618
.120		1.548	.631
.140		1.274	.565
.160		.990	.428
.180		.727	.340
0	23.7	3.621	0.846
.020		3.454	.826
.040		3.170	.825
.060		2.817	.844
.080		2.477	.800
.100		1.815	.617
.120		1.470	.619
.140		1.242	.565
.160		.944	.425
.180		.675	.322
0	33.3	3.781	0.826
.020		3.575	.822
.040		3.318	.845
.060		2.939	.852
.080		2.595	.820
.100		1.969	.637
.120		1.604	.631
.140		1.375	.601
.160		1.039	.449
.180		.731	.332
0	42.7	3.900	0.814
.020		3.649	.825
.040		3.413	.837
.060		3.007	.853
.080		2.625	.834
.100		2.057	.648
.120		1.677	.660
.140		1.428	.621
.160		1.057	.443
.180		.757	.340

Table C.43 - Cont.

$\frac{r}{x}$	Average particle size, μm	$\bar{u}_p$, m/s	$\overline{(u'^2_p)}^{1/2}$, m/s
0	52.2	3.931	0.829
.02		3.688	.845
.04		3.448	.819
.06		3.026	.840
.08		2.678	.816
.10		2.150	.663
.12		1.781	.679
.14		1.477	.645
.16		1.108	.466
.18		.829	.359
0	61.7	3.990	0.826
.02		3.724	.821
.04		3.473	.825
.06		3.110	.849
.08		2.703	.814
.10		2.181	.666
.12		1.804	.665
.14		1.535	.640
.16		1.161	.460
.18		.854	.348
0	71.3	3.980	0.847
.02		3.751	.841
.04		3.519	.820
.06		3.116	.829
.08		2.801	.827
.10		2.214	.650
.12		1.906	.657
.14		1.618	.630
.16		1.242	.451
.18		.924	.348

C.3.5 Particle-Laden Jet, Gas-Phase Velocities, S = 0.3

Table C.44 - Phase/Doppler
Gas-Phase Velocities at
x/d = 0.5, S = 0.3[a]

$\frac{r}{x}$	$\frac{\bar{u}}{\bar{u}_c}$	$\frac{(\overline{u'^2})^{1/2}}{\bar{u}_c}$
0	1.0	0.074
.201	.996	.081
.401	1.017	.075
.602	.992	.084
.802	.975	.097
.936	.778	.168
1.00	.611	.205
1.069	.310	.111
1.136	.209	.093
1.20	.142	.077

$a_{\bar{u}_c}$ = 11.95 m/s.

Table C.45 - Phase/Doppler
Gas-Phase Velocities at
x/d = 2, S = 0.3[a]

$\frac{r}{x}$	$\frac{\bar{u}}{\bar{u}_c}$	$\frac{(\overline{u'^2})^{1/2}}{\bar{u}_c}$
0	1.0	0.096
.067	1.04	.079
.134	1.00	.119
.201	.888	.181
.267	.638	.177
.334	.326	.131
.368	.170	.075
.401	.112	.062

$a_{\bar{u}_c}$ = 11.20 m/s.

Table C.46 - Phase/Doppler Gas-Phase Velocities at x/d = 5, S = 0.3[a]

$\frac{r}{x}$	$\frac{\bar{u}}{\bar{u}_c}$	$\frac{(\overline{u'^2})^{1/2}}{\bar{u}_c}$
0	1.0	0.168
.054	.909	.209
.107	.733	.196
.160	.476	.162
.187	.230	.125
.214	.214	.097
.241	.128	.083
.267	.080	.045

$a_{\bar{u}_c}$ = 9.35 m/s.

Table C.47 - Phase/Doppler Gas-Phase Velocities at x/d = 10, S = 0.3[a]

$\frac{r}{x}$	$\frac{\bar{u}}{\bar{u}_c}$	$\frac{(\overline{u'^2})^{1/2}}{\bar{u}_c}$
0	1.0	0.227
.027	.957	.238
.054	.870	.220
.080	.722	.226
.107	.539	.191
.134	.409	.170
.160	.209	.115
.187	.148	.085
.214	.104	.063

$a_{\bar{u}_c}$ = 5.75 m/s.

Table C.48 - Phase/Doppler
Gas-Phase Velocities at
$x/d = 20$, $S = 0.3$[a]

$\frac{r}{x}$	$\frac{\bar{u}}{\bar{u}_c}$	$\frac{(\overline{u'^2})^{1/2}}{\bar{u}_c}$
0	1.0	0.278
.020	1.0	.252
.040	.833	.258
.060	.767	.235
.080	.633	.242
.100	.483	.212
.120	.383	.182
.140	.317	.160
.160	.200	.113
.180	.183	.100

[a] $\bar{u}_c = 3.0$ m/s.

C.3.6 Particle-Laden Jet, Particle Velocities, S = 0.3

Table C.49 - Phase/Doppler Particle Velocities at x/d = 0.5, S = 0.3

$\frac{r}{x}$	Average particle size μm	$\bar{u}_p$ m/s	$\overline{(u'^2_p)}^{1/2}$ m/s
0	14.3	11.527	1.084
.201		11.605	1.111
.401		11.301	1.243
.602		10.211	1.432
.802		9.603	1.427
.936		8.492	1.835
1.0		6.944	1.981
1.069		4.602	1.765
1.136		3.860	1.715
1.203		3.045	1.607
1.270		2.725	1.350
1.337		1.924	1.013
0	23.7	10.584	1.130
.201		10.634	1.158
.401		10.206	1.260
.602		9.271	1.301
.802		8.861	1.295
.936		8.146	1.566
1.0		7.036	1.836
1.069		5.205	1.817
1.136		4.380	1.614
1.203		3.630	1.429
1.270		2.894	1.289
1.337		2.357	1.143
0	33.3	9.520	1.329
.201		9.670	1.317
.401		9.449	1.241
.602		8.842	1.157
.802		8.540	1.172
.936		7.871	1.441
1.0		7.240	1.617
1.069		5.929	1.666
1.136		5.339	1.605
1.203		4.704	1.512
1.270		3.925	1.492
1.337		3.101	1.427

Table C.49 - Cont.

$\frac{r}{x}$	Average particle size, μm	$\bar{u}_p$, m/s	$\overline{(u'^2_p)}^{1/2}$, m/s
0	42.7	8.825	1.421
.201		8.930	1.338
.401		8.849	1.175
.602		8.512	1.071
.802		8.292	1.064
.936		7.868	1.258
1.0		7.390	1.435
1.069		6.473	1.544
1.136		6.173	1.485
1.203		5.721	1.405
1.270		5.150	1.463
1.337		4.081	1.583
0	52.2	8.265	1.406
.201		8.406	1.309
.401		8.394	1.086
.602		8.221	.993
.802		8.149	.984
.936		7.854	1.075
1.00		7.462	1.207
1.069		6.917	1.318
1.136		6.737	1.303
1.203		6.436	1.233
1.270		6.035	1.225
1.337		5.286	1.394
0	61.7	7.703	1.306
.201		7.802	1.238
.401		7.783	1.096
.602		7.877	.948
.802		7.968	.942
.936		7.776	.947
1.00		7.507	1.061
1.069		7.057	1.177
1.136		6.968	1.134
1.203		6.724	1.370
1.270		6.521	1.035
1.337		5.942	1.137
0	71.3	7.648	1.329
.201		7.714	1.253
.401		7.784	1.043
.602		7.692	.880
.802		7.769	.900
.936		7.481	.898
1.00		7.181	1.028
1.069		6.900	1.119
1.136		6.892	1.140
1.203		6.676	1.117
1.270		6.550	.995
1.337		6.057	1.135

Table C.50 - Phase/Doppler Particle Velocities at x/d = 2, S = 0.3

$\frac{r}{x}$	Average particle size μm	$\bar{u}_p$ m/s	$\overline{(u'^2_p)}^{1/2}$ m/s
0	14.3	10.986	1.062
.067		11.226	1.006
.134		10.758	1.373
.201		9.473	1.883
.267		7.099	1.941
.334		4.282	1.739
.368		3.001	1.396
.401		1.933	1.031
0	23.7	10.481	0.996
.067		10.696	.957
.134		10.295	1.241
.201		9.048	1.717
.267		6.948	1.887
.334		4.228	1.728
.368		2.883	1.370
.401		1.986	1.064
0	33.3	9.902	0.969
.067		10.161	.910
.134		9.991	1.020
.201		9.329	1.348
.267		7.620	1.818
.334		4.903	1.892
.368		3.474	1.497
.401		2.183	1.118
0	42.7	9.458	0.975
.067		9.724	.899
.134		9.852	.890
.201		9.366	1.067
.267		8.177	1.486
.374		5.977	1.850
.368		4.414	1.584
.401		3.193	1.340

Table C.50 - Cont.

$\frac{r}{x}$	Average particle size μm	$\bar{u}_p$ m/s	$\overline{(u'^2_p)}^{1/2}$ m/s
0	52.2	9.147	1.007
.067		9.396	.911
.134		9.463	.844
.201		9.211	.906
.267		8.454	1.197
.334		6.947	1.521
.368		5.358	1.430
.401		4.300	1.281
0	61.7	8.947	1.188
.067		9.163	1.080
.134		9.091	.845
.201		8.824	.888
.267		8.380	.966
.334		7.434	1.158
.368		5.974	1.152
.401		5.062	1.038
0	71.3	8.743	0.997
.067		8.969	.987
.134		8.984	.773
.201		8.801	.781
.267		8.362	.948
.334		7.424	1.071
.368		6.149	1.100
.401		5.325	1.049

Table C.51 - Phase/Doppler Particle Velocities at x/d = 5, S = 0.3

$\frac{r}{x}$	Average particle size μm	$\bar{u}_p$ m/s	$\overline{(u'^2_p)}^{1/2}$ m/s
0	14.3	9.441	1.374
.053		9.169	1.684
.107		7.689	2.044
.160		4.443	1.751
.187		3.115	1.251
.214		2.407	1.088
.241		1.383	.721
.267		1.150	.738
0	23.7	9.032	1.458
.053		8.723	1.722
.107		6.983	2.034
.160		4.131	1.621
.187		2.865	1.252
.214		2.151	1.058
.241		1.200	.690
.267		.955	.658
0	33.3	8.696	1.520
.053		8.273	1.746
.107		6.705	1.960
.160		4.410	1.661
.187		3.144	1.253
.214		2.484	1.124
.241		1.502	.769
.267		1.201	.724
0	42.7	8.543	1.616
.053		8.091	1.807
.107		6.809	2.026
.160		4.673	1.708
.187		3.477	1.335
.214		2.721	1.213
.241		1.683	.800
.267		1.435	.796

Table C.51 - Cont.

$\frac{r}{x}$	Average particle size, μm	$\bar{u}_p$, m/s	$\overline{(u'^2_p)}^{1/2}$, m/s
0	52.2	8.665	1.516
.053		8.270	1.897
.107		7.203	2.021
.160		5.281	1.841
.187		3.867	1.389
.214		3.109	1.305
.241		1.943	.828
.267		1.658	.825
0	61.7	9.064	1.382
.053		8.958	1.491
.107		7.946	1.797
.160		6.122	1.713
.187		4.563	1.368
.214		3.772	1.317
.241		2.287	.796
.267		2.056	.789
0	71.3	9.129	1.424
.053		8.987	1.389
.107		8.224	1.562
.160		6.615	1.582
.187		5.015	1.249
.214		4.358	1.322
.241		2.550	.715
.267		2.388	.677

Table C.52 - Phase/Doppler Particle Velocities at x/d = 10, S = 0.3

$\frac{r}{x}$	Average particle size μm	$\bar{u}_p$ m/s	$\overline{(u'^2_p)}^{1/2}$ m/s
0	14.3	6.359	1.327
.027		6.294	1.375
.053		5.677	1.459
.080		4.687	1.482
.107		3.962	1.311
.134		2.771	1.093
.160		2.055	.852
.187		1.50	.721
.214		.931	.491
0	23.7	6.296	1.321
.027		6.176	1.366
.053		5.680	1.435
.080		4.704	1.469
.107		3.465	1.257
.134		2.592	1.117
.160		1.781	.852
.187		1.164	.687
.214		.758	.459
0	33.3	6.127	1.293
.027		6.135	1.363
.053		5.602	1.374
.080		4.709	1.440
.107		3.652	1.277
.134		2.808	1.155
.160		1.940	.892
.187		1.332	.714
.214		.836	.498
0	42.7	6.040	1.245
.027		5.931	1.280
.053		5.393	1.388
.080		4.613	1.395
.107		3.701	1.265
.134		2.957	1.171
.160		2.071	.918
.187		1.439	.757
.214		.916	.539

Table C.52 - Cont.

$\frac{r}{x}$	Average particle size, μm	$\bar{u}_p$, m/s	$\overline{(u'^2_p)}^{1/2}$, m/s
0	52.2	5.813	1.247
.027		5.704	1.303
.053		5.158	1.365
.080		4.448	1.377
.107		3.729	1.251
.134		2.992	1.164
.160		2.191	.926
.187		1.621	.779
.214		1.015	.577
0	61.7	5.665	1.359
.027		5.525	1.365
.053		5.043	1.422
.080		4.271	1.370
.107		3.681	1.287
.134		2.989	1.175
.160		2.282	.929
.187		1.673	.781
.214		1.083	.575
0	71.3	5.940	1.362
.027		5.424	1.366
.053		5.101	1.568
.080		4.490	1.458
.107		3.650	1.283
.134		3.136	1.192
.160		2.303	.942
.187		1.846	.765
.214		1.220	.586

Table C.53 - Phase/Doppler Particle Velocities at x/d = 20, S = 0.3

$\frac{r}{x}$	Average particle size μm	$\bar{u}_p$ m/s	$\overline{(u'^2_p)}^{1/2}$ m/s
0	14.3	3.302	0.736
.020		3.275	.728
.040		2.953	.780
.060		2.673	.820
.080		2.367	.783
.100		1.982	.664
.120		1.547	.590
.140		1.300	.569
.160		.988	.468
.180		.798	.378
0	23.7	3.346	0.765
.020		3.246	.769
.040		2.949	.784
.060		2.874	.799
.080		2.305	.788
.100		1.902	.677
.120		1.433	.597
.140		1.233	.566
.160		.870	.428
.180		.646	.341
0	33.3	3.474	0.759
.020		3.427	.766
.040		3.141	.793
.060		2.866	.780
.080		2.445	.803
.100		2.063	.703
.120		1.629	.637
.140		1.365	.607
.160		.968	.475
.180		.708	.369
0	42.7	3.515	0.753
.020		3.484	.771
.040		3.187	.790
.060		2.916	.779
.080		2.494	.813
.100		2.143	.718
.120		1.721	.651
.140		1.377	.619
.160		1.00	.473
.180		.769	.377

Table C.53 - Cont.

$\frac{r}{x}$	Average particle size, μm	$\bar{u}_p$, m/s	$\overline{(u'^2_p)}^{1/2}$, m/s
0	52.2	3.573	0.773
.020		3.496	.760
.040		3.240	.773
.060		2.935	.776
.080		2.502	.801
.100		2.170	.713
.120		1.771	.662
.140		1.475	.628
.160		1.061	.478
.180		.800	.391
0	61.7	3.526	0.796
.020		3.523	.771
.040		3.231	.775
.060		2.955	.788
.080		2.560	.797
.100		2.234	.700
.120		1.808	.665
.140		1.526	.631
.160		1.090	.481
.180		.812	.388
0	71.3	3.629	.747
.020		3.599	.732
.040		3.275	.776
.060		2.971	.765
.080		2.573	.780
.100		2.285	.699
.120		1.911	.647
.140		1.592	.623
.160		1.192	.469
.180		.931	.382

NASA
National Aeronautics and Space Administration

Report Documentation Page

1. Report No.	2. Government Accession No.	3. Recipient's Catalog No.
NASA TM-100881		

4. Title and Subtitle	5. Report Date
Particle-Laden Weakly Swirling Free Jets: Measurements and Predictions	May 1988
	6. Performing Organization Code: E-2913

7. Author(s)	8. Performing Organization Report No.
Daniel L. Bulzan	505-62-21
	10. Work Unit No.

9. Performing Organization Name and Address	11. Contract or Grant No.
National Aeronautics and Space Administration Lewis Research Center Cleveland, Ohio 44135	13. Type of Report and Period Covered: Technical Memorandum

12. Sponsoring Agency Name and Address	14. Sponsoring Agency Code
National Aeronautics and Space Administration Washington, D.C. 20546	

15. Supplementary Notes

This report was a thesis submitted in partial fulfillment of the requirements for the degree Doctor of Philosophy to The Pennsylvania State University, University Park, Pennsylvania in May 1988.

16. Abstract

A theoretical and experimental investigation of particle-laden, weakly swirling, turbulent free jets was conducted. Glass particles, having a Sauter mean diameter of 39 μm, with a standard deviation of 15 μm, were used in the study. A single loading ratio (the mass flow rate of particles per unit mass flow rate of air) of 0.2 was used in the experiments. Measurements are reported for three swirl numbers, ranging from 0 to 0.33. The measurements included mean and fluctuating velocities of both phases, and particle mass flux distributions. Measurements were also completed for single-phase non-swirling and swirling jets, as baselines. Measurements were compared with predictions from three types of multiphase flow analysis, as follows: (1) locally homogeneous flow (LHF), where slip between the phases was neglected; (2) deterministic separated flow (DSF), where slip was considered but effects of turbulence/particle interactions were negelected, and (3) stochastic separated flow (SSF), where effects of both interphase slip and tubulence/particle interactions were considered using random sampling for turbulence properties in conjunction with random-walk computations for particle motion. Single-phase weakly swirling jets were considered first. Predictions using a standard k-ϵ turbulence model, as well as two versions modified to account for effects of streamline curvature, were compared with measurements. Predictions using a streamline curvature modification based on the flux Richardson number gave better agreement with measurements for the single-phase swirling jets than the standard k-ϵ model. For the particle-laden jets, the LHF and DSF models did not provide very satisfactory predictions. The LHF model generally overestimated the rate of decay of particle mean axial and angular velocities with streamwise distance, and predicted particle mass fluxes also showed poor agreement with measurements, due to the assumption of no-slip between phases. The DSF model also performed quite poorly for predictions of particle mass flux because turbulent dispersion of the particles was neglected. The SSF model, which accounts for both particle inertia and turbulent dispersion of the particles, yielded reasonably good predictions throughout the flow field for the particle-laden jets.

17. Key Words (Suggested by Author(s))	18. Distribution Statement
Swirling jets; Two-phase flows; Particle-laden jets	Unclassified - unlimited Subject Category 07

19. Security Classif. (of this report)	20. Security Classif. (of this page)	21. No of pages	22. Price*
Unclassified	Unclassified	240	A11

*For sale by the National Technical Information Service, Springfield, Virginia 22161

National Aeronautics and
Space Administration

Lewis Research Center
Cleveland, Ohio 44135

SECOND CLASS MAIL

ADDRESS CORRECTION REQUESTED

Official Business
Penalty for Private Use $300

Postage and Fees Paid
National Aeronautics and
Space Administration
NASA-451

NASA